1969

Silicon detector studies of nuclear internal conversion in Sm155 and Nd151

David Francis Boneau
Iowa State University

69-20,626

BONEAU, David Francis, 1940-

SILICON DETECTOR STUDIES OF NUCLEAR INTERNAL CONVERSION IN Sm^{155} AND Nd^{151}.

Iowa State University, Ph.D., 1969
Physics, nuclear

University Microfilms, Inc., Ann Arbor, Michigan

SILICON DETECTOR STUDIES OF NUCLEAR INTERNAL CONVERSION IN Sm^{155} AND Nd^{151}

by

David Francis Boneau

A Dissertation Submitted to the
Graduate Faculty in Partial Fulfillment of
The Requirements for the Degree of
DOCTOR OF PHILOSOPHY

Major Subject: Nuclear Physics

Approved:

Signature was redacted for privacy.

In Charge of Major Work

Signature was redacted for privacy.

Head of Major Department

Signature was redacted for privacy.

Dean of Graduate College

Iowa State University
Ames, Iowa

1969

TABLE OF CONTENTS

I. INTRODUCTION

A. Internal Conversion

An excited nucleus can make a transition to a lower energy level in one of several ways. For transition energies less than one MeV, the principal processes are gamma-ray emission and internal conversion. In the former process, the nucleus emits a photon with energy very close to the transition energy. In internal conversion, the nuclear transition energy is transferred directly to one of the orbital electrons, ejecting it from the atom with kinetic energy equal to the nuclear transition energy minus the original binding energy of the electron.

For a given nuclear transition, the total internal conversion coefficient, α, is defined as the ratio of the rate of ejection of internal conversion electrons, I_e, to the rate of gamma-ray emission, I_γ. Hence,

$$\alpha = I_e/I_\gamma$$

and $\alpha \geq 0$. A transition can convert in any filled electron shell of the atom provided the electron binding energy is less than the transition energy. The total internal conversion coefficient is simply the sum of similar coefficients for the various filled shells and subshells. Thus

$$\alpha = \alpha_K + \alpha_L + \alpha_M + \cdots$$

where

$$\alpha_L = \alpha_{L_I} + \alpha_{L_{II}} + \alpha_{L_{III}}$$

and likewise for the remaining shells.

The internal conversion coefficients depend strongly on a number of parameters. One obvious parameter is the shell or subshell where conversion takes place. Since the internal conversion process proceeds via the electromagnetic interaction between the orbital electron and the charged nucleus, electrons in higher shells are usually less likely to be converted. The conversion coefficients are also very sensitive to the atomic number, the transition energy, and the multipolarity (angular momentum and parity change) of the transition. In general, conversion coefficients increase with increasing atomic number and decreasing transition energy. It is the strong dependence of conversion coefficients on the multipole character of a transition, coupled with the fact that conversion coefficients are normally independent of detailed nuclear structure, that makes internal conversion measurements a useful tool in nuclear spectroscopy. A measured internal conversion coefficient is compared with theoretical values for all reasonable multipolarities. Extensive tables of theoretical conversion coefficients have been calcu-

lated and compiled by several workers (1,2,3). Good agreement between a measured coefficient and the corresponding calculated conversion coefficient for a single multipolarity then fixes the multipole character of the transition in question.

A particular transition, however, does not necessarily have a pure multipole character. If the nuclear angular momenta of the initial and final states are J_i and J_f, the radiated field can have any angular momentum L for which

$$|J_i - J_f| \leq L \leq J_i + J_f .$$

For each multipole order L, there are two possible classes of radiation; namely, electric 2^L-pole (EL) and magnetic 2^L-pole (ML), which differ with respect to parity. If there is no parity change in a nuclear transition, there can be emission of only electric multipoles of even order (L even) or magnetic multipoles of odd order. If parity does change in the transition, the allowed even and odd orders are simply reversed. Finally, because of the transverse nature of electromagnetic waves, no gamma-ray radiation of multipole order 0 can occur.

If more than one multipole order is allowed, the internal conversion coefficient for the i th shell or subshell is a mixture of the form

$$\alpha_i = \sum_{\text{allowed } L} a(L)\alpha_i(L)$$

where a(L) is the fraction of the gamma rays that carry away angular momentum L. The theory of multipole radiation (4) usually restricts observed conversion coefficients to at most a mixture of the two multipoles with the smallest allowed values of L. Some transitions studied in this work have mixtures of M1 plus E2 or E1 plus M2 multipole character. For such transitions

$$\alpha_i = a_1\alpha_i(M1) + a_2\alpha_i(E2)$$

or

$$\alpha_i = a_1\alpha_i(E1) + a_2\alpha_i(M2).$$

Here $\delta^2 = a_2/a_1$ is defined as the mixing ratio. Since $a_1 + a_2 = 1$, the measurement of a single conversion coefficient for a mixed transition can be combined with theoretical conversion coefficients for the pure multipoles to yield a value for the mixing ratio. In cases where a particular coefficient is not very sensitive to δ^2, only an imprecise value of the mixing ratio will be obtained unless other coefficients are measured. Values of δ^2 are important in the comparison of a particular nuclear model with experiment because calculations of the pure-multipole gamma-ray transition probabilities for the model can normally be performed.

B. Theoretical Internal Conversion Coefficients

One of the purposes of this work is to determine the multipolarity of some nuclear transitions by comparison of measured and theoretical internal conversion coefficients. Hence, it is appropriate to describe briefly the basic procedures used in conversion coefficient calculations. For a complete description of the methods involved, the original works (1,2,3,5,6) or the review article by Rose (7) should be consulted.

All modern calculations of conversion coefficients have been performed on the basis of lowest order perturbation theory - first order for the gamma-ray transition probability and second order for the conversion electron transition probability. They differ in the model or potential used to compute the electron wavefunctions and in their treatment of the effects of finite nuclear size.

The first values of Rose et al. (5) were computed for a point nucleus and a pure Coulomb potential. Rose's later calculations (6) used a Thomas-Fermi-Dirac screened potential. Sliv and Band (2) retained the same potential but included the effects of finite nuclear size for the first time. There are two effects. First, the electron wavefunction is modified,

especially in the important region near the nuclear origin. This is called the static effect since it depends only on the nuclear charge density. A second (dynamic) effect also arises because the electron now spends a fraction of its time inside the nucleus where it probes the details of the nuclear charges and currents. If this dynamic effect is included, model-dependent nuclear matrix elements no longer cancel in the conversion coefficient calculation. Sliv and Band assumed a constant nuclear charge density and a uniform surface transition current density to account for the static and dynamic effects. Their tables give K-shell and L-subshell coefficients calculated on these assumptions. The latest tables by Rose (1) give coefficients for the K, L_I and L_{II} shells which include the static effect through a constant nuclear charge density. The L_{III} coefficients neglect even the static effect since it is not expected to be important.

The most complete internal conversion coefficient calculations have been performed by Hager and Seltzer (3). They ignored the model-dependent dynamic effect, but accounted for the static effect by the use of a realistic nuclear charge density with a Fermi shape. Their electron wavefunctions were derived from the Kohn and Sham (8) version of a relativistic Hartree-Fock-Slater (9) self consistent field calcula-

tion. Conversion coefficients were computed for all the K, L, M subshells for each atomic number from 30 to 103 and for a wide range of transition energies beginning one keV above threshold. Since this calculation is easily the most comprehensive to date, all theoretical conversion coefficients quoted in this work were interpolated from the table of Hager and Seltzer.

The dynamic effect is usually small since the electron spends so little time inside the nucleus. Yet, as pointed out by Church and Weneser (10), it can be important in transitions for which the gamma-ray matrix element is greatly inhibited. Such dynamic penetration effects have been found in Lu^{175} (11). However, it is impractical to compile tables of conversion coefficients for every variation of each nuclear model and no general theory of penetration effects is as yet available. For the present, detailed comparison of experiment with the current tables can point the way to the possible existence of penetration effects in more nuclei. For cases where the dynamic effect is not important, the uncertainties in the present tables are about three percent.

C. Methods of Measuring Internal Conversion Coefficients

A variety of methods have been used to measure internal conversion coefficients. In special cases, a clever trick can produce a measured conversion coefficient from an indirect experimental approach. A particularly ingeneous ploy was employed by Pettersson et al. (12) to determine the K-shell conversion coefficient of the 412-keV transition in the decay of Au^{198} from an angular correlation experiment. This was possible since the same radial matrix elements appear in the analytic expressions for the directional correlation function and the internal conversion coefficient. However, in the usual type of internal conversion coefficient measurement, two of the following three transition rates are measured: (1) the rate of ejection of conversion electrons, I_e; (2) the rate of gamma-ray emission, I_γ; and (3) the total transition rate, $I_o = I_\gamma + I_e$ for all the electron shells. Obviously, if the first two rates can be measured, their ratio gives the conversion coefficient by definition. In some instances, it is more convenient to measure I_o and one of the other two rates.

I_e can be obtained by observing the conversion electrons themselves or the x-rays emitted during readjustment of the atomic electrons following internal conversion. To find I_γ,

one can count either the gamma rays themselves or photoelectrons ejected from a converter placed near the source. I_o can be determined by measuring the rate of emission of particles or photons which uniquely feed the transition. Such radiation might be alpha rays or continuous beta rays from a neighboring nucleus or gamma rays or conversion electrons emitted in a coincident transition.

The discussion below outlines in some detail the more important methods used to measure internal conversion coefficients. The review articles by van Nooijen (13) and Subba Rao (14) provide a more complete summary of experimental methods.

1. Conversion electron peak to beta distribution ratio

This method requires the use of only one major piece of experimental apparatus. A beta spectrometer is employed to measure both the intensities of the conversion electron peaks and the intensity, I_β, of the total distribution on which the peaks sit. The method works best for simple de-excitation schemes where beta decay leads to a single excited state. If I_K is the intensity of the K-shell conversion peak, the experiment determines the ratio

$$\frac{I_K}{I_\beta} = \frac{\alpha_K}{1 + \alpha_{total}}$$

where $\alpha_{total} = \alpha_K + \alpha_L + \alpha_M + \cdots$ is the total conversion coefficient. Then the K-shell internal conversion coefficient is found from

$$\alpha_K = \frac{I_K}{I_\beta - (I_K+I_L+I_M+\cdots)}$$

where I_L, I_M and so forth are the intensities of the peaks due to conversion in the other shells.

The main difficulty with this method lies in obtaining the low-energy contribution to I_β. Distortion due to scattering of electrons from the source and source backing is particularly significant near zero energy. Corrections for these scattering effects require a knowledge of the shape factor for the beta distribution being considered. The work of Parsignault (15) illustrates the principal problems associated with this method.

2. K x-ray to gamma-ray ratio

This is a second specialized method that requires only a single spectrometer. For a simple decay scheme with a single gamma-ray transition, some type of photon spectrometer is used to measure the ratio of I_{K_x}, the rate of emission of K x-rays following internal conversion, to the gamma-ray emission rate, I_γ. The K-shell internal conversion coefficient is then calculated from

$$\alpha_K = \frac{I_{K_x}}{\omega_K I_\gamma}$$

where ω_K, the fluorescent yield of the K shell, is the probability that the filling of a vacancy in the K shell is accompanied by the emission of a K x-ray. Such a vacancy can also be filled via the Auger process. Values of ω_K can be determined from the semi-empirical formula of Hagedoorn and Wapstra (16) or from the tables of Fink et al. (17) to an accuracy of about 2% for atomic numbers above forty.

In using this method, one must account for all extraneous K x-rays due to source thickness, electron-capture decay, competing transitions, contaminants and so forth. At times, some of these unwanted radiations can be eliminated by coincidence techniques or high-resolution apparatus. Nelson and Hatch (18,19) employed a bent-crystal spectrometer to measure K x-ray to gamma-ray ratios in the decays of Tm^{170}, Ho^{166} and Eu^{155}. Boneau and Hatch (20) used a normal NaI(Tl) scintillation crystal in a coincidence arrangement to measure α_K for a transition in Er^{164} by this method. In the work reported here, the conversion coefficient for a transition in the decay of Sm^{155} was found from the K x-ray to gamma-ray ratio determined with a semiconductor detector.

3. Internal-external conversion

This is a more general method of measuring conversion coefficients that still requires only one spectrometer. A magnetic beta-ray spectrometer is used to count not only the internal conversion electrons but also the gamma rays via the external conversion process. First, the conversion electron counting rates are measured with the source at the entrance slit of the beta-ray spectrometer. Then, the source is moved away a short distance and a high-Z converter is placed at the original source position. Gamma rays from the source now eject photoelectrons from the various shells of the atoms in the converter. The gamma-ray counting rates are determined by analyzing these external conversion electrons in the beta-ray spectrometer. Conversion coefficients are then found simply from the ratio of internal conversion electron to gamma-ray counting rates. In this ratio, the transmission of the spectrometer cancels; but the efficiency of the external converter remains. This efficiency depends upon the angular distribution of ejected photoelectrons plus straggling effects in the converter as well as on the absolute photoelectric cross-section. The calculation of this efficiency has been refined several times by Hultberg (21,22,23) and internal con-

version coefficients can now be measured to five percent with the internal-external conversion method (24,25,26).

The internal-external conversion method can be applied to a complicated decay scheme where many details of the scheme are unknown. However, the radioactive source used must be both strong enough to produce a reasonable external conversion electron counting rate and also thin enough so the internal conversion electrons escape the source without scattering. In addition, the half-life of the source must be long enough so that both internal and external conversion measurements can be made.

4. Coincidence methods

Since coincidence techniques are of basic importance throughout the field of nuclear physics, it is not surprising to find these techniques applied to conversion coefficient measurements in many different ways. Normally, coincidence methods require gating upon radiation which feeds the state whose de-excitation is of interest. Both the number of gating events and the number of coincident gamma rays or conversion electrons are counted. The ratio of the intensity of a coincident gamma ray to the gating rate equals $1/(1+\alpha_{total})$. Similarly, the ratio of the intensity of a coincident K-shell

electron to the gating rate equals $\alpha_K/(1+\alpha_{total})$. Either of these two results can be combined with a measurement of the K/(L+M+···) electron ratio to give a value for α_K. Numerous variations of the general method are possible. Particular examples may be found in the work of Duke and Talbert (27), Schupp and Hatch (28), Lewin et al. (29), Croft et al. (30), Pettersson et al. (31) and Gerholm (32).

5. Normalized conversion electron to gamma-ray ratio

The most direct way to determine a conversion coefficient is to measure the intensities of the gamma ray and its corresponding conversion electron line. The ratio I_e/I_γ gives the conversion coefficient by definition. Normally, different spectrometers are used to find the relative intensities of the gamma rays and the internal conversion electrons in a complex decay. If the conversion coefficient for one of the transitions is known from some other measurement, this "standard" transition can be used to normalize the electron intensities to those of the gamma rays. The conversion coefficients for the other transitions can then be found from

$$\alpha = \frac{I_e}{I_e{}^s} \quad \frac{I_\gamma{}^s}{I_\gamma} \quad \alpha_s \ .$$

The standard conversion coefficient might be measured by one of the other methods or the multipolarity of the standard

transition might be known so that the corresponding theoretical conversion coefficient can be taken as the standard. In the decay of Nd^{149}, for example, the lifetime of the isomeric state at 240.3 keV indicates that the transition depopulating this level has M2 character. Hence, the theoretical M2 conversion coefficient for this transition can serve as α_s (33, 34). In another variation, Hatch et al. (35) mixed Te^{123m} with the actual experimental source and treated the well-known conversion coefficient of the 159-keV transition in Te^{123m} as the standard. The normalized conversion electron to gamma-ray ratio method requires two separate relative intensity measurements plus a determination of α_s. The efficiencies of both a beta-ray and a gamma-ray spectrometer must be calibrated, and the uncertainties introduced by these two instruments must be combined with the uncertainty in the standard conversion coefficient. Hence, it is difficult to measure conversion coefficients to better than ten percent with this method. Note, however, that the determinations of the electron relative intensities, the gamma-ray relative intensities and the standard conversion coefficient can be completely distinct. These separate measurements may be performed by different groups at different times with different equipment.

In the study reported here, the normalized conversion electron to gamma-ray ratio method was employed to find conversion coefficients of some transitions in the decays of two shortlived nuclei. The appropriate gamma-ray intensities have been measured by other workers. Measurements of the conversion electron relative intensities and the standard conversion coefficients are described herein. These various results were combined to yield internal conversion coefficients for a number of transitions in the decays of Sm^{155} and Nd^{151}.

D. Methods of Measuring Internal Conversion Electron Relative Intensities

Three types of experimental apparatus have been used recently to obtain accurate conversion electron relative intensities. They are the semicircular magnetic spectrograph, the magnetic beta-ray spectrometer and the silicon semiconductor detector.

1. Magnetic spectrograph

Slätis (36,37,38,39) has described the semicircular magnetic spectrograph method in detail. In this method, electrons emitted by a radioactive source are bent into helical trajectories by a homogeneous magnetic field and allowed to impinge upon an extended photographic plate after they complete half a revolution. Since the radius of an electron

trajectory is proportional to the electron momentum, electrons with different momenta (and, hence, different energies) strike the photographic plate at different radii. Thus, electrons of a given energy show up as a darkened line at a particular distance along the photographic plate. The energy of the electron line is determined simply from its position on the plate. The electron intensity, however, depends upon the actual number of electrons which hit the photographic plate. A microphotometer is used to measure the relative "darkness" of the plate which is related to the electron exposure by the Silberstein (40,41) formula

$$D \equiv \log_{10} I_o/I = C \log_{10}(E+1).$$

Here I_o is the light intensity transmitted through an unexposed portion of plate, I is the light intensity at any exposed portion, E is the corresponding exposure in electrons/area and C is a calibration constant which must be determined. Corrections must be made for the variations with electron energy of not only the sensitivity of the photographic emulsion but also the effective solid angle subtended by the photographic plate. A further correction is sometimes made for the fact that electrons penetrate the photographic emulsion at different angles. Helmer and McIsaac (33) have recently employed the magnetic

spectrograph method to find relative intensities of conversion electrons from the decay of Nd^{149} with uncertainties of 10-20%.

The magnetic spectrograph combines fine energy resolution with the ability to record an entire spectrum at one time. These features are especially important for work with short-lived activities. However, the tedious procedure for determining relative intensities yields results with uncertainties as small as ten percent only in very favorable cases.

2. Magnetic beta-ray spectrometer

In a magnetic beta-ray spectrometer, a carefully designed magnetic field is employed to focus electrons of nearly the same momentum onto an electron counter. Only electrons of a particular momentum and energy can travel from source to counter; all other radiations are blocked by a system of shields and baffles. Normally, the electron detector is a low-resolution counter such as a Geiger-Müller tube or a scintillation crystal which simply signals the arrival of an electron. Momentum selection is accomplished by the magnetic field. A complete spectrum is recorded by counting the electron rate at a particular momentum, incrementing the current so the magnetic field selects a nearby momentum and counting the electron rate at the new momentum. The process is repeated automatically until the region of interest is scanned

in as small increments as desired.

Two principal characteristics of magnetic beta-ray spectrometers are their resolution and their luminosity. For a magnetic spectrometer, resolution is defined as $\Delta p/p$ where Δp is the full-width at half maximum for a peak due to monoenergetic electrons of momentum p. Outstanding resolution of a few hundredths of a percent has been obtained with some magnetic spectrometers. So narrow an instrumental line width is of the order of the natural width of some energy levels (42). The luminosity, L, is defined by $L = \sigma T$. Here σ is the source area and T, the transmission, is the fraction of all monoenergetic electrons leaving the source which is counted in the detector. The desirable objectives of high resolution (small $\Delta p/p$) and high transmission tend to be exclusive. However, Berkvist (43) has designed a scheme of electrostatic correctors which greatly increase the usable source area. The large luminosity thus possible allows both high resolution and a reasonable counting rate. Siegbahn (44) discusses in extensive detail properties of magnetic beta-ray spectrometers of various designs.

In a large number of cases, magnetic spectrometers are nearly ideal for measuring electron relative intensities

because of their unexcelled resolution. Weak conversion electron peaks stand out clearly even if a competing continuous beta-ray distribution is present. The advantage of superior resolution is balanced to an extent by the slow point-by-point data accumulation, the meticulous source preparation required and the technical problems of building, operating and servicing an extensive and complex apparatus. The method of accumulating data is a serious problem for work with short half-lives. The source strength may be essentially gone before any significant portion of a spectrum is recorded. This problem may be overcome (45,46) by operating the magnetic spectrometer on-line at an accelerator or reactor. The radioactive source thus can be continuously replenished as it dies away so that a constant source strength is maintained. However, such on-line operation increases background levels and adds a further layer of technical complications.

3. Silicon semiconductor detector

The theory, fabrication and operation of silicon semiconductor detectors have been discussed by Taylor (47), Dearnaley and Northrop (48,49), Goulding (50) and Hollander (51) among others. The silicon detector method of measuring electron relative intensities will be described in some detail

since this basic approach was used in the investigation reported here.

From the simplest point of view, the intrinsic region of a semiconductor detector acts like an ionization chamber. An incident electron excites a trail of electron-hole pairs as it slows down in the semiconductor. The freed conduction electrons and holes are swept to opposite faces of the detector by an externally applied electric field. The collected charge is converted to a voltage pulse which is amplified and fed into a multichannel pulse-height analyzer. Since the number of electron-hole pairs produced in the semiconductor is proportional to the energy lost by the incident electron in the intrinsic region (one pair is formed for each 3.66 eV energy loss on the average), the pulse height analyzed is ideally a linear function of the electron energy loss. Small deviations from true linearity occur because of variations in the charge collection, pulse amplification and pulse analysis. A source of incident electrons thus produces a spectrum which can be interpreted as showing number of counts versus energy.

The main characteristic for comparison of silicon detectors is the resolution, R(E), which is generally expressed simply as the full energy width at half maximum for a peak due to monoenergetic electrons of some energy E. The resolution

does increase slowly with energy. Resolutions below 1.5 keV (52) have been obtained for electrons of about fifty keV while 2.5 keV is a very good resolution for one MeV electrons. If reasonable resolution is to be obtained, the silicon crystal must be cooled below room temperature in order to reduce thermal noise. The very best resolution further requires that the input stage of the pulse electronics also be cooled.

Silicon detectors can not match the resolution of the best magnetic beta-ray spectrometers. But, they do possess advantages in some cases where extreme resolution is not paramount. Solid angles of practically 2π steradians are possible with little degradation in resolution, and an entire spectrum can be accumulated at one time. Thus, the semiconductor detector is a good choice for analysis of weak sources with short half-lives. In addition, the spins and parities of nuclear levels can often be determined from an electron intensity measurement with moderate resolution. The simplicity of the silicon spectrometer can make such measurements routine.

In order to determine relative electron intensities with a semiconductor spectrometer, the small silicon crystal is exposed to the source under study and a pulse-height spectrum is accumulated. The conversion electron intensity, I_i, of the i th peak relative to an arbitrary standard is then given by

$$I_i = \frac{\epsilon_s}{\epsilon_i} \frac{A_i}{A_s} I_s$$

where I_s is the arbitrary intensity of the standard electron transition, A_i and A_s are the areas of the spectrum attributable, respectively, to the i th and the standard electron peaks and ϵ_i and ϵ_s are the efficiencies of the detector at the corresponding energies. Normally, the A's are defined as the areas of the full-energy peaks and electrons losing less than their full energy in the detector are ignored. In this case (51,52,53), the efficiency at a particular energy becomes the probability that an electron which is emitted from the source with that energy loses all its energy in the detector. In the present work, however, the spectrum area due to monoenergetic electrons of a given energy includes any count caused by an incident electron of that energy. Thus, the relevant efficiency is the probability that an emitted electron loses any energy whatsoever in the detector. The efficiency so defined is approximately constant with energy since any incident electron loses some energy due to collisions with the atomic electrons of the silicon crystal.

In the investigation reported here, a continuous set of response functions for monoenergetic conversion electrons was developed by an interpolation technique. Such a response

function pictures the shape of a spectrum due only to electrons of a given energy. The response function of a silicon detector to monoenergetic electrons of 62 keV is shown in Figure 1. It was assumed that a complex conversion electron spectrum is a linear combination of response functions for conversion electrons of various known energies. A least-squares computer program was applied to yield the linear combination which best fits the experimental data. The computer routine used differs only in input-output details from the unfolding program of Brown and Hatch (54).

Two factors complicate the analysis scheme. First, gamma rays interact with the silicon crystal through the Compton and photoelectric processes. While the silicon efficiency for gamma rays is small compared to the efficiency for electrons, the gamma-ray response can not be neglected. Several spectrometers (55,56,57) have been constructed which greatly reduce the efficiency for gamma-ray detection. A superconducting solenoidal magnet focuses onto a distant silicon detector all electrons emitted into a large solid angle. In the work reported here, the response function due to photons of all energies was obtained by inserting a thin absorber between source and detector to stop the electrons. This total photon response was combined with the electron response functions in

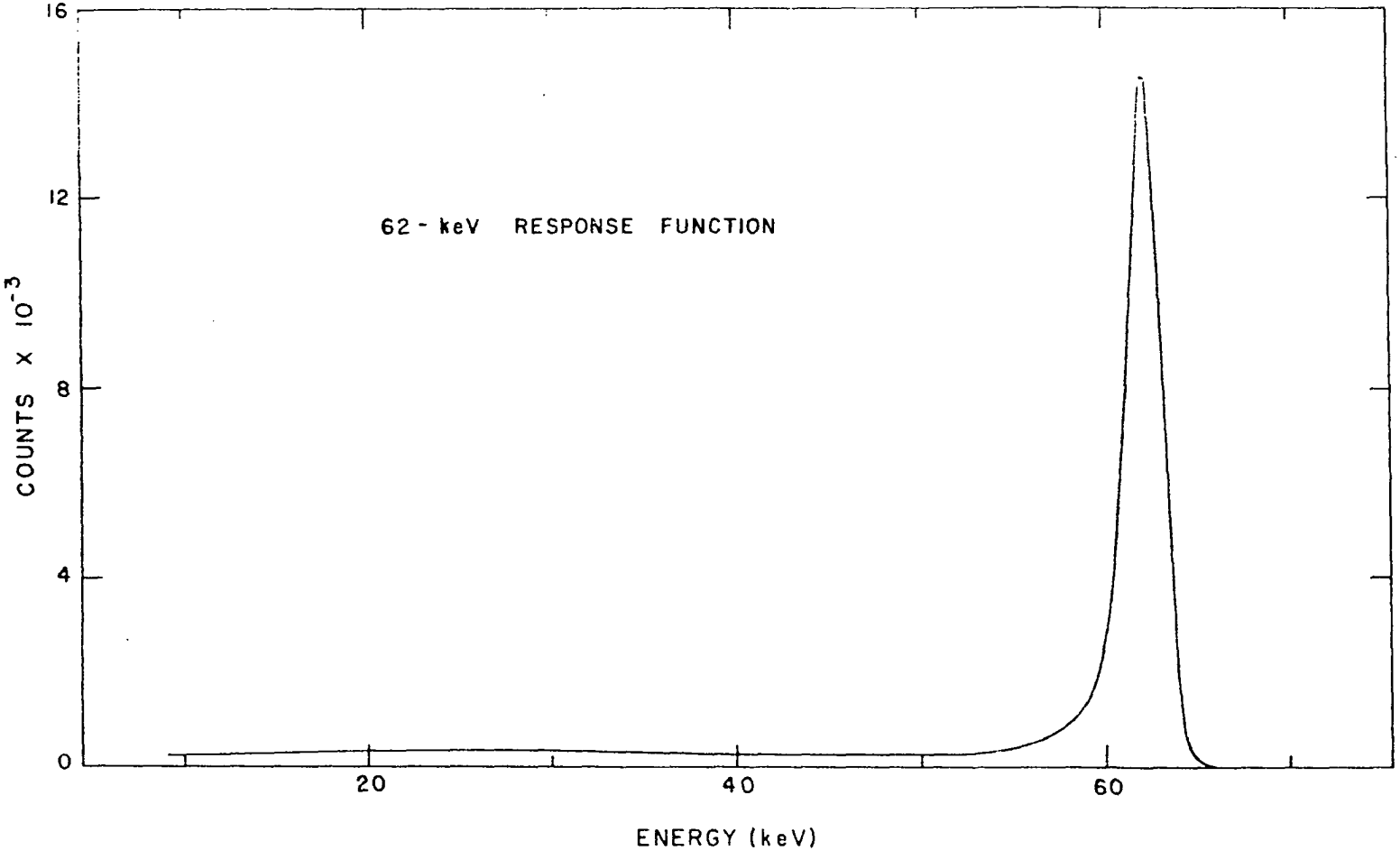

Fig. 1. The response of a silicon detector to monoenergetic electrons of 62 keV

the unfolding program. Second, the analysis scheme assumes a spectrum contains no counts due to continuous beta rays while, in reality, the conversion electrons studied are accompanied by strong beta-ray distributions. A coincidence technique described in the next section was used to eliminate the beta-ray contributions.

In summary, the present method involves developing a library of monoenergetic response functions for electrons, measuring directly the photon response function and suppressing the continuous beta rays by a coincidence method. A linear least-squares analysis is then carried out on the observed pulse-height spectrum to determine the relative intensities of the conversion electrons present.

II. EXPERIMENTAL EQUIPMENT AND METHODS

The principal feature of this investigation is the use of a lithium-drifted silicon detector to measure the relative intensities of internal conversion electrons emitted in the decays of shortlived Sm^{155} and Nd^{151}. Internal conversion coefficients are then deduced for some transitions in the Eu^{155} and Pm^{151} daughters from gamma-ray relative intensity data previously reported by other workers. Measurements of the standard conversion coefficients required by the normalized conversion-electron to gamma-ray ratio method also comprise a part of the present investigation and are described in the second section of this chapter.

A. Internal Conversion Electron Intensity Measurements

The conversion electron relative intensity measurements are subject to special difficulties not encountered in the earlier work of Bosch et al. (53,58,59). Not only are the lifetimes of Sm^{155} and Nd^{151} quite short (22 and 12 minutes), but also their decays are accompanied by strong high-energy beta+ray distributions which mask weak conversion electron peaks. A coincidence method which suppresses the continuous beta rays is described further on in this section. An unusual

feature of the present study is the use of monoenergetic electron response functions to analyze the conversion electron data. The generation of approximate response functions and their relation to the efficiency of the silicon detector are discussed in the latter part of this section. Thus, this section details the silicon spectrometer itself, the coincidence method for reduction of competing beta rays and the spectrometer calibration through development of electron response functions.

1. Description of the silicon spectrometer

The semiconductor spectrometer used was a modified version of the one described by Englert (60). It consisted of a vacuum chamber in which was mounted a 2 mm x 80 mm^2 Kevex model A80x2 lithium-drifted silicon detector. The Si(Li) detector faced a 1.75" x 3" Pilot-B scintillation crystal which formed part of one wall of the spectrometer. The plastic scintillator was used to gate the silicon detector in the coincidence arrangement described below. An Ortec 118A FET preamplifier was modified so the entire unit connected directly to the back of the semiconductor detector. The close proximity of detector and preamplifier reduced the input capacitance seen by the electronics and helped better the Si(Li) resolution. An aper-

ture and a collimator of 1/32 inch copper were placed in front of the Si(Li) detector to suppress the number of electrons scattered not only out of the edges of the detector but also off the chamber walls into the detector. Appendix I discusses the effect of the aperture and collimator on the fraction of incident electrons which lose their full energy in the intrinsic region of the silicon detector. A 0.013 inch aluminum absorber was mounted inside the vacuum chamber so it could be rotated in and out of position between the source and silicon crystal. Figure 2 shows a schematic drawing of the arrangement inside the chamber. The vacuum chamber was maintained at a pressure of about 5×10^{-3} Torr by use of a standard fore pump which was separated from the chamber by a nitrogen cold trap to reduce deposition of pump oil on the Si(Li) detector. A conventional air lock with its own fore pump allowed radioactive sources to be introduced into the chamber without disturbing the vacuum. The design of the source holder assured reproducible positioning of the source on the axis of the detectors. The silicon crystal was cooled by a Dry Ice-alcohol reservoir connected directly to the Si(Li) mount by a copper path. The performance of the silicon detector in this arrangement is pictured in Figure 3. The resolution for the 89K and

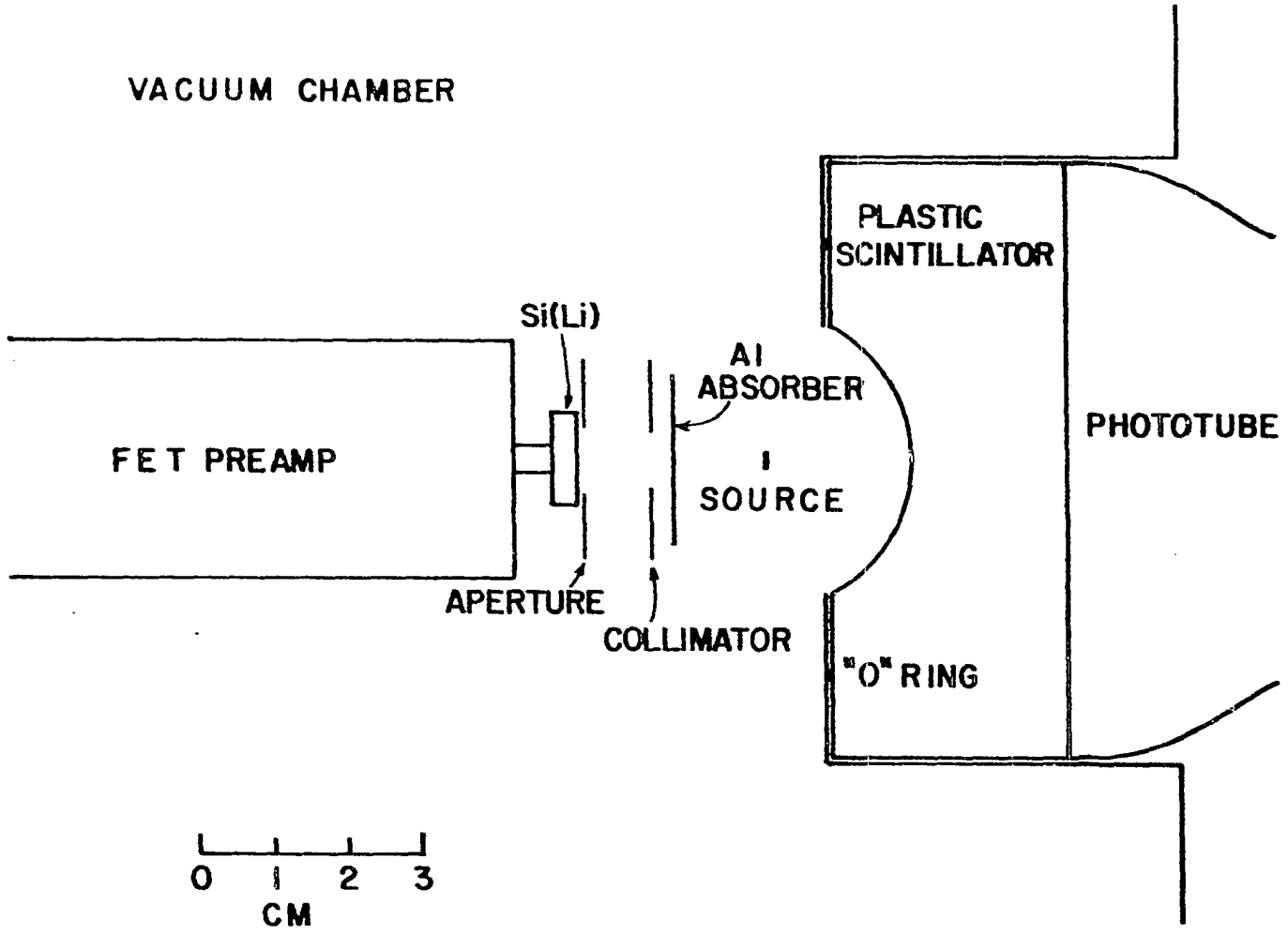

Fig. 2. Schematic drawing of the inside of the vacuum chamber

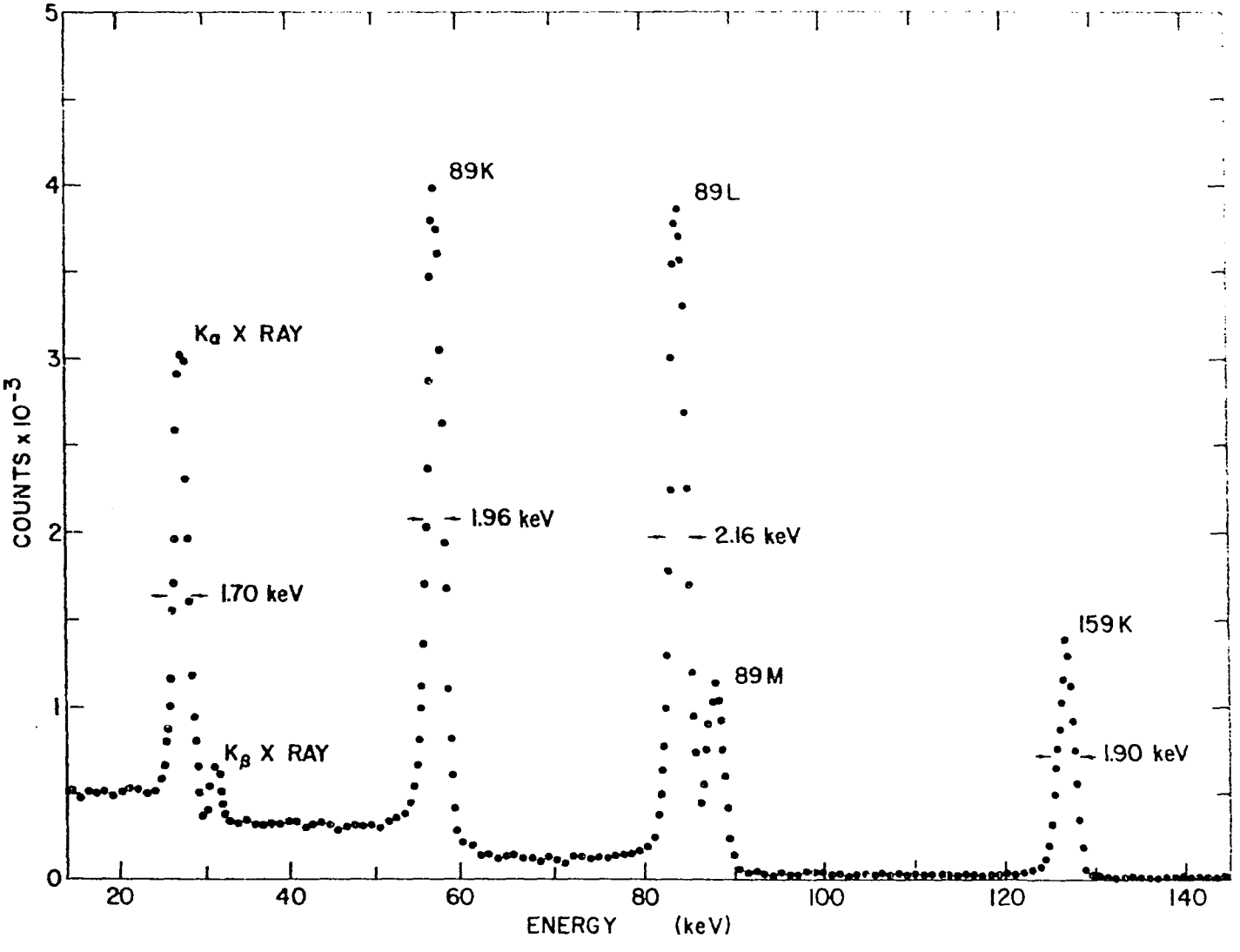

Fig. 3. Portion of a Te^{123m} spectrum seen by the silicon detector

159K electrons from Te^{123m} is seen to be a bit less than two keV. It should be possible to improve the resolution by cooling the input FET of the preamplifier.

2. Coincidence method

The plastic scintillation detector was included in the spectrometer so electron-electron coincidences could be recorded. The idea is to reduce the continuous beta-ray distribution seen in the silicon spectra by requiring time coincidences between conversion electrons in the Si(Li) detector and beta rays in the plastic crystal. Both Sm^{155} and Nd^{151} feature high-energy beta-ray branches feeding fairly low-lying levels in the daughter nuclei. If the beta rays detected by the plastic scintillator have energies greater than the conversion electron energies of interest, the coincident events detected in the silicon crystal can be due only to conversion electrons. Thus, a count in the semiconductor detector is recorded only if it is in time coincidence with a beta ray that lost, say, 600-800 keV in the plastic detector. In practice, a small number of beta rays are still counted by the semiconductor detector because of accidental coincidences and the scattering of beta rays out of the plastic and into the silicon. Figure 4 indicates the effectiveness of the coincidence arrangement

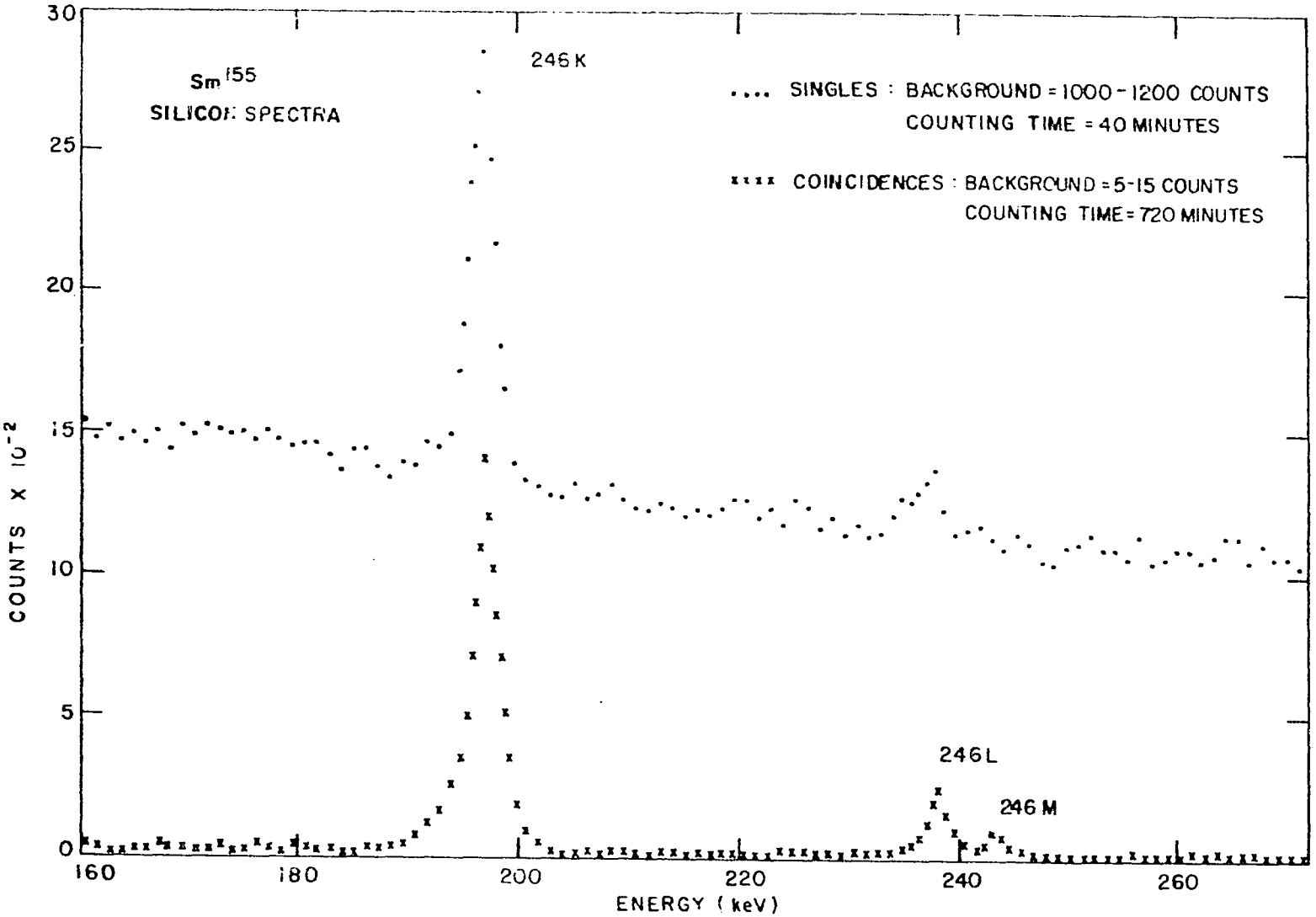

Fig. 4. Comparison of internal conversion lines from 246-keV transition in the Sm^{155} decay as seen in singles and coincidence spectra

in suppressing the continuous beta-ray distribution. After accidental coincidences were subtracted, the background above the 246-keV conversion peaks from Sm^{155} was reduced by a factor of about one hundred from the corresponding beta-ray background in a singles spectrum. This reduction necessitated a twentyfold increase in the counting period. Still, the coincidence technique allowed some weak conversion electron peaks to be seen with the semiconductor spectrometer.

The coincidence method introduces two complexities in addition to the increased counting times. First, gating on high-energy beta rays tends to favor those transitions which are fed by high-energy beta-ray branches. The relative conversion electron intensities observed in the coincidence spectrum are not necessarily the same as the true intensities seen in an undistorted singles spectrum. However, the correct relative intensities for transitions depopulating the same level and for K, L, and M peaks from the same transitions are preserved. Appendix II considers corrections for the effect of this beta-ray branching. Second, the coincidence method allows the possibility of angular correlation effects. It is conceivable that the angular distributions of conversion electrons from different transitions and different shells are peaked at widely varying directions with respect to the beta

rays. Strong angular correlations could upset even the ratios of K, L and M peaks from the same transition. However, the discussion in Appendix III shows that the large solid angles in the semiconductor spectrometer greatly attenuate any correlations present. In addition, nuclear theory requires that the angular distribution of radiation following the strong allowed beta-ray branches be isotropic. One further point is that conversion electrons from an isomeric transition are essentially absent from a coincidence spectrum because of the extended lifetime of the isomeric state.

The corrections described in Appendices II and III require that the decay scheme of the isotope under investigation be known in detail. While the main features of the decay schemes of Sm^{155} and Nd^{151} are known from the gamma-ray work of Funke et al. (61) and Zganjar and Helmer (62), the simplest way of checking the distortions caused by the coincidence method is to refer back to the singles spectra. The stronger electron peaks show up well enough in the singles spectra to allow accurate determinations of their actual relative intensities so that the validity of the corrections for beta-ray branching and angular correlation can be checked. Thus, the present coincidence method does not obviate the need for analysis of singles spectra - an analysis that depends on a knowledge of peak

efficiencies rather than total response functions. In fact, the analysis of the singles spectra must serve as the final measure of the worth of the coincidence scheme. The principal value of the coincidence method is that it does permit the silicon detector to provide some information about weak conversion electron peaks.

Figure 5 shows a block diagram of the electronics associated with the silicon coincidence spectrometer. Pulses from the Si(Li) detector were sent to two separate main amplifiers. The Nuclear Data 524-A was used in the single RC-clipping mode to yield maximum resolution in the recorded spectrum. Ortec 410 amplifiers, operating in the double-delay-line-clipping mode, fed timing and amplitude information to the coincidence circuit from both the silicon and plastic detectors. The coincidence circuit itself was composed of other modules from the Ortec 400 series. The 2τ resolution time of the coincidence circuit was normally set at 60 nsec and the accidentals were never more than 2-3% of the true coincidences. Tests showed that the centroid of the coincidence distribution varied less than 5 nsec when the electron energy detected in the silicon changed from 60 to 600 keV. Pulse-height spectra were recorded in a 1600-channel SCIPP analyzer manufactured commercially by Victoreen. For the most part, an individual

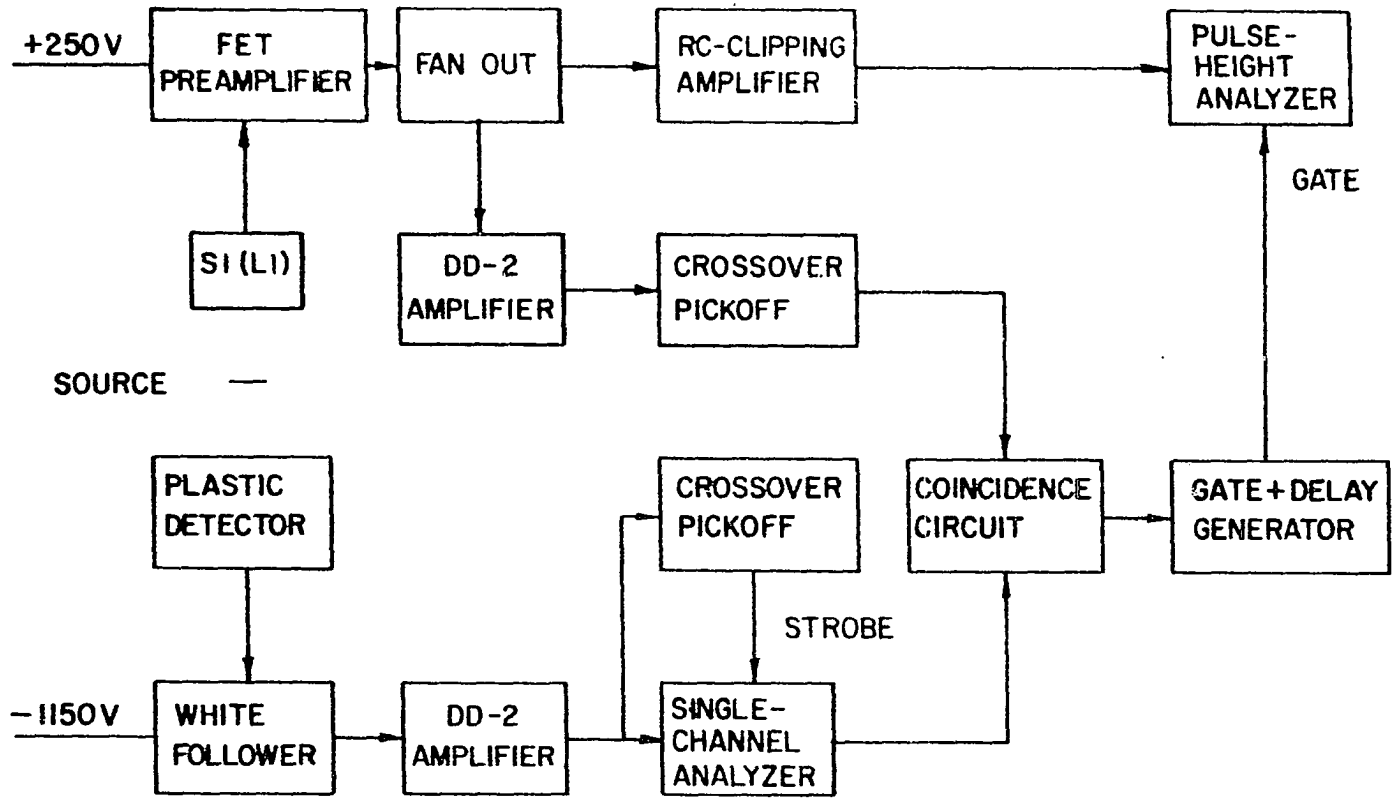

Fig. 5. Block diagram of the electronics used to record coincidences between the silicon crystal and the plastic scintillator

spectrum contained eight hundred channels; but the full 1600 channels were used when more detail was required.

A complete set of silicon coincidence data consisted of total coincidences with and without the aluminum absorber plus accidental coincidences for the case with the absorber removed. The number of accidental coincidences counted with the absorber in place was found to be very close to zero. About fifteen separate sources were required to accumulate such a complete set of data. A couple of sources were used to determine the relative numbers of electron plus photon coincidences, electron plus photon accidentals, absorber coincidences and total singles. A singles spectrum provided the shape of the accidental distribution to be subtracted from the total coincidences. Several sources served only to build the statistics of the absorber response function while counts from the remaining ten or so sources were summed together to yield a total electron plus photon coincidence spectrum with healthy statistics. The source preparation procedure was monitored to assure approximately uniform strength from source to source.

3. Silicon efficiency and monoenergetic response functions

Vacuum evaporated sources of 5.5 hr Hf^{180m} were used to measure both the relative electron efficiency of the silicon detector and the response of the detector to monoenergetic

electrons from a thin source - each as a function of incident electron energy. Figure 6 shows that the Hf^{180m} decay scheme features transitions rather evenly spaced over the region of interest from near zero energy up to about 500 keV. The 93K, 215K, 332K and 444K conversion electron lines provide four groups of monoenergetic electrons ideally suited for finding response functions at 28, 150, 267 and 378 keV since each is well separated from all other peaks. In addition, the simplicity of the decay scheme makes it possible to calculate the actual relative conversion electron intensities quite accurately.

Two different Hf^{180m} spectra were analyzed to find the efficiency and monoenergetic response of the silicon detector. The regions in each spectra near the 93K, 215K, 332K and 444K lines were first fit to an analytic function of the energy with the form

$$Y(E) = \frac{a+b(1+e^{f})\left(\frac{E}{\phi}\right)^{d}}{1+e^{f\ e^{\left(\frac{E-\phi}{c}\right)}}} + Y_{o}e^{-\frac{1}{2}\left(\frac{E-E_{o}}{\sigma}\right)^{2}}$$

where $f = cd/\phi + \ln cd/\phi$ and $\underline{a}$, b, c, d, ϕ, Y_o, σ are seven adjustable parameters. The second term simply describes the major portion of a peak by a Gaussian of height Y_o, full-width-half-maximum $2\sigma\sqrt{2\ \ln 2}$, centered at E_o. For $cd/\phi < 1$,

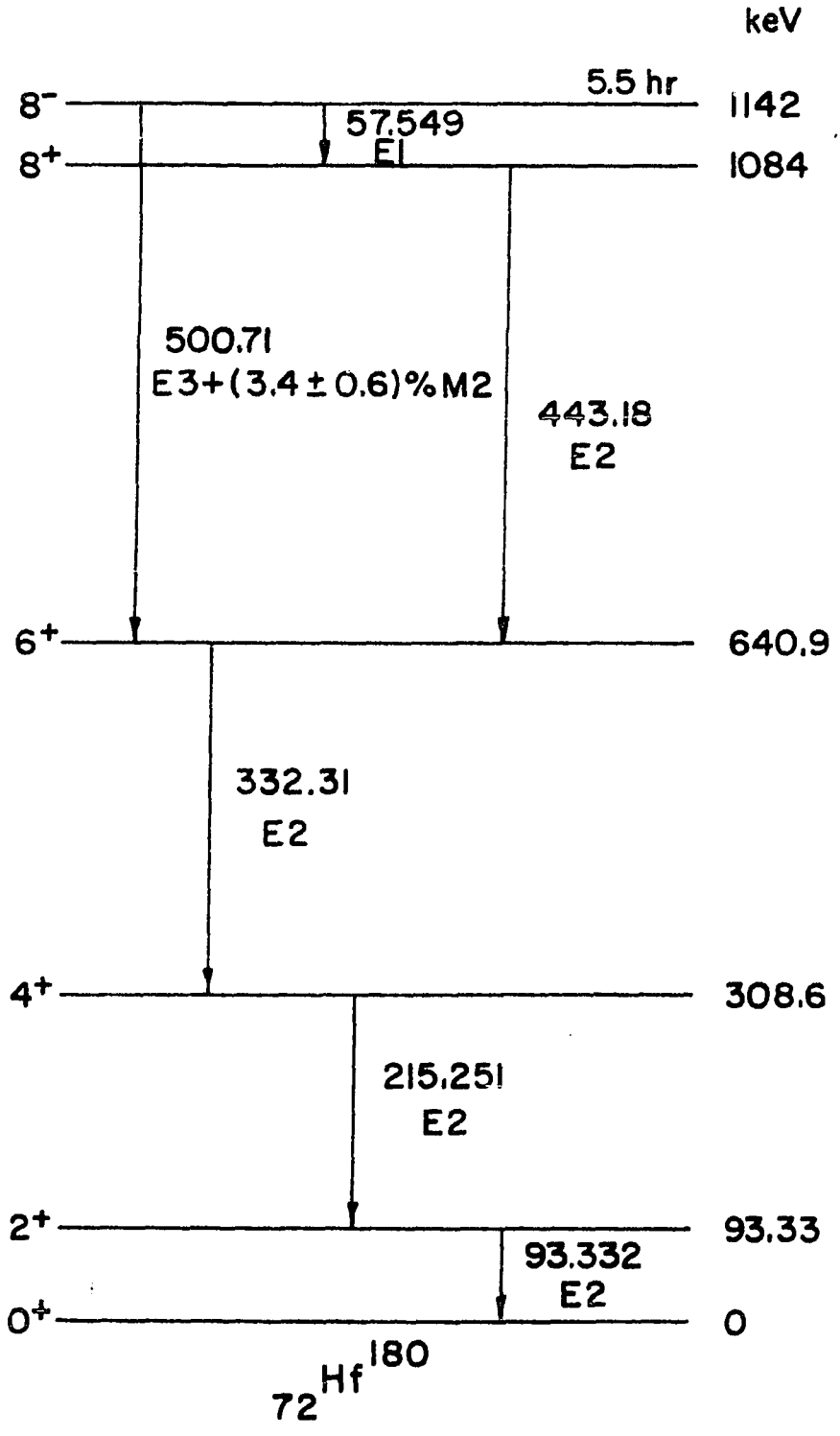

Fig. 6. Decay scheme for 5.5-hour Hf^{180m}

the first term equals a constant value a when $E \ll \emptyset$. As E nears $\emptyset$, it rises to a value a+b with a curvature specified by d. For $E > \emptyset$, this term then falls off to zero with half-width c. This rather general distribution was used to describe the non-Gaussian part of a monoenergetic response function. The first term is sometimes referred to as the scatter peak. Figure 7 shows the fit of the entire expression to the neighborhood of the 215K peak. The response function was assumed to continue with constant a down to energy zero. Figure 1 shows that the low-energy tail, while not actually constant, has little structure. Thus, the parameters a/Y_o, b/Y_o, c, d, $\emptyset$ and σ specify a normalized peak shape centered at energy E_o.

From an analysis of the 93K, 215K, 332K and 444K peaks, these parameters were found at four energies. Values were assigned to these parameters at the energies of the other Hf^{180m} peaks by interpolation or extrapolation. In this way, approximate response functions were obtained for all the Hf^{180m} lines. A separate monoenergetic response function was used for each of the L_I, L_{II}, L_{III} lines, while a single shape described all the M lines and another all the N and higher lines from a particular transition. The response functions thus generated were employed in a computer program to unfold

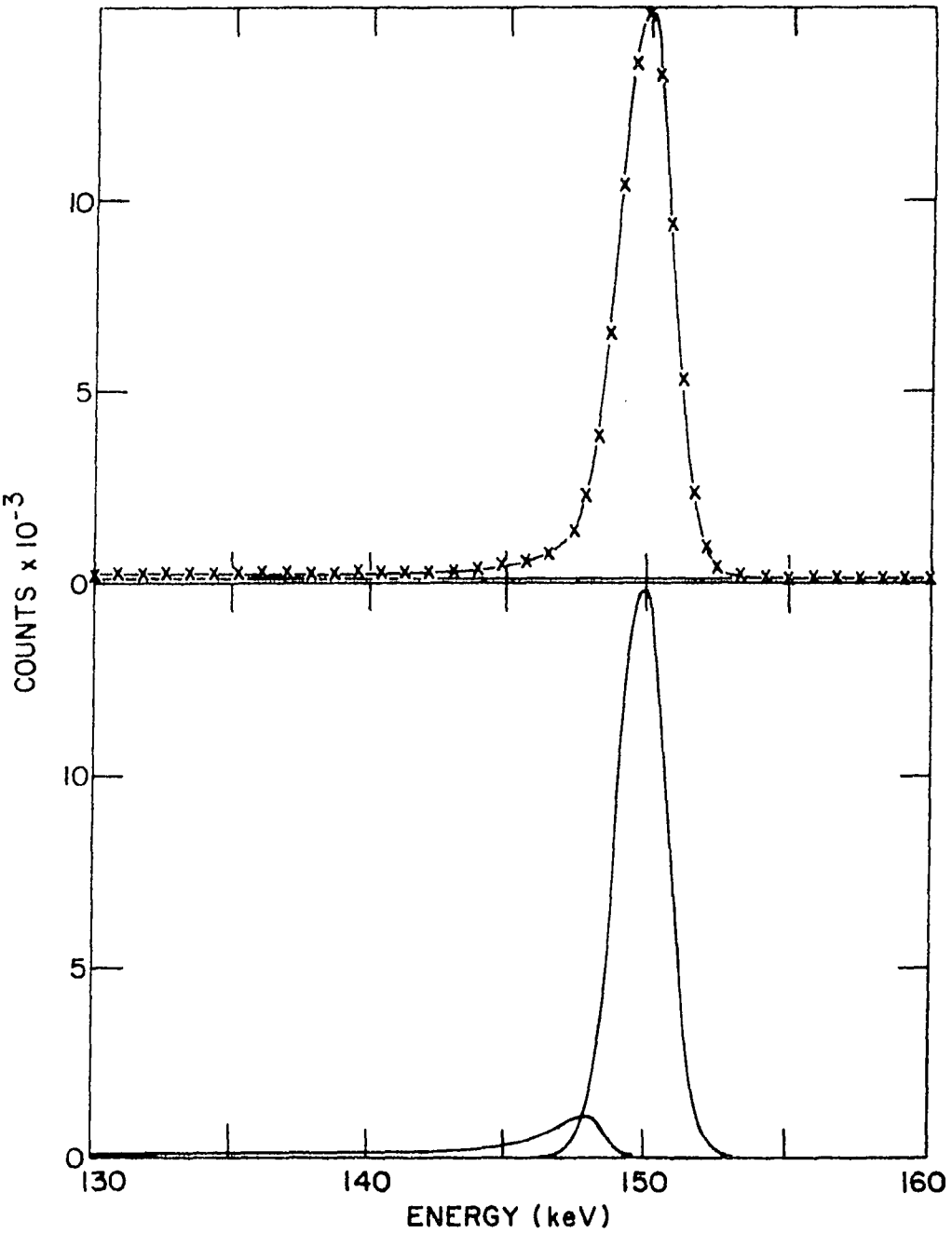

Fig. 7. Fit of analytic expression to the 215K conversion electron peak from Hf^{180m}. The contributions of the Gaussian and the scatter-peak terms after background subtraction are shown at the bottom

the Hf^{180m} spectra. The program (54) finds how much of each shape is required to give the best fit to the data in the sense of least squares. During the unfolding procedure, the dominant parameters (σ, $\underline{a}$ and to a lesser extent b) of the interpolated response functions were varied systematically in order to improve the fit. A photon response function taken with the Al absorber in place plus a 43-day Hf^{181} contaminant shape accumulated about fifty hours after preparation of a Hf^{180m} source were also included in the unfolding program. Fits with $\chi^2 = 1.90$ and 1.64 were obtained for the two Hf^{180m} spectra.

This unfolding of the Hf^{180m} spectra provided two types of information. First, it yielded reliable values for the important parameters σ, $\underline{a}$, b at a number of energies different from the original four. Figure 8 shows how the 215L line was convincingly unfolded into three monoenergetic components with the same values of σ, a/Y_o, b/Y_o. Such values of these parameters thus became "known" and were used to pin down the variations of these dominant parameters with energy. Figure 9 illustrates how the parameters c, d, $\emptyset$ (expressed as E_o-$\emptyset$) change smoothly with energy, while Figures 10 and 11 show the variation of the more important parameters σ, $\underline{a}$ (expressed as $a/\sigma Y_o$ to reflect a fraction of the Gaussian area) and b with

Fig. 8. Results of unfolding the region near the 215L peak in the Hf^{180m} spectrum. The individual response functions (solid lines) combine to give the calculated composite spectrum (dashed line) which best fits the data points (x's). The experimental relative intensities are compared with the theoretical values for an E2 transition

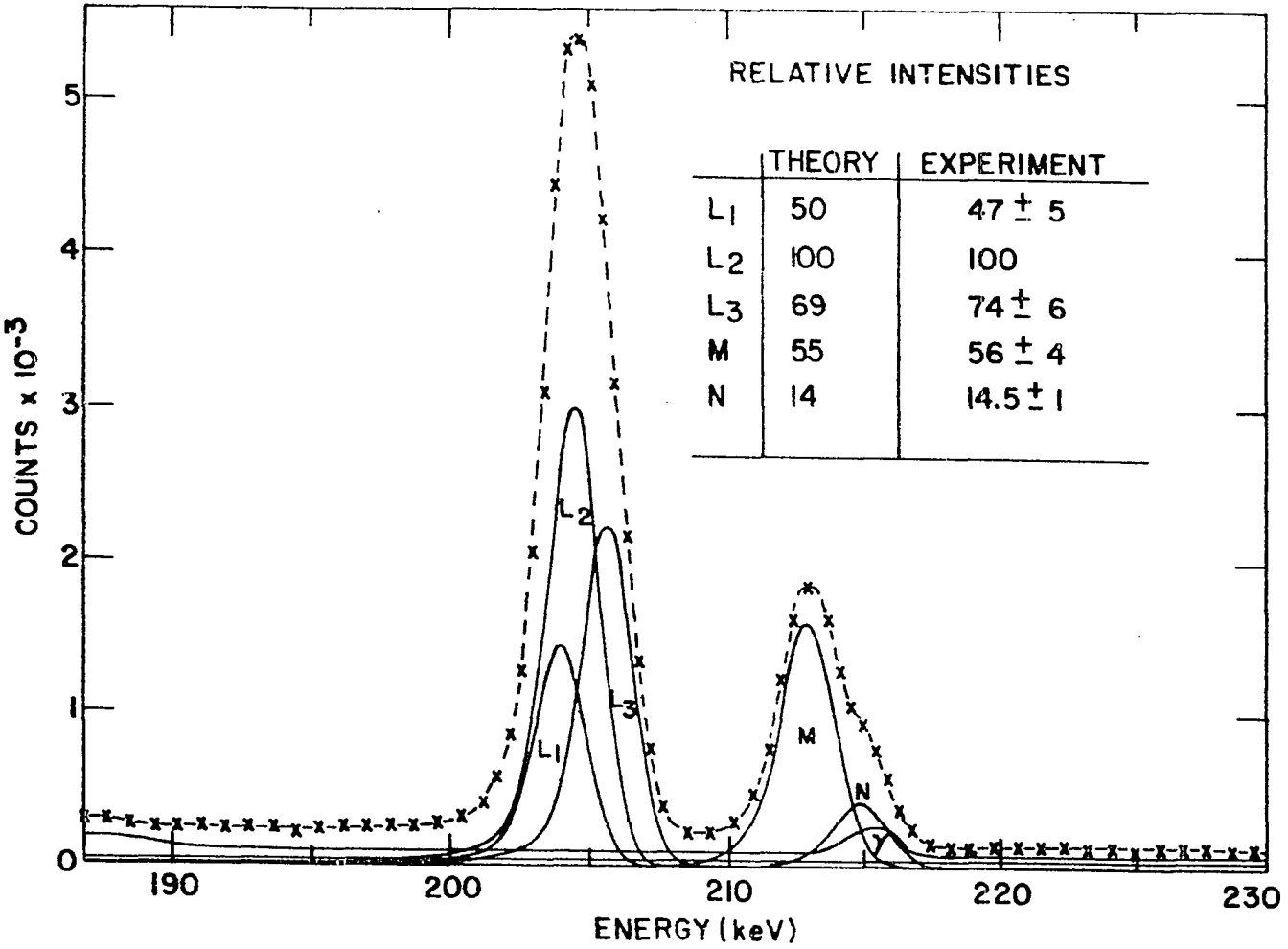
RELATIVE INTENSITIES
THEORY
EXPERIMENT
L1 50 47 ± 5
L2 100 100
L3 69 74 ± 6
M 55 56 ± 4
N 14 14.5 ± 1
COUNTS x 10-3
ENERGY (keV)
L1
L2
L3
M
N
γ

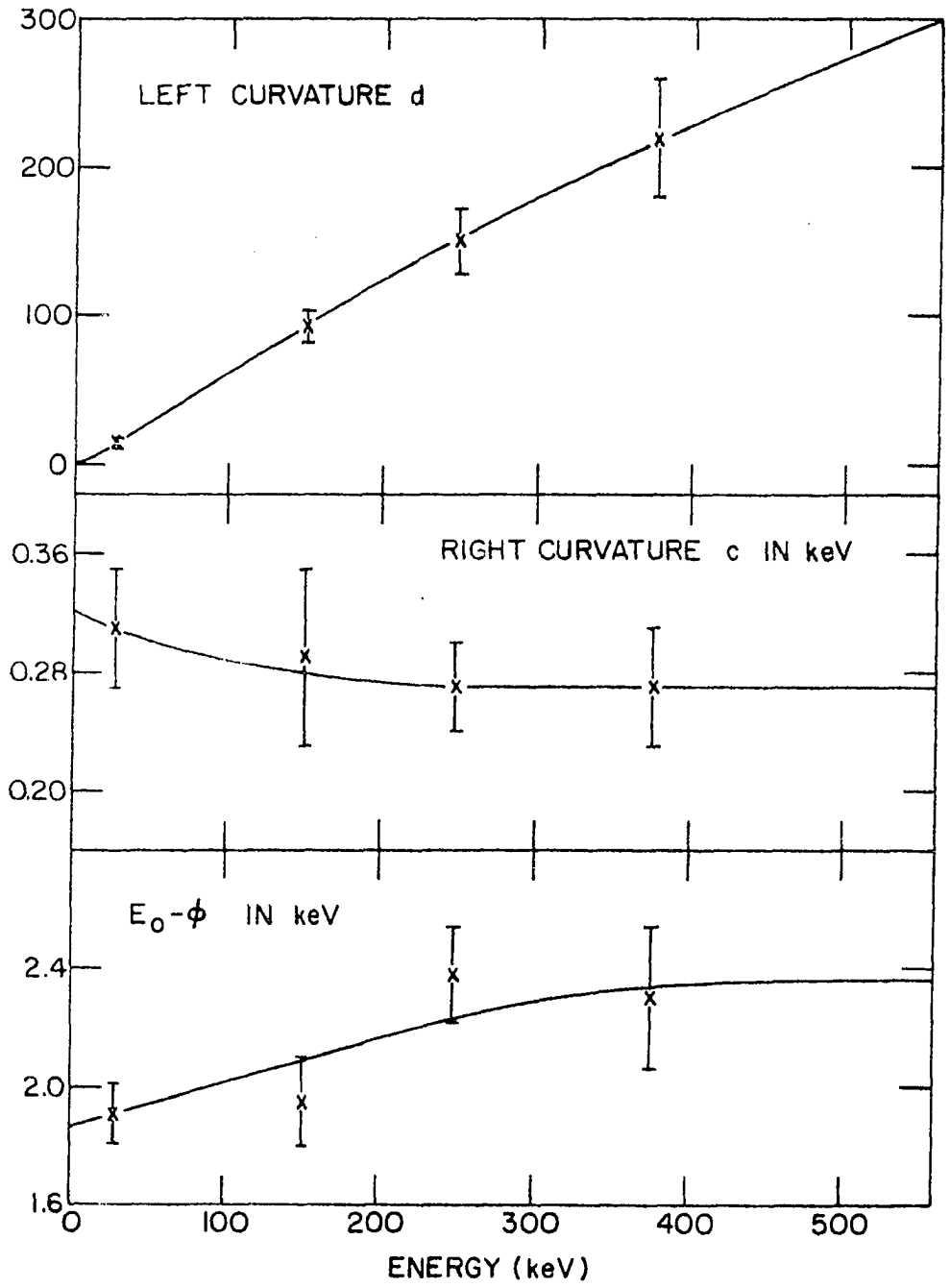

Fig. 9. The left curvature, right curvature and position of the scatter peak as functions of incident electron energy

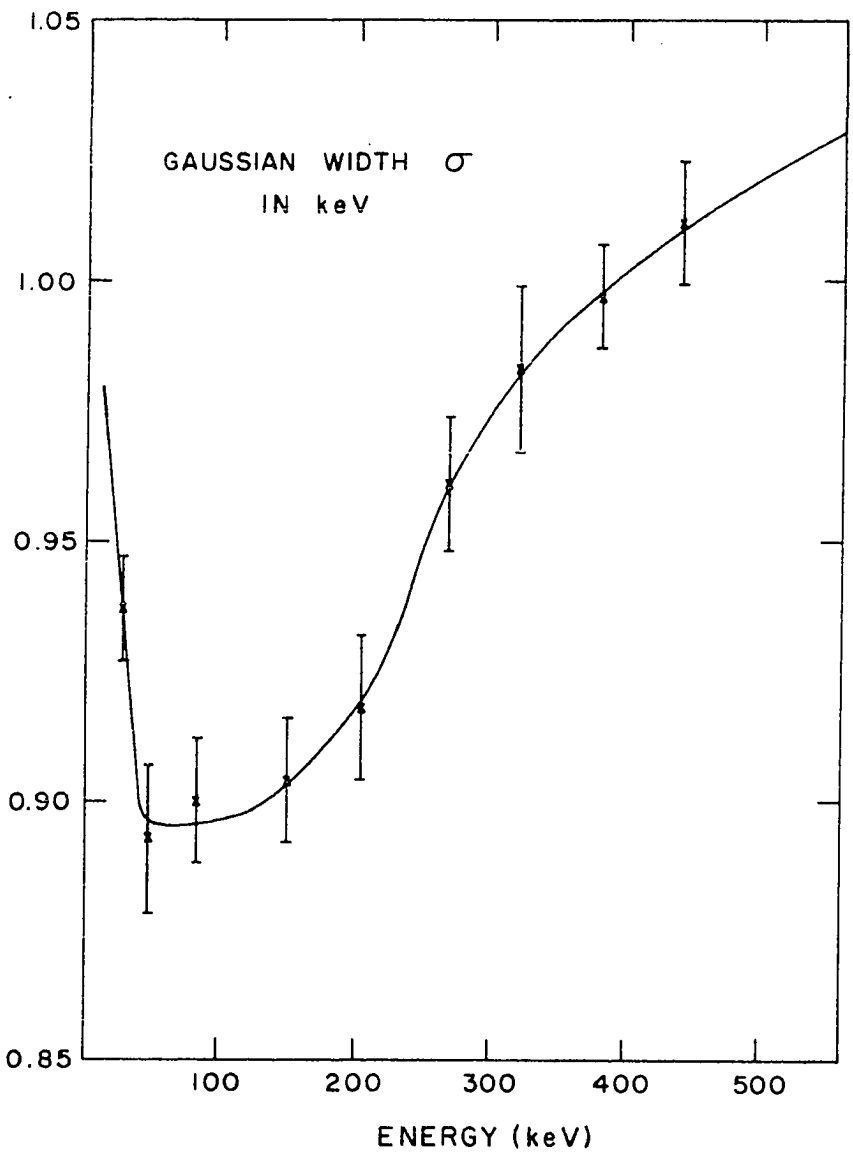

Fig. 10. The variation with incident electron energy of the standard deviation of the Gaussian term in the response function

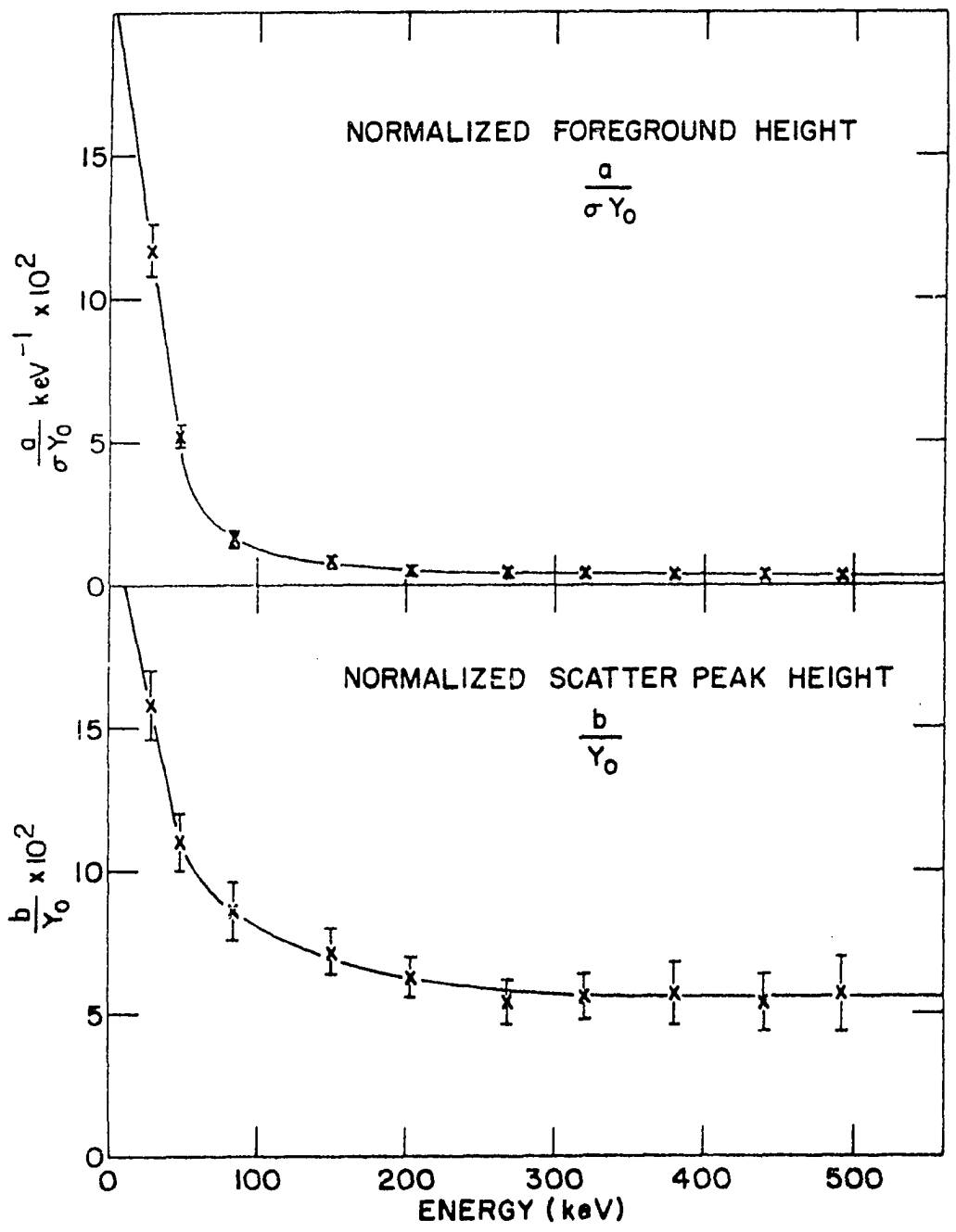

Fig. 11. The heights of the foreground and the scatter peak as functions of incident electron energy

energy. Second, the unfolded Hf^{180m} spectra provided a direct measurement of the relative intensities of the various Hf lines as seen by the silicon detector. A comparison of these measured relative intensities with the actual relative intensities of the same Hf lines then yielded the relative efficiency of the silicon detector.

The actual relative intensities of the Hf^{180m} conversion lines have been measured to 5-15% by Edwards and Boehm (63) with a magnetic spectrometer. Because of the simplicity of the Hf^{180m} decay scheme, the actual conversion electron relative intensities can be calculated if several reasonable assumptions are made. From Figure 6 the total transition intensities must be related by $I_{93} = I_{215} = I_{332} = I_{443} + I_{501} = I_{57} + I_{501}$. No crossover transitions have been found among the 0^+, 2^+, 4^+, 6^+, 8^+ levels (64,65). The 93-, 215-, 332- and 443-keV transitions all have pure E2 character. A large body of experimental data indicates that internal conversion coefficients for pure E2 transitions do not deviate from theoretical values by more than 3-5%. With one exception, we assumed the theoretical E2 conversion coefficients of Hager and Seltzer (3) for these transitions, along with the complement $\alpha_{NO...} = 0.26\alpha_M$ (66). The L_{I+II}/L_{III} ratio for the 93-keV transition was taken to be 1.28 ± 0.03 (64). We also

adopted $I_{501} = (0.148 \pm 0.008)I_{332}$ (64) for the branching ratio and E3+(3.4 ± 0.6)% M2 (65) for the multipolarity of the 501-keV transition. Finally, the values (64) $\alpha_L = 0.43 \pm 0.045$ and $\alpha_M = 0.088 \pm 0.025$ were assumed for the anomalous 57-keV transition. The intensity balance equations were then solved to yield the relative gamma-ray intensities. Table 1 compares gamma-ray intensities calculated in this manner with two direct measurements of the same relative intensities.

Table 1. Relative intensities of gamma rays from Hf^{180m}

Gamma energy (MeV)	Nelson & Hatch (67)	Edwards & Boehm (63)	Calculated
57	513 ± 20	513 ± 17	584 ± 24
93	180 ± 5	176 ± 4	181 ± 6
215	865 ± 20	882 ± 25	863 ± 6
332	1000 ± 25	1000 ± 42	1000 ± 7
443	904 ± 30	866 ± 46	879 ± 10
501	136 ± 12	180 ± 55	148 ± 8

The errors in the calculated intensities include a 3% uncertainty in the theoretical values for α_K, 4% for α_L, 5% for α_M plus the uncertainties in the assumptions above. The conversion electron intensities for each transition were found from $I_{e_i} = \alpha_i I_\gamma$ where i = K, L, M or MNO···. Table 2 compares these calculated values with those measured directly by

Table 2. Relative intensities of conversion electrons from Hf^{180m}

Transition		Actual electron intensity I_e	
		Edwards & Boehm (63)	Calculated
57	L	294 ± 12	280 ± 29
	M	72 ± 7	59 ± 10
93	K	205 ± 12	223 ± 7
	L	582 ± 17	582 ± 24
	MN	169 ± 12	172 ± 9
215	K	114 ± 5	132 ± 4
	L	72 ± 6	66 ± 3
	MN	---	21 ± 1
332	K	40 ± 1.6	47 ± 1.4
	L	15.4 ± 1.2	14.4 ± 0.6
	M	---	3.6 ± 0.2
443	K	17.3 ± 1.0	19.7 ± 0.6
	L	4.0 ± 0.5	4.8 ± 0.2
	M	1.1 ± 0.2	1.2 ± 0.1
501	K	7.0 ± 0.9	6.7 ± 0.5
	L	---	2.6 ± 0.2
	M	---	0.66± 0.05

Edwards and Boehm. The uncertainties in the calculated electron intensities are larger than those in the gamma-ray intensities because the conversion coefficients now enter in a more direct way. The purpose of the calculation was not to dispute the work of Edwards and Boehm, but rather to obtain a more

consistent set of actual electron intensities for Hf^{180m}. Hopefully, in this way, the uncertainty in the silicon relative efficiency curve could be reduced.

We measured two relative efficiency curves for the silicon detector. The first is called the relative peak efficiency curve and describes, as a function of incident electron energy, the relative probability that an incident electron will lose essentially all its energy in the detector. Such electrons show up in the peak of the corresponding response function. This efficiency curve is comparable to those given by most other workers (51,52,53,58). The second is called the total efficiency curve and describes the variation with energy of the relative probability that an incident electron will lose any of its energy in the detector. Here, the low-energy tail of the corresponding response function is included.

We define the peak area (P_e) of a response function as the Gaussian area plus the area of the hump on the low-energy side of the Gaussian. The total area (T_e) of the electron response function also includes the flat tail region. Thus,

$$P_e = \int_0^\infty \left[\frac{b(1+e^{f})\left(\frac{E}{\phi}\right)^{d}}{1+e^{\frac{(E-\phi)}{c}+f}} + Y_o e^{-\frac{1}{2}\left(\frac{E-E_o}{\sigma}\right)^2} \right] dE$$

and

$$T_e = P_e + a \int_0^{\infty} \frac{dE}{1+e^{\frac{(E-\emptyset)}{c}} + f} \quad .$$

Table 3 shows both peak and total relative efficiencies for the two sets of actual electron intensities listed in Table 2. The errors in the efficiencies include the uncertainty in the actual relative intensities, the uncertainty due to the statistics of the unfolding routine plus the three percent uncertainty in the area of the response functions used by the computer. The silicon efficiency curves based on the calculated values of the actual Hf^{180m} electron intensities (columns 3 and 5 in Table 3) are shown in Figure 12. Peak efficiency data obtained with Te^{123m} and Tm^{170} is also included to define better the variation of the curve at low energies. The actual Te^{123m} relative intensities were taken from the work of Chu et al. (68,69) while the Tm^{170} intensities were based on theoretical conversion coefficients for the 84.3-keV E2 transition. The silicon efficiency curves should be accurate to four percent overall. The fact that the total efficiency curve is approximately constant illustrates that almost no electrons in this energy range pass through the detector without losing some energy. This should

Table 3. Peak and total efficiencies for the silicon detector

Transition	Peak efficiency		Total efficiency	
	Edwards (63)	Calculated	Edwards (63)	Calculated
57 L	79.7 ± 4.0	91.2 ± 9.8	0.848 ± 0.043	0.970 ± 0.102
M	84.3 ± 8.5	99.3 ± 15.1	0.879 ± 0.090	1.035 ± 0.163
93 K	75.3 ± 4.9	75.0 ± 3.3	1.062 ± 0.070	1.034 ± 0.045
L	88.0 ± 3.7	95.5 ± 4.8	0.924 ± 0.038	0.979 ± 0.050
MN	98.9 ± 7.6	105.5 ± 6.3	1.045 ± 0.080	1.088 ± 0.065
215 K	105.3 ± 5.6	99.1 ± 4.1	1.090 ± 0.058	0.998 ± 0.042
L	84.0 ± 7.5	99.9 ± 5.4	0.846 ± 0.076	1.006 ± 0.054
MN	---	99.5 ± 5.5	---	1.002 ± 0.055
332 K	107.4 ± 5.4	99.6 ± 4.1	1.062 ± 0.052	0.985 ± 0.042
L	86.4 ± 7.3	100.8 ± 5.1	0.859 ± 0.074	1.002 ± 0.053
M	---	101.4 ± 63	---	1.023 ± 0.064
443 K	104.3 ± 6.7	99.9 ± 4.2	1.037 ± 0.069	0.990 ± 0.042
L	114.2 ±14.6	103.8 ± 5.2	1.122 ± 0.146	1.020 ± 0.051
M	102.7 ±18.9	100.7 ± 8.8	1.010 ± 0.190	0.990 ± 0.085
501 K	86.9 ±11.5	99.0 ± 7.9	0.854 ± 0.110	0.973 ± 0.075
L	---	99.5 ± 8.3	---	0.992 ± 0.084
M	---	104.4 ± 8.9	---	1.041 ± 0.088

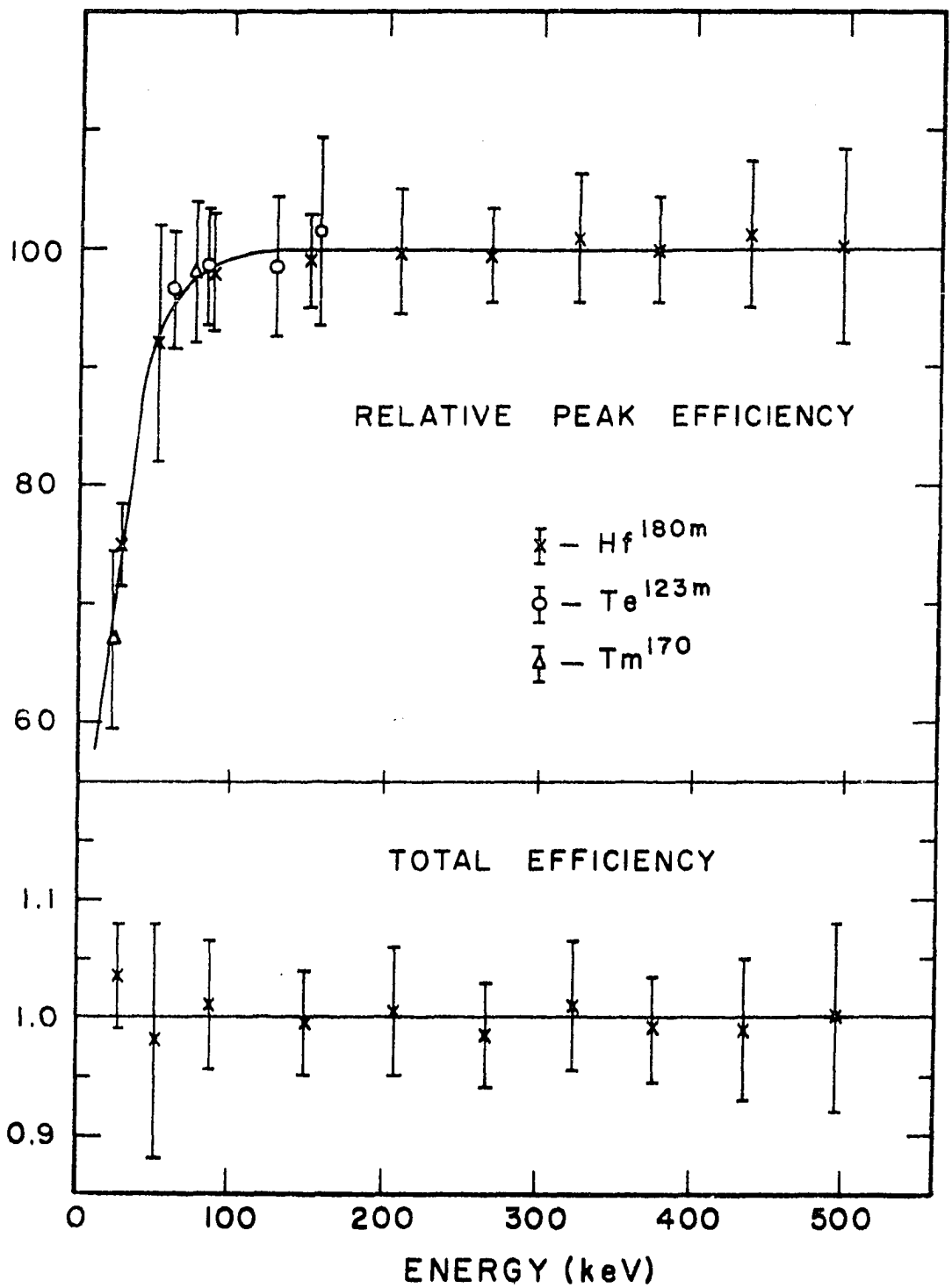

Fig. 12. Efficiency curves for the silicon detector

be the case since 2 mm of silicon corresponds to the range of 1 MeV electrons. The agreement found here lends support to the contention that the analytic response functions used provide a good description of the actual response of the silicon detector to monoenergetic electrons from a thin source.

Several strong conversion electron peaks from liquid-deposited sources of Sm^{155} and Nd^{151} were fit to the same analytical expression to test if source preparation technique influenced the electron response functions. Only the Gaussian width σ was affected, and that was increased by only 1-2% except for electron energies below 40 keV where low-energy tailing due to source thickness became apparent. It was impractical to fit separate response functions to each L and M line for any but the strongest transitions in the decays of Sm^{155} and Nd^{151}. Instead a single response function represented the three L-shell peaks and another the five M-shell peaks. The exact relation between such an effective response function and the monoenergetic response function for the average energy of the peaks depends on the subshell ratios and the multipolarity of the particular transition. From a study of the Hf^{180m} and Te^{123m} spectra, it was found that a general effective response function could be generated by

increasing the Gaussian width σ and decreasing the scatter peak height b by 6% for L-shell peaks and 3% for M-shell peaks. Several conversion electron peaks were found in Nd^{151} spectra at energies greater than 500 keV. The efficiency of the silicon detector was extended to these higher energies by calibration with a vacuum evaporated Ag^{110m} source. The conversion electron relative intensities for Ag^{110m} have been measured with magnetic beta-ray spectrometers by Suter et al. (70), Newbolt and Hamilton (71) and Moragues et al. (72). The silicon peak efficiency curve for electron energies up to about 900 keV is shown in Figure 13a. The same figure (b,c) includes peak efficiency curves for two other lithium-drifted silicon detectors which were used in the direct internal conversion coefficient measurements described in the next section. All three detectors had the same dimensions (2 mm depletion depth by 80 mm^2 surface area) and were manufactured by the same TMC-Kevex group. The peak efficiency curves actually appear quite similar, especially compared to the unexplained variations from detector to detector seen by other workers (52).

In summary, the relative intensities of conversion electrons from the decays of Sm^{155} and Nd^{151} were measured with a

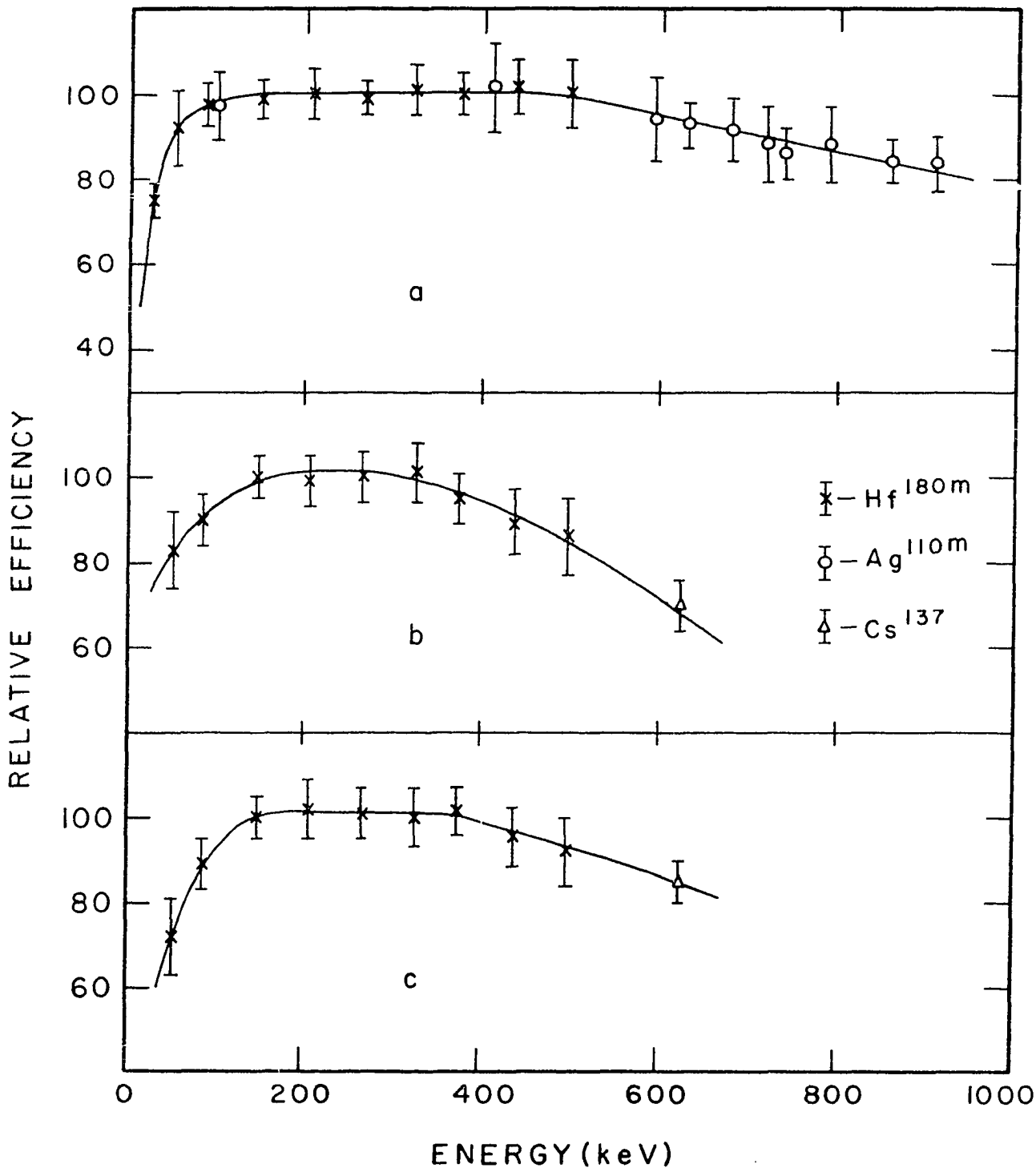

Fig. 13. Relative peak efficiency curves for three different silicon detectors used in the work reported here

lithium-drifted silicon detector. While intensities of the stronger conversion peaks could be obtained from singles spectra, only the coincidence method allowed some weak electron peaks to be observed. The development of monoenergetic response functions from a study of the electron spectrum of Hf^{180m} permitted the Sm^{155} and Nd^{151} coincidence spectra to be unfolded by a linear least-squares computer routine.

B. Direct Internal Conversion Coefficient Measurements

The standard internal conversion coefficients required by the normalized conversion electron to gamma-ray method were measured in two basic ways. The K-shell conversion coefficient of the 104-keV transition in the decay of Sm^{155} could be measured by the K x-ray to gamma-ray ratio method since the overwhelming majority of the Sm^{155} decays proceed through this transition. The second method used is a simple modification of the normalized conversion electron to gamma-ray method itself. The conversion electrons and gamma rays from Sm^{155} or Nd^{151} are counted simultaneously by separate detectors. Nuclides having transitions with well known internal conversion coefficients are used to normalize the efficiencies of the two detectors in the dual spectrometer so the standard Sm^{155} or Nd^{151} conversion coefficient is just the ratio of

the measured electron and gamma-ray intensities. All the Sm^{155} and Nd^{151} conversion coefficients could be measured in this way if the continuous beta-ray distribution did not mask many conversion electron peaks.

1. Gamma-ray singles measurement

The fact that gamma rays interact in the intrinsic region of a silicon detector complicates the study of electrons with a silicon detector. However, this does allow the silicon crystal to be used as a low-efficiency gamma detector if the incident electrons can be blocked out with an absorber. Commercial silicon photon spectrometers are available from both Kevex Corporation and Ortec Incorporated with quoted resolutions of about 300 eV for 6.4 keV x-rays. In the work reported here, the same semiconductor crystal used to study the electron relative intensities was converted to a photon detector by simply fixing the aluminum absorber in position between the source and collimator. The resolution obtained was about 1.6 keV for 50-100 keV photons. The relative peak efficiency of the silicon crystal for photons was calibrated with Yb^{169}, Tm^{170} and Cd^{109} sources. The relative intensities used as standards are those of Alexander and Boehm (73) and Brown and Hatch (74) for Yb^{169}, Nelson and Hatch (18) for

Tm^{170} and Lentz et al. (75) and Donnelly and Wiedenbeck (76) for Cd^{109}. The intensity of the 20-keV gamma ray from Yb^{169} was deduced from the required intensity balance in the decay scheme, the conversion electron subshell ratios of Shliagan and Samoilov (77) plus the theoretical internal conversion coefficients of Hager and Seltzer (3). Thus the point in the efficiency curve at 20 keV has a large (20%) error. Figure 14 shows the measured relative peak efficiency as a function of energy. The uncertainty over the entire range of the curve is about six percent.

The areas of photon peaks in the silicon detector were found from a computer routine written by L. M. Taff (78) of this laboratory. The computer program searches a spectrum, locates the peaks, and fits the region of each peak to a Gaussian function plus a quadratic background. Figure 15 illustrates that the response of the silicon semiconductor detector to monoenergetic photons was actually quite Gaussian.

The silicon photon spectrometer was used to measure the intensities of several low-energy gamma rays from Sm^{155} and Nd^{151} as well as to determine the K-shell internal conversion coefficient of the 104-keV transition in the decay of Sm^{155} by the K x-ray to gamma-ray ratio method. As explained in

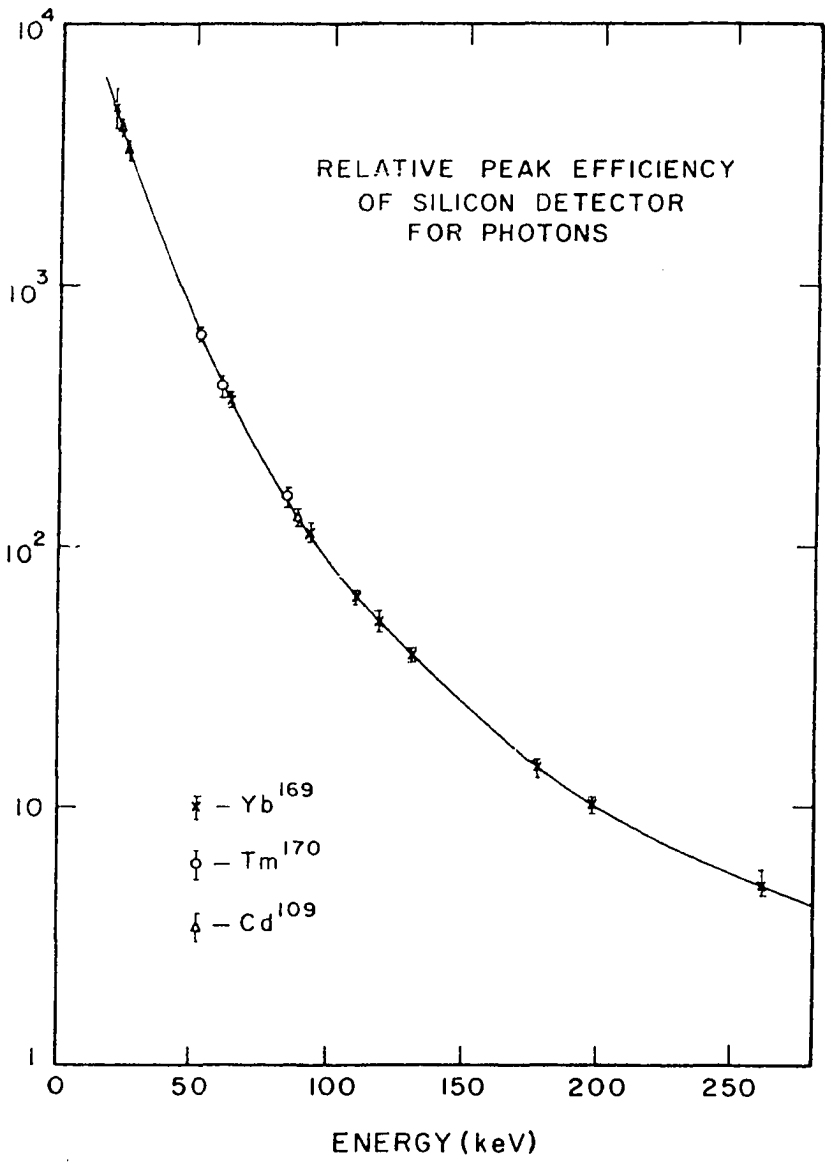

Fig. 14. Relative Gaussian peak efficiencies of the silicon detector for low-energy photons

Fig. 15. Portions of a Yb^{169} photon spectrum as seen with the silicon detector. Solid lines show both the Gaussian fits to the peaks and the accompanying quadratic fits to the local background

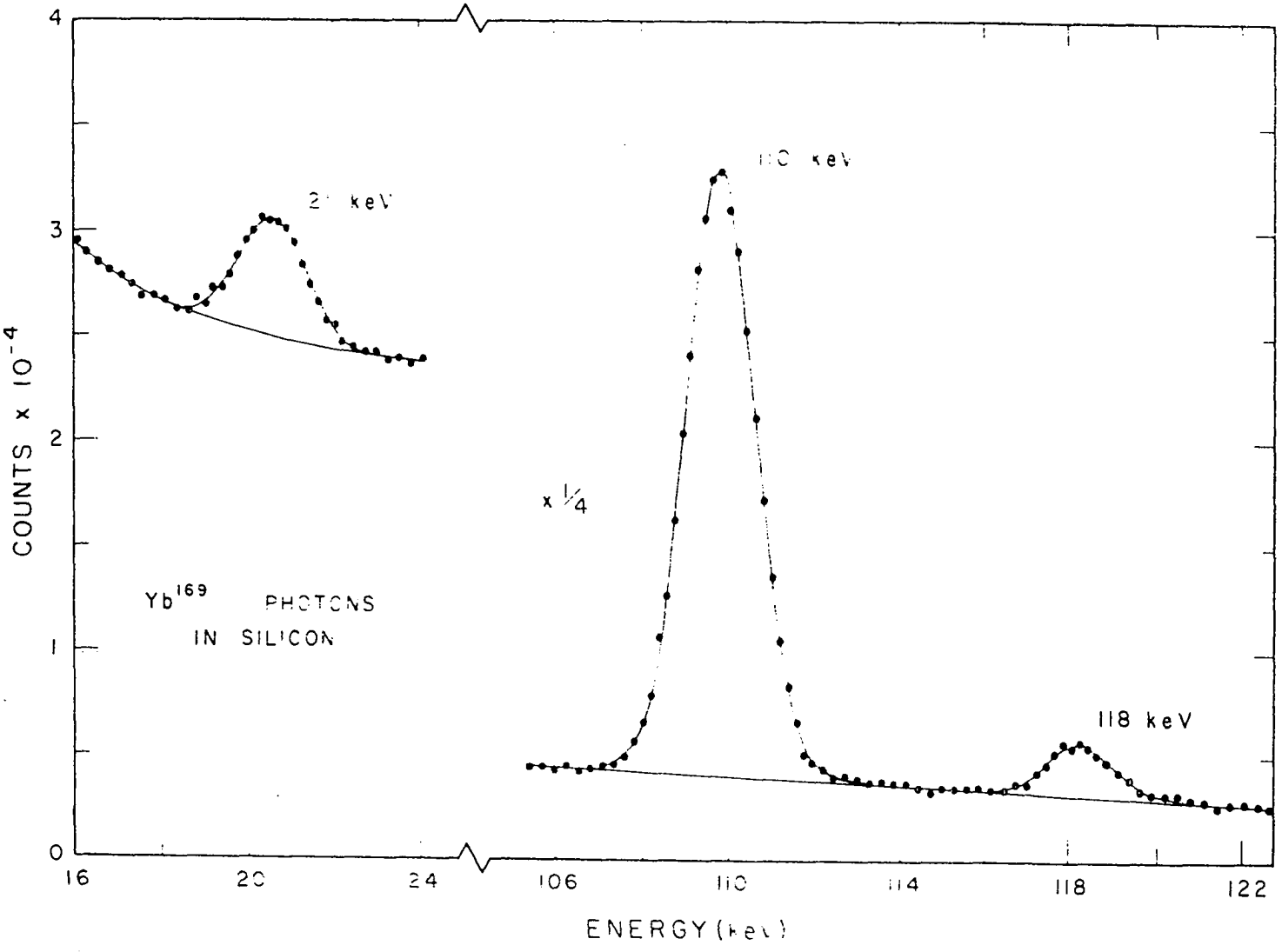
4
3
2
1
0
COUNTS x 10^{-4}
21 keV
110 keV
x 1/4
Yb^{169} PHOTONS
IN SILICON
118 keV
16
20
24
106
110
114
118
122
ENERGY (keV)

the first chapter, this method gives the K-shell conversion coefficient for a particular transition as

$$\alpha_K = \frac{I_{K_x}}{\omega_K I_\gamma}$$

where I_{K_x} is the intensity of the K x-rays that follow internal conversion of the transition in question. When K x-rays also arise from conversion of other transitions, then $I_{K_x} = R_K I_{K_x}^T$ where $I_{K_x}^T$ is the total K x-ray intensity due to internal conversion and R_K is the fraction of all K-shell conversion electrons which accompany the transition considered. Thus,

$$\alpha_K = \frac{R_K I_{K_x}^T}{\omega_K I_\gamma}$$

where an electron relative intensity measurement is required to find R_K. If almost all the K-shell internal conversion occurs in a single strong transition, then R_K is almost unity for that transition, and an accurate value of its conversion coefficient can be obtained. Such is the case for the 104-keV transition in the decay of Sm^{155}. No single transition dominates the decay of Nd^{151} so that it is difficult to sort out accurately the various contributions to the total K x-ray intensity.

2. Simultaneous measurement of conversion electron and gamma-ray singles

This method was outlined in the introduction to this section and has been discussed in detail by Hollander (51) and Haverfield (52). In the work described here, two different experimental arrangements were employed to count conversion electrons and gamma rays in separate detectors at the same time. Conversion electrons were counted by a lithium-drifted silicon detector in each of the two spectrometers. The gamma rays, however, were detected with a NaI(Tl) crystal in one spectrometer and a lithium-drifted germanium semiconductor in the other.

The first arrangement was constructed around the same vacuum chamber used in measuring coincidences between conversion electrons and high-energy beta rays. The 2mm x 80mm^2 silicon detector was purchased commercially as a TMC model W80-2AA. Its relative peak efficiency at a bias of 200 volts is shown in Figure 13b. A 3x3 inch integral line NaI(Tl) scintillation detector, manufactured by Harshaw Chemical, counted the gamma rays. It was placed in the same port of the vacuum chamber that the plastic crystal occupied during the coincidence experiment. Now, however, the source-to-

detector distance was fixed at 6 cm to reduce the NaI counting rate. Also, 0.159 cm of aluminum was erected between source and NaI detector. The gamma-ray attenuation coefficients of Davisson (79) were used to correct for photons stopped in the aluminum walls. The resolution of the NaI crystal was about 13% at 100 keV. The NaI pulses were analyzed in a 400 channel RIDL model 34-12B pulse-height analyzer which was synchronized with the Victoreen SCIPP analyzer so that the counting of conversion electrons and gamma rays could begin simultaneously.

The relative peak efficiency for the NaI detector was interpolated from the work of Lazar et al. (80) and extrapolated to lower energies through the combination of a measured peak-to-total ratio for the 88-keV gamma ray in Cd^{109} and the total efficiency calculated by Vegors et al. (81) for this energy and geometry. The contribution of the iodine escape peak at low energies was found from the approximate formula of Axel (82). Figure 16 shows both the NaI relative peak efficiency and the ratio of the iodine escape peak to the Gaussian full-energy peak. The total efficiency calculations of Vegors were not used exclusively because of the possibility of gamma rays scattering into the NaI crystal from the surrounding material. The relative peak efficiency curves for the silicon

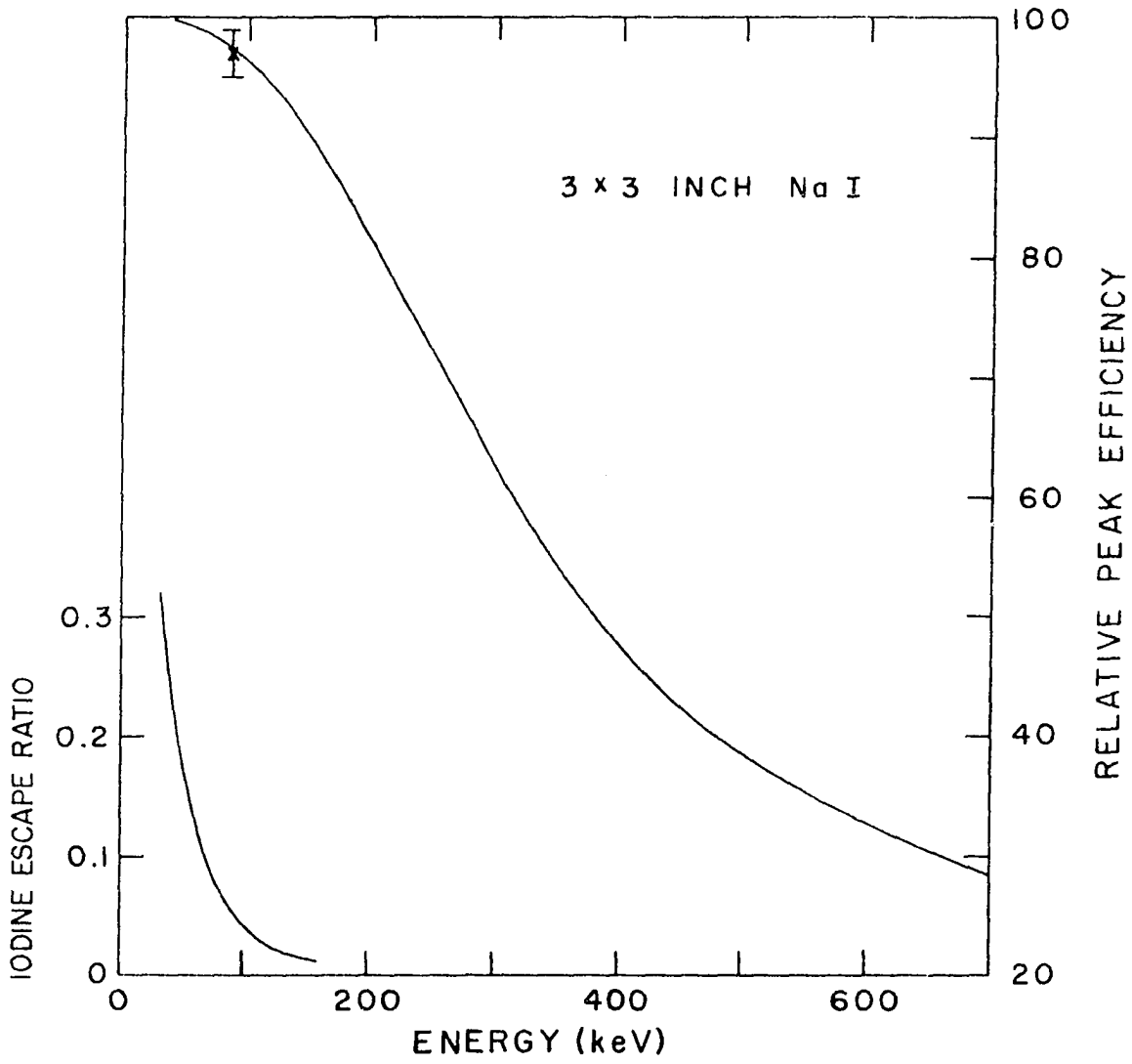

Fig. 16. Relative peak efficiency of the NaI crystal plus the ratio of iodine escape peak to Gaussian full-energy peak as functions of gamma-ray energy

and NaI detectors were related to each other through the well-known internal conversion coefficients of the 88-keV transition in the decay of Cd^{109} and the 159-keV transition from Te^{123m}. The measured K-shell conversion coefficient (83) for the 662-keV transition in the decay of Cs^{137} then allowed the placement of the point at 625 keV on the silicon peak efficiency curve in Figure 13b. The total uncertainty in the normalized efficiency of the dual NaI-silicon spectrometer was about seven percent due to the combined effects of the five percent uncertainty in the silicon relative peak efficiency, the three percent uncertainty in the NaI relative peak efficiency and the three percent uncertainty in the normalizing conversion coefficients.

The poor resolution of the NaI detector makes such a dual spectrometer arrangement far less than ideal. The virtue of the NaI crystal is that its efficiency can be calculated accurately. Thus, the intensities of relatively isolated peaks can be determined all right; but the poor resolution does not permit accurate intensity measurements for closely spaced peaks. In this work, only a single peak intensity had to be obtained for each Sm^{155} or Nd^{151} spectrum so that the poor NaI resolution was not a complete handicap.

The second dual spectrometer experiment was performed in an entirely new vacuum chamber. The chamber was designed as a versatile electron and gamma-ray spectrometer for use on-line with the isotope separator at the Ames Laboratory Research Reactor. Two movable silicon detectors could be accommodated inside the chamber while two ports were available for gamma-ray detectors. More complete details are given by Taff (84).

The second simultaneous singles experiment incorporated a lithium-drifted germanium detector in order to separate gamma-ray peaks that overlapped in a NaI spectrum. The 23 cc germanium crystal was borrowed from Dr. Tucker of this laboratory and had a resolution of 2.5 keV for 1200-keV photons. A third 2 mm x 80 mm^2 silicon detector (again, TMC model W80-2AA) counted the conversion electrons. A Hf^{180m} source was used to calibrate the relative peak efficiencies of both the silicon and germanium detectors and to normalize the electron and gamma-ray efficiencies. The silicon efficiency curve is shown in Figure 13c and the germanium curve in Figure 17. The measured gamma-ray intensities for Sm^{155} (61) and Nd^{151} (62) were used to fill in the low-energy behavior of the germanium efficiency and Cs^{137} provided each curve with an extrapolated

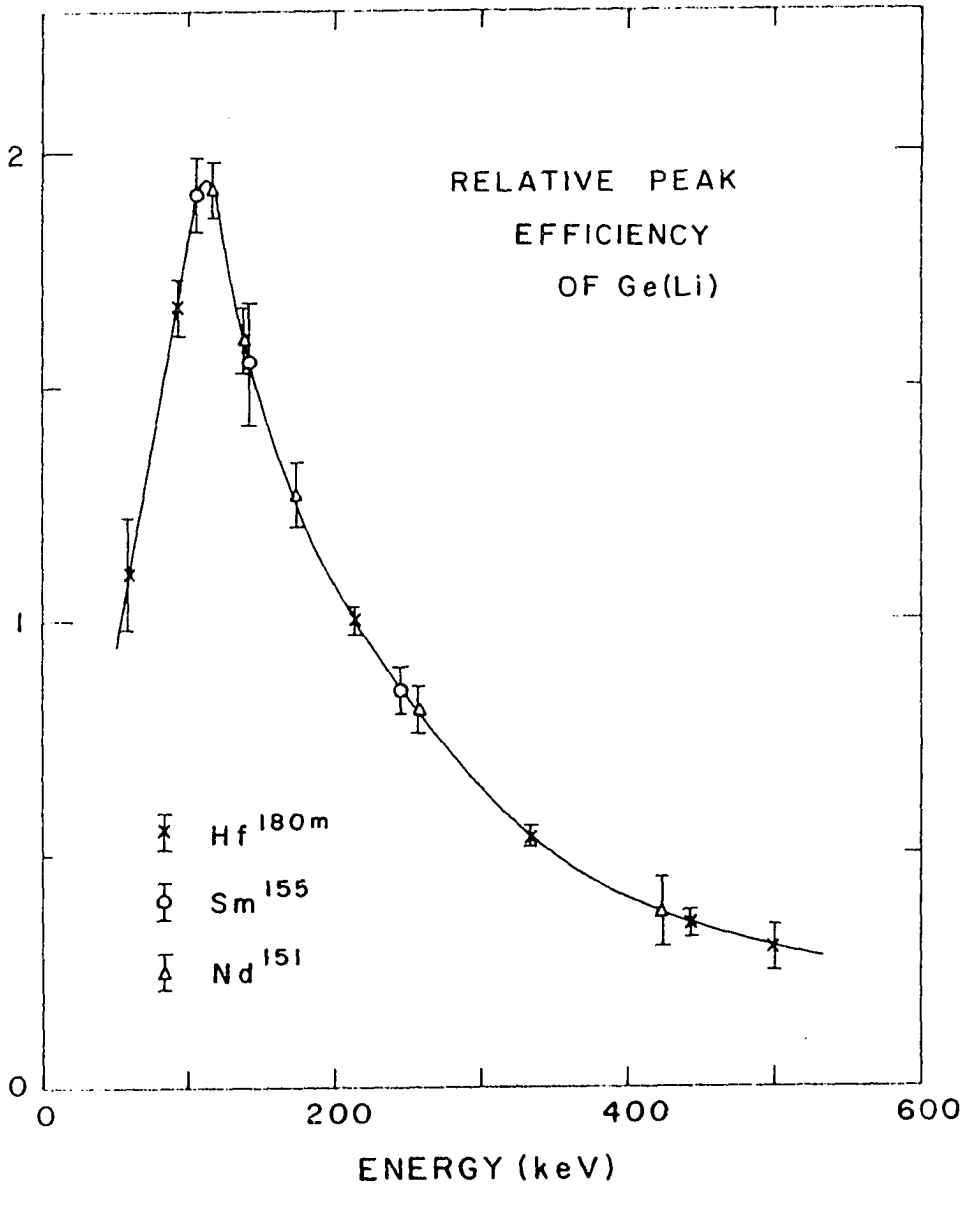

Fig. 17. Relative Gaussian peak efficiency of germanium detector for gamma rays

efficiency point at higher energy. The total uncertainty in the efficiency of the electron gamma-ray spectrometer was estimated at eight percent due in part to the slight possibility of inconsistencies in the Hf^{180m} conversion coefficients (67).

Both the silicon and germanium detectors were connected via Tennelec TC 130 preamplifiers and TC 200 amplifiers to a 4K channel TMC pulse-height analyzer with a dual ADC and separate timers. The counting rates of the two detector systems were approximately equal so that the effect of the deadtime on the effective source strength was negligible even for short-lived Sm^{155} and Nd^{151}.

In summary, standard conversion coefficients for Sm^{155} and Nd^{151} were measured by the normalized conversion electron to gamma-ray ratio method with two different spectrometers. Silicon detectors counted conversion electrons in each spectrometer while one employed a lithium-drifted germanium crystal to count gamma rays and the other used a NaI scintillator. In addition, the relative intensities of the K x-ray and the 104-keV gamma ray in the decay of Sm^{155} were found from the NaI singles spectra. This last measurement allowed still another determination of the K-shell internal conversion coefficient

of the 104-keV transition in the Sm^{155} decay by the x-ray to gamma-ray ratio method as explained earlier in this section.

C. Sources

Samarium and neodymium source material was purchased commercially from Oak Ridge National Laboratory in the form of samarium oxide enriched in Sm^{154} and neodymium oxides enriched in Nd^{148} or Nd^{150}. The isotopic concentration of the enriched samples is indicated below. The enriched Sm^{154} sample contained $<0.01\%$ Sm^{144}, 0.08% Sm^{147}, 0.07% Sm^{148}, 0.21% Sm^{149}, 0.05% Sm^{150}, 0.38% Sm^{152}, 99.21% Sm^{154}; the Nd^{148} sample 1.0% Nd^{142}, 0.59% Nd^{143}, 1.38% Nd^{144}, 0.77% Nd^{145}, 2.28% Nd^{146}, 92.93% Nd^{148}, 1.06% Nd^{150}; and the Nd^{150} sample 1.46% Nd^{142}, 1.00% Nd^{143}, 1.52% Nd^{144}, 0.91% Nd^{145}, 1.51% Nd^{146}, 1.09% Nd^{148}, 92.5% Nd^{150}. The rare-earth oxides were converted to soluble nitrates by adding excess HNO_3 and heating to dryness. The nitrates were dissolved in alcohol and a few drops of the resulting solution were encapsulated in 3/64 inch polyethylene tubing for irradiation. The radioactive Sm^{155}, Nd^{149} and Nd^{151} samples were produced by n-γ reaction with a flux of 4×10^{13} neutrons/cm^2-sec in one of the pneumatic ports at the Ames Laboratory Research Reactor. Typical irradiation times were approximately one half-life. The short-

lived samarium and neodymium sources were deposited as a liquid from the alcohol solutions onto aluminized or clear 1/4 mil mylar. Low heat quickly evaporated the alcohol so source preparation times of less than one minute from the end of the irradiation could be achieved. The Sm and Nd source strengths were restricted to approximately 2-5 μc to prevent swamping the detectors. The Hf^{180m}, Yb^{169}, Ag^{110m} and Cd^{109} calibration sources were vacuum evaporated from tungsten or tantalum boats onto 1.75 mg/cm^2 aluminum foil, while isotopically pure calibration sources of Tm^{170} and Te^{123m} were deposited on similar aluminum foils at the Ames Laboratory isotope separator.

III. MEASUREMENTS AND RESULTS

Once more we outline our procedure for studying the decays of shortlived Sm^{155} and Nd^{151}. The essential features of a decay scheme plus the gamma-ray relative intensities have been found by others, principally from germanium detector work. The silicon crystal is used as a photon detector to check the intensities of the low energy gamma rays and to measure the K x-ray to gamma-ray ratio for the strongest gamma ray in each decay. The conversion coefficient of a standard transition in each decay is measured by the simultaneous counting of electrons in silicon and gamma rays in NaI or germanium. Then the silicon singles electron spectra are analyzed to determine the relative intensities of those conversion electron peaks in each decay which can be seen above the continuous beta-ray distribution. The internal conversion coefficients corresponding to these strong conversion electron lines can now be found. The relative intensities of some weaker conversion electron peaks in each decay are then deduced from the silicon coincidence data. By now enough is known of the particular decay scheme to correct for the complexity introduced by beta-ray branching. As explained in Appendix III, angular correlation effects are neglected. Finally, internal conversion

coefficients deduced for all observed transitions in each decay are used to find the transition multipolarities and to explain some characteristics of the levels in the decay scheme.

A. Sm^{155}

The 22-minute decay of Sm^{155} to Eu^{155} was first studied by Schmid and Burson (85), who arranged three strong gamma rays into a simple crossover-stopover pattern. The Sm^{155} decay scheme was extended by the germanium work of Funke *et al.* (61) to include thirty-four transitions among eleven nuclear energy levels in Eu^{155}. Figure 18 shows the portion of the decay scheme which is of interest in the present work. Agin *et al.* (86) repeated the study of the Sm^{155} decay with germanium detectors and Nelson and Hatch (18) measured the relative intensities of the three strongest gamma rays with a bent-crystal spectrometer. After the initial report (87) of the work described here, Widemann and Sebille (88) published both gamma-ray relative intensities obtained with a germanium detector and conversion electron relative intensities measured with a magnetic spectrograph.

1. Photon intensities and standard conversion coefficient

Table 4 lists four sets of measurements of the relative intensities of the gamma rays considered in this work.

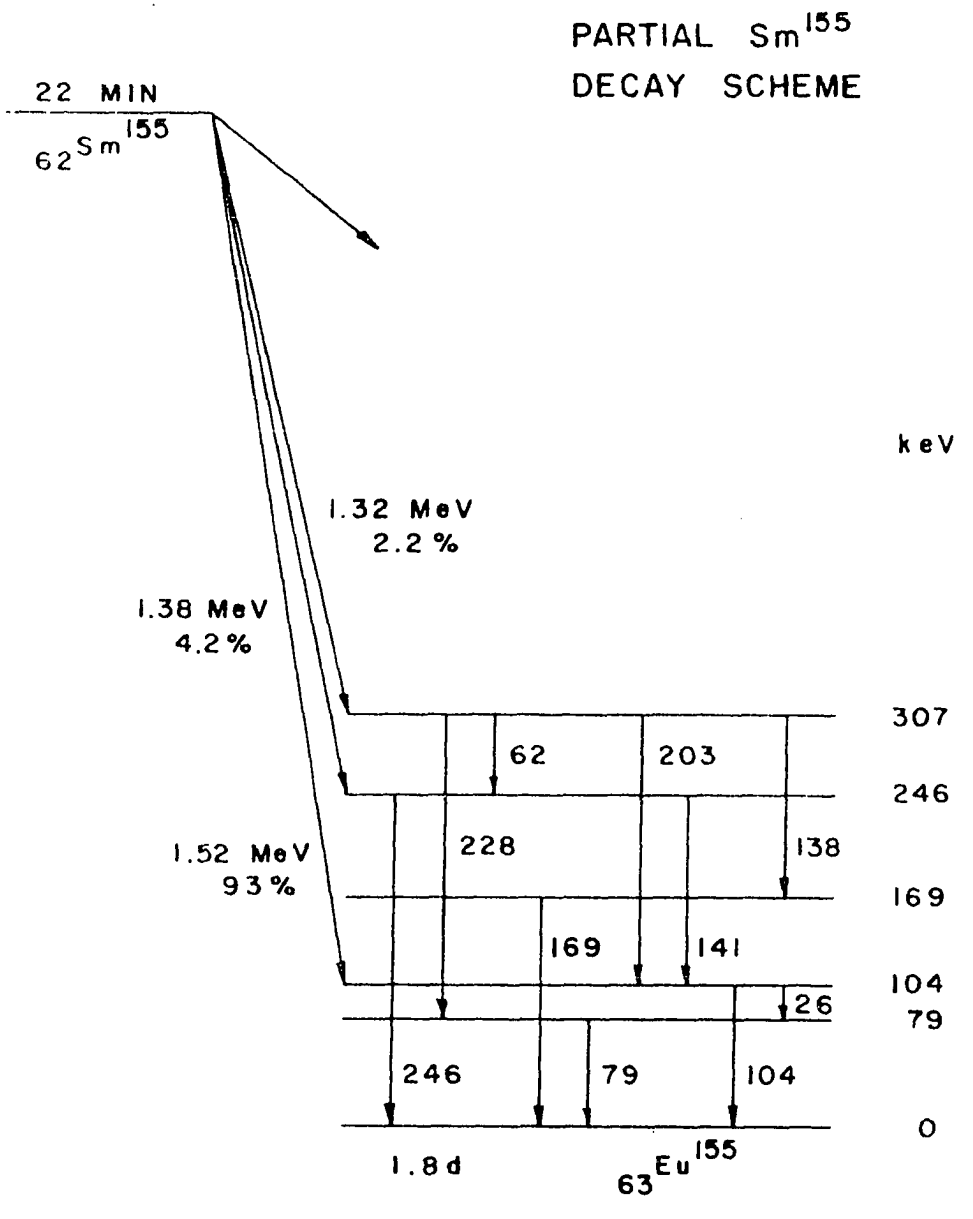

Fig. 18. Portion of the Sm^{155} decay scheme investigated in the work reported here

Table 4. Relative intensities of gamma rays from Sm^{155}

Gamma-ray energies (keV)	Measured gamma-ray relative intensities			
	Funke (61)	Agin (86)	Nelson (18)	Widemann (88)
25.7	11 ± 5			49 ± 5
61.55	4.5 ± 1.5	6.6 ± 0.6		5.7 ± 0.2
78.65	4.5 ± 1.5	≤0.5		7.0 ± 0.4
104.32	2000 ± 200	2270 ± 40	2000 ± 90	2040 ± 100
141.37	45 ± 5	54 ± 2	56 ± 5	49 ± 5
167.1	1.8 ± 0.3	1.7 ± 0.3		0.9 ± 0.1
168.7				0.7 ± 0.1
228.5	1.2 ± 0.2	1.3 ± 0.1		1.3 ± 0.2
245.8	100	100	100 ± 6	100

Since there is some disagreement concerning the intensities of the 25.7- and 78.65-keV transitions, the silicon photon spectrometer was employed to measure the intensities of the low-energy gamma rays as well as the K x-ray to gamma-ray ratio for the strong 104-keV gamma ray. Figure 19 pictures the Gaussian fits to several of the photon peaks from the decay of Sm^{155} and Table 5 shows the relative gamma-ray intensities obtained with the silicon detector. The present results seriously bring into question the value of Agin *et al.* (86) for the intensity of the 79-keV transition and the value of Widemann and Sebille (88) for the intensity of the 26-keV transition. Widemann and Sebille show that so small an inten-

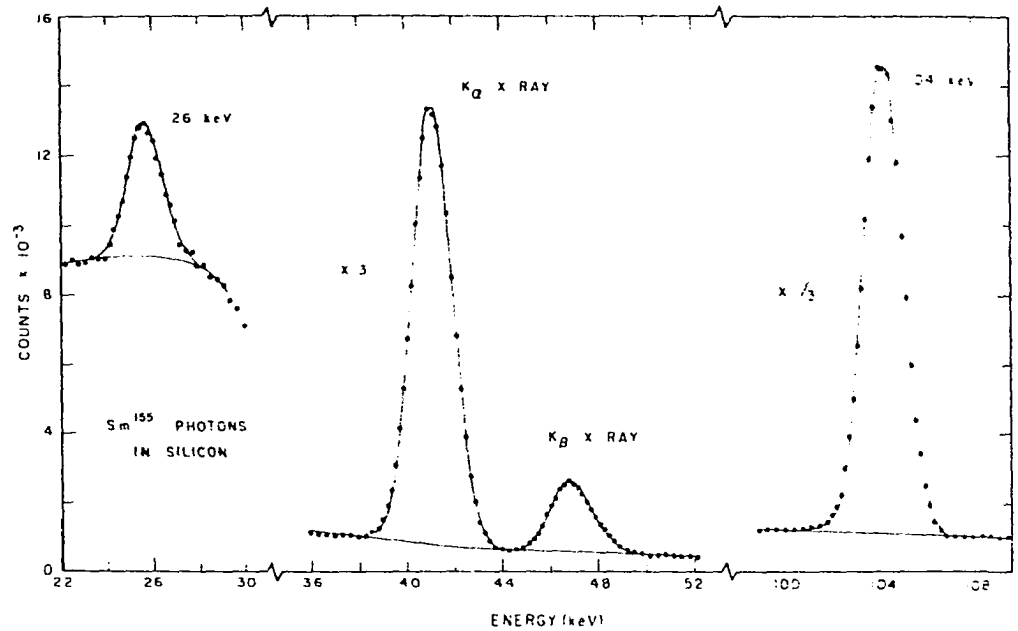

Fig. 19. Portion of silicon spectrum showing some photon peaks from Sm^{155} fit with Gaussian shapes plus quadratic backgrounds

Table 5. Relative intensities of Sm^{155} photons measured with Si(Li)

Transition energy (keV)	Photon relative intensities Present results
25.7	13.5 ± 2
K_α x-ray	370 ± 17
K_β x-ray	89 ± 5
61.55	5.8 ± 0.8
78.65	6.8 ± 1.0
104.32	2000 ± 100

sity for the 79-keV gamma ray produces unreasonably large internal conversion coefficients since the conversion electron intensities are appreciable. On the other hand, if the present result for the intensity of the 26-keV gamma ray is accurate, the possibility of an energy level exising at approximately 25 keV in Eu^{155} as proposed by Widemann and Sebille is greatly reduced.

From the results listed in Table 5 the total K x-ray to gamma-ray ratio for the 104-keV transition is

$$\frac{I_{K_x}^T}{I_\gamma} = \frac{459 \pm 22}{2000 \pm 100} = 0.230 \pm 0.016.$$

The K-shell internal conversion coefficient for the 104-keV transition is then

$$\alpha_K = \frac{R_K I_{K_x}^T}{\omega_K I_\gamma} = (0.251 \pm 0.018) R_K$$

where $\omega_K = 0.92$ is the K-shell fluorescent yield for Eu and R_K is the fraction of all K-shell internal conversion electrons that accompany the 104-keV transition. When R_K has been determined from the measurement of the internal conversion electron relative intensities, a value for the standard Sm^{155} conversion coefficient can be deduced by the K x-ray to gamma-ray ratio method.

A second value for the ratio of the intensity of the total K x-ray to the 104-keV gamma-ray intensity was found from NaI spectra. Here the ratio

$$\frac{I_{K_x}^T}{I_\gamma} = 0.225 \pm 0.020$$

was measured so that

$$\alpha_K = \frac{R_K I K_x^T}{\omega_K I_\gamma} = (0.245 \pm 0.022) R_K$$

can provide another value for the standard Sm^{155} conversion coefficient that was determined partially by an independent experiment.

The silicon-NaI and silicon-germanium simultaneous singles spectra yielded directly the K-shell internal conversion coefficients for the strong 104-keV transition. The former arrangement gave $\alpha_K = 0.249 \pm 0.027$ and the latter $\alpha_K = 0.253 \pm 0.026$. These values are slightly above the

theoretical E1 conversion coefficient of 0.214 calculated by Hager and Seltzer (3). Thus, the 104-keV transition has almost pure E1 character with perhaps an M2 admixture of about 0.2%. This result is surely reasonable in view of the fact that the transition between the same two Nilsson orbitals in the decay of Sm^{153} to Eu^{153} apparently has E1 character with a small M2 admixture (89).

2. Internal conversion electron relative intensities

Like the gamma-ray spectrum, the Sm^{155} conversion electron spectrum is dominated by lines from the strong 104-keV transition. In addition to the 104K, L, M, N lines, only the 79L, 141K and 246K peaks show up clearly in the singles spectra. The 141K line at 93 keV was barely resolved from the intense 104L lines near 96 keV in the work reported here. The reasonably strong 62L peak was completely overwhelmed by the 104K peak at practically the same energy, and the intensity of the 62L peak had to be determined by a special method described later in this section.

Table 6 lists the relative intensities of those conversion electron lines which stand out clearly above the continuous beta-ray distribution. The measurements include data from approximately forty runs taken with all three of the

Table 6. Sm^{155} relative electron intensities from singles runs

Conversion line	Measured relative intensity
79L	74 ± 5
104K	4200 ± 180
L_I	415 ± 20
L_{II}	95 ± 25
L_{III}	120 ± 13
L_{total}	630 ± 30
M	133 ± 10
N	40 ± 9
141K	41 ± 3
246K	100 ± 5

silicon detectors. Over a hundred coincidence runs were made; practically all of them used the same silicon detector gated by beta rays that lost over 600 keV in the plastic crystal. Normally coincidence spectra from about ten sources irradiated on the same day were added together to obtain sufficient statistics for analysis. Figure 20 shows a major portion of one such Sm^{155} summed spectrum. Fourteen additional conversion electron lines from the decay of Sm^{155} appeared clearly in the coincidence spectra. These included weak lines at higher energies such as the L and M peaks from

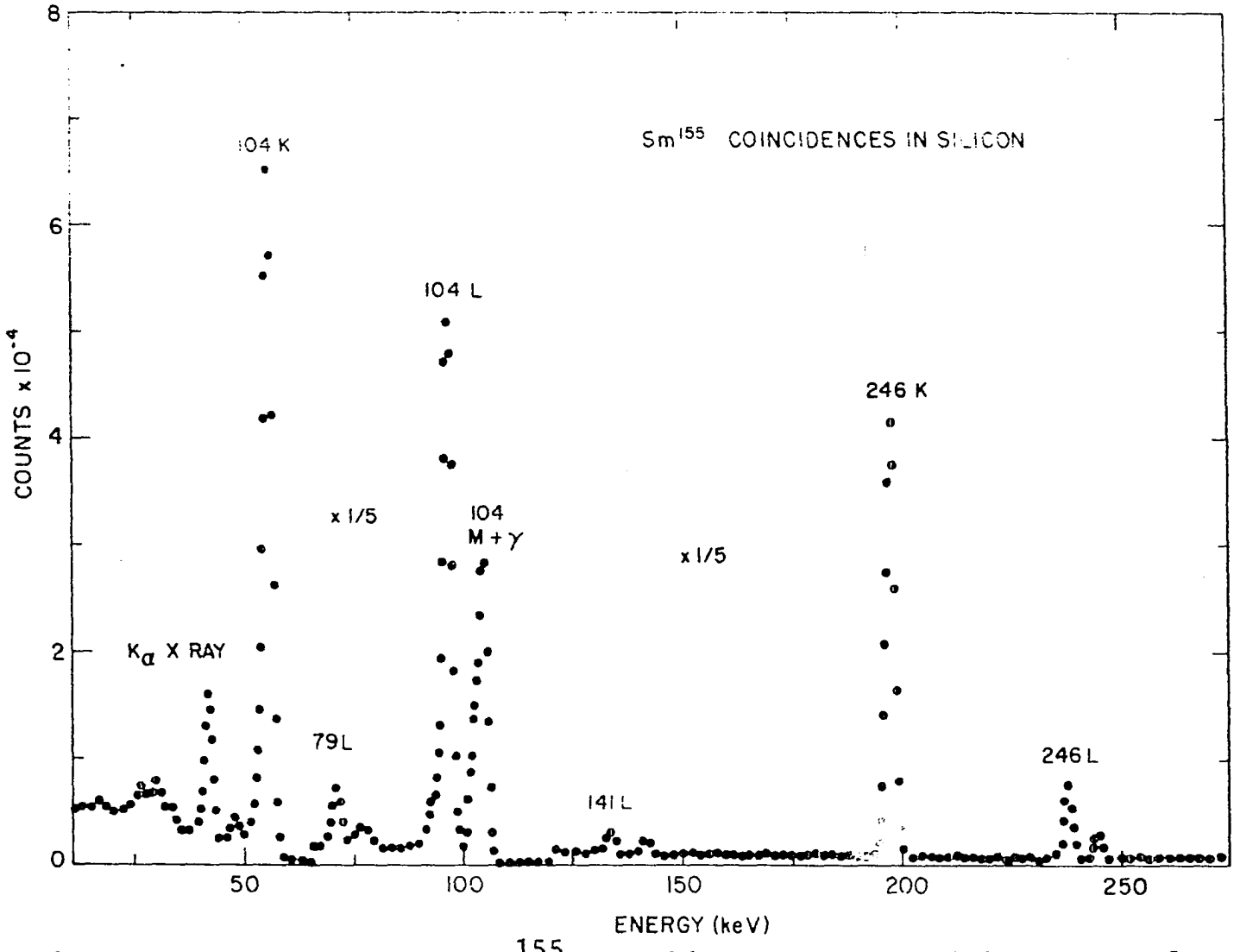

Fig. 20. A major portion of a Sm^{155} coincidence spectra. Coincidences from nine separate sources were combined to give the statistics shown here

the 141- and 246-keV transitions, reasonably strong lines at low energies which were masked in the singles spectra by back-scattered beta rays and even the KLL and KLM Auger groups. The computer unfolding routine gave χ^2 values between 1.29 and 1.98. Figure 21 pictures the unfolding of the congested region near 100 keV into component response functions. The composite spectrum is the same as that seen in Figure 20.

Table 7 illustrates the results of unfolding the Sm^{155} coincidence spectra. The second column of the table lists the relative conversion electron intensities measured directly from the coincidence spectra while the intensities in the third column include the corrections for beta-ray branching described in Appendix II. The fact that the discrepancies between the relative intensities in column three of Table 7 and those in Table 6 are not only small but also of the same relative magnitude for the 141K and 246K lines indicates that the angular correlations effects discussed in Appendix III are not of major significance here. The corrected coincidence results were combined with the singles results to yield a final set of conversion electron relative intensities. In the cases of the 141K and 246K lines, the values from the singles data were chosen as most reasonable.

Fig. 21. Results of unfolding the region near the 104L peak in the Sm^{155} spectrum. The individual response functions (solid lines) combine to give the calculated composite spectrum (dashed line) which best fits the data points (x's). The intensities of the L_{II} and N lines are subject to the largest uncertainties

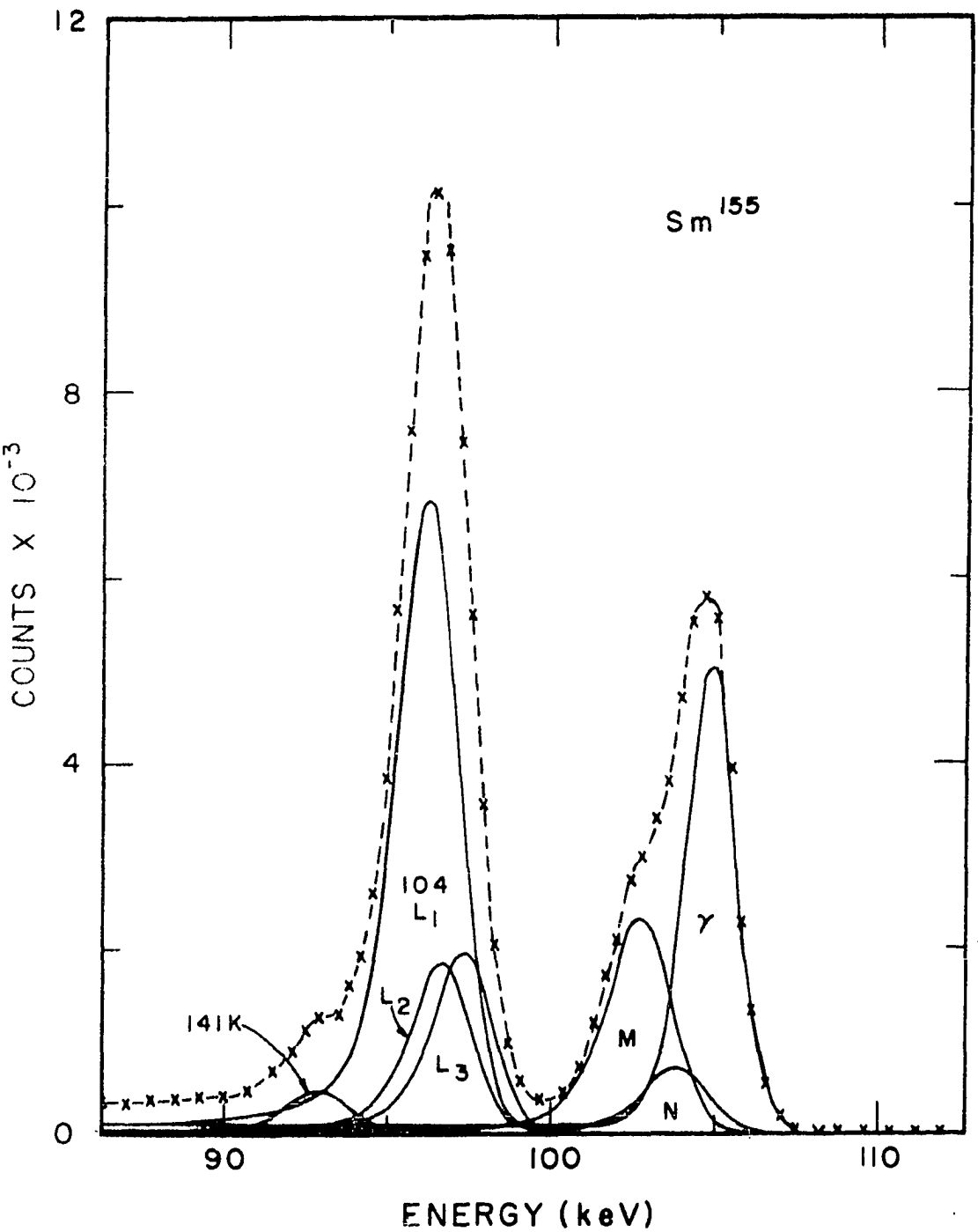
12
8
4
0
COUNTS X 10^{-3}
Sm^{155}
104
L_1
L_2
L_3
141K
M
N
γ
90
100
110
ENERGY (keV)

Table 7. Sm^{155} relative conversion electron intensities from coincidence runs

Conversion line	Measured electron relative intensity	
	Direct from coincidence data	After correction for beta-ray branching
KLL	230 ± 20	234 ± 21
KLM	93.4 ± 10	95.2 ± 11
26L	185 ± 35	185 ± 36
M	60 ± 12	60 ± 13
62K	173 ± 45	226 ± 59
M	14.2 ± 3.0	18.5 ± 3.9
79K	185 ± 22	185 ± 24
L	73.9 ± 5.0	73.9 ± 6.0
M	17.1 ± 2.4	17.1 ± 2.7
104K	4200 ± 175	4200 ± 200
L_I	414 ± 17	414 ± 20
L_{II}	94 ± 34	94 ± 34
L_{III}	118 ± 12	118 ± 13
L_{total}	626 ± 40	626 ± 45
M	126 ± 13	126 ± 15
N	42 ± 12	42 ± 13
141K	31.0 + 2.7	38.8 ± 3.5
L	5.1 ± 0.6	6.3 ± 0.8
M	0.9 ± 0.2	1.1 ± 0.3
167K	2.2 ± 0.6	2.7 ± 0.8
229K	1.1 ± 0.4	1.4 ± 0.5
246K	74.9 ± 4.0	93.8 ± 7.0
L	11.2 ± 0.8	14.0 ± 1.0
M	2.9 ± 0.5	3.6 ± 0.6

A special coincidence experiment was performed to obtain the intensity of the 62L peak from the decay of Sm^{155}. The strong competing 104K line was eliminated by requiring that events counted by the silicon detector be in coincidence with gamma rays of 104 keV. The experimental apparatus consisted of the silicon-NaI spectrometer and the coincidence electronics described separately in the previous chapter. Figure 22 compares a silicon singles spectrum with the Sm^{155} spectrum taken in coincidence with the 104-keV gamma ray. The beta-ray distribution is enhanced in the coincidence spectrum because a majority of the 104-keV gamma rays are in coincidence with only a beta ray. The weak 62L and 141K lines stand out clearly in the coincidence spectrum so their relative intensity can be determined. Here again, the coincidence intensities must be considered while possible angular correlation effects are ignored. Thus

$$\frac{I_{62L}}{I_{141K}} = \frac{M_{62L}}{M_{141K}} \frac{\varepsilon_{141K}}{\varepsilon_{62L}} \frac{\langle 141,104\rangle}{\langle 62,104\rangle}$$

where M_{62L}/M_{141K} is the relative peak intensity seen by the silicon detector operating in the coincidence mode, $\varepsilon_{62L}/\varepsilon_{141K}$ is the relative peak efficiency of the silicon detector and $\langle 62,104\rangle/\langle 141,104\rangle$ is the relative coincidence intensity with

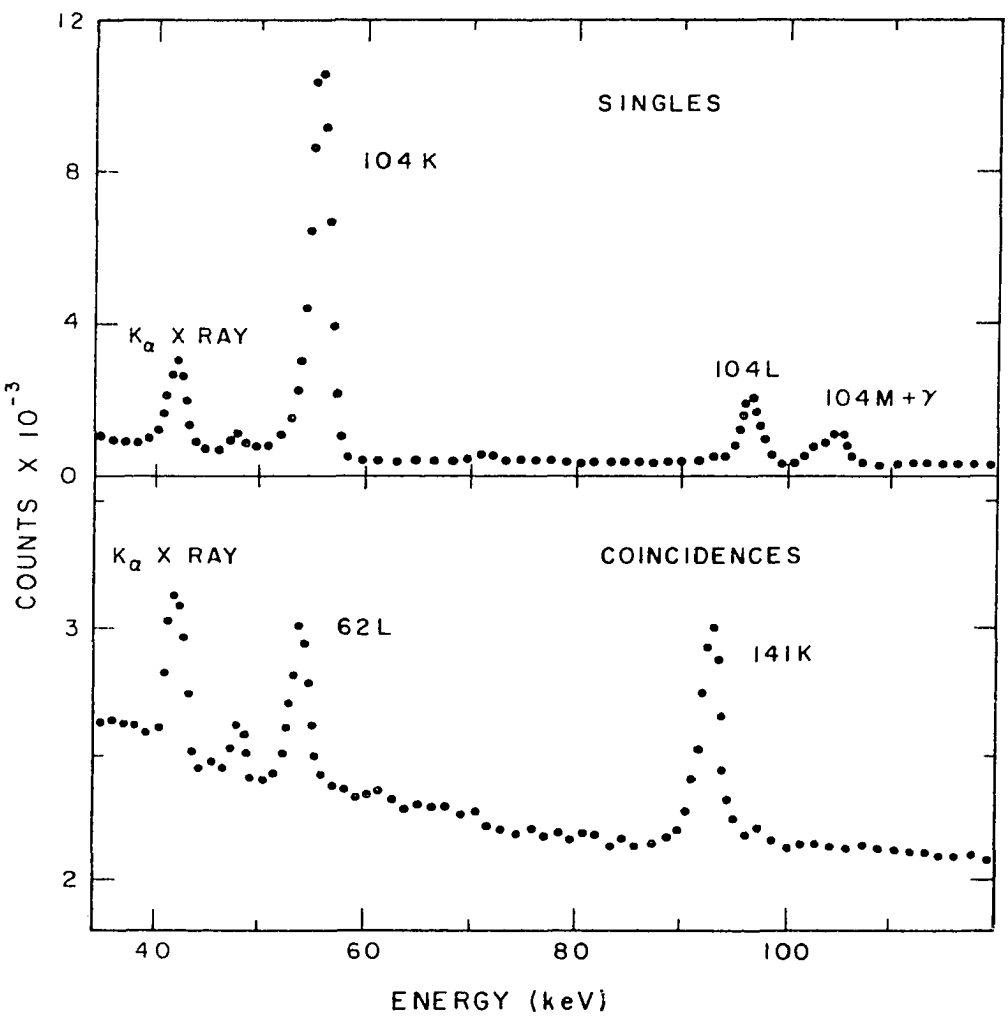

Fig. 22. A Sm^{155} silicon singles spectrum (top) and a Sm^{155} silicon spectrum in coincidence with 104-keV gamma rays

respect to the 104-keV transition. These concepts are similar to those used in Appendix II, but peak areas and efficiencies must be used because of the presence of the beta-ray background. The experiment measured

$$\frac{M_{62L}}{M_{141K}} \frac{\epsilon_{141K}}{\epsilon_{62L}} = 0.63 \pm 0.06 \text{ while } \frac{\langle 141, 104\rangle}{\langle 62, 104\rangle} = 3.45 \pm 0.15$$

from the same self-consistent approach to the decay scheme described in Appendix II. Thus $I_{62L} = (2.2 \pm 0.2) I_{141K}$.

Table 8 lists the Sm^{155} conversion electron intensities found in the present work and compares them with the results of Kracik *et al.* (90) and Widemann and Sebille (88). The early work of Kracik and co-workers was performed with an intermediate image beta-ray spectrometer. Because of the 22-minute Sm^{155} half-life, they were able to measure only a small part of the total electron spectrum with one source. Hence, many sources were required to accumulate a spectrum, and the various source strengths had to be normalized one to the other. The recent measurements of Widemann and Sebille were made with a high-resolution magnetic spectrograph. It should be noticed that it is not fair to conclude from Table 8 that the present results are superior to those of Widemann and Sebille. These French workers were able to resolve the L lines of the 61.55- and 78.65-keV transitions as well as the

Table 8. Relative intensities of electrons from the decay of Sm^{155} to Eu^{155}

Conversion line	Measured electron relative intensities		
	Kracik(90)	Widemann(88)	Present results
KLL			235 ± 20
KLM			95 ± 10
26L			185 ± 35
M			60 ± 12
62K			230 ± 60
L			90 ± 10
M		12 ± 2	18 ± 4
79K			185 ± 22
L	70	97 ± 8	74 ± 5
M		27 ± 3	17 ± 2
104K	4100	4100 ± 380	4100 ± 200
L_I		450 ± 50	415 ± 20
L_{II}		90 ± 9	95 ± 25
L_{III}		110 ± 9	120 ± 13
L_{total}	630	650 ± 60	630 ± 30
M	100	140 ± 9	130 ± 10
N		40 ± 4	40 ± 9
141K		48 ± 5	41 ± 3
L		4 ± 1.5[a]	6.8 ± 0.9
M		2 ± 1[b]	1.2 ± 0.3
167K		4 ± 1.5	2.9 ± 0.8
229K		≤2	1.4 ± 0.5
246K	63	150 ± 9	100 ± 5
L	12	25 ± 3[a]	15 ± 1
M		8 ± 2	3.8 ± 0.6

[a] L_I contribution only.

[b] M_I contribution only.

104-keV transition and to obtain precise energies for even some weak transitions. However, the difficulty of extracting intensity data from photographic plates counterbalances the magnetic spectrograph's advantage of improved resolution and hinders the obtaining of excellent electron intensities with the magnetic spectrograph. In the Sm^{155} case, the magnetic spectrograph results produce better L-subshell ratios which can provide a sensitive measure of the transition multipolarities while the present work yields reasonably precise relative intensities of low-energy electron lines.

The major discrepancy among the values in Table 8 concerns the intensity of the 246K conversion electron peak. It is difficult to imagine any cogent reason for the fifty percent difference between the latest two measurements since both claim to have fairly small uncertainty assignments. An examination of possible sources of systematic error forces the conclusion that the true intensity is almost surely close to the value reported here.

The electron intensities in Table 8 provide an estimate of the fraction of all K-shell internal conversion electrons that accompany the 104-keV transitions. Thus $R_K = 0.88 \pm 0.06$ can be combined with the measurements of the K x-ray to

gamma-ray ratio described above to give values of the K-shell internal conversion coefficient for the 104-keV transition. The silicon detector experiment yields

$$\alpha_K = (0.251 \pm 0.018)R_K = 0.221 \pm 0.022$$

while the photon data taken with a NaI crystal gives

$$\alpha_K = (0.245 \pm 0.022)R_K = 0.216 \pm 0.024.$$

An average of the four different experimental determinations of this internal conversion coefficient finally defines $\alpha_K = 0.235 \pm 0.020$ as the standard coefficient to which all the others in the Sm^{155} decay are normalized. The electron relative intensities found in this investigation along with the experimental gamma-ray intensities due mostly to other workers then yielded the measured internal conversion coefficients shown in Table 9. The table also lists the theoretical values of Hager and Seltzer (3) plus the transition multipolarities deduced from the present results.

3. Discussion

The strong 104-keV transition was found to have practically pure E1 character. Widemann and Sebille (88) claim the transition is pure E1. While the present results are not inconsistent with this view, they do favor the possibility that the character of the transition includes a small M2 admixture.

Table 9. Internal conversion coefficients and multipolarities for transitions in the decay of Sm^{155}

Transition energy (keV)	Conversion line	Internal conversion coefficients			Transition multipolarity
		Experimental	Theoretical		
			E1		
26	L	1.60 ± 0.41	1.65		E1
	M	0.52 ± 0.13	0.36		
			M1	E2	
62	K	4.7 ± 1.4	6.46	3.38	M1 +
	L	1.85 ± 0.33	0.93	9.42	(10 ± 4)% E2
	M	0.37 ± 0.09	0.20	2.19	
			M1	E2	
79	K	3.14 ± 0.49	3.14	2.14	M1 +
	L	1.25 ± 0.15	0.45	2.90	(33 ± 6)% E2
	M	0.29 ± 0.04	0.096	0.67	
			E1	M2	
104	K	0.235 ± 0.020	0.214	11.9	
	L_I	0.024 ± 0.003	0.0220	2.25	
	L_{II}	0.0054 ± 0.0015	0.0043	0.27	E1 +
	L_{III}	0.0069 ± 0.0010	0.0054	0.41	0.2% M2
	L_{total}	0.036 ± 0.004	0.0317	2.93	
	M	0.0075 ± 0.0009	0.0069	0.67	
	N	0.0023 ± 0.0006			

Table 9. (Continued)

Transition energy (keV)	Conversion line	Internal conversion coefficients			Transition multipolarity
		Experimental	Theoretical		
			E1		
141	K	0.096 ± 0.018	0.095		E1
	L	0.016 ± 0.003	0.014		
	M	0.0028 ± 0.0008	0.0029		
			M1	E2	
167	K	0.38 ± 0.08	0.37	0.26	M1, E2
			M1	E2	
229	K	0.13 ± 0.05	0.16	0.10	M1, E2
			M1	E2	
246	K	0.117 ± 0.014	0.129	0.081	M1
	L	0.0176 ± 0.0019	0.0182	0.0217	
	M	0.0044 ± 0.0008	0.0039	0.0052	

It is, of course, conceivable that any deviation from the theoretical E1 conversion coefficients is due to small penetration effects. The truly mixed transitions of 61.55 and 78.65 keV have multipolarities of (90 ± 4)% M1 + (10 ± 4)% E2 and (67 ± 6)% M1 + (33 ± 6)% E2, respectively. These agree with the (9 ± 3)% E2 and (29 ± 1)% E2 admixtures found by Widemann and Sebille (88). The results reported here are consistent with the assignments of pure multipolarities to the other two strong transitions at 141.4 and 245.8 keV. Still, it is possible for the predominantly M1 character of the 246-keV transition to possess an E2 admixture of up to 30%. The 167K internal conversion coefficient quoted may be a bit large because of interference from the weaker K-shell electron line of the nearby 169-keV transition. Conversely, the fact that the 169K conversion line did not appear in the electron spectra leads one to expect an E1 character for the 169-keV transition. The large uncertainties in the 26L and 26M coefficients allow some M2 admixture in the 26-keV transition while any combination of M1 and E2 multipolarities is possible for the 229-keV transition.

The angular momentum of the Eu^{155} ground state has been assumed to be 5/2 in analogy with the Eu^{151} and Eu^{153} ground

states (91). Gamma-gamma directional correlation work (92) suggested a spin sequence of 5/2, 5/2, 3/2 for the ground state and the excited states at 104 and 245 keV. The early conversion coefficient results of Schmid and Burson (85) and Kracik et al. (90) indicate that the 104-, 141- and 246-keV transitions are predominantly E1, E1 and M1 in character. This meager experimental evidence along with the Nilsson (93) theoretical energy level diagram was sufficient to indicate tentatively that Eu^{155} is a deformed nucleus with a deformation parameter of 0.2-0.3. The ground state was interpreted as the Nilsson $5/2+[413]$ level while the states at 104 and 246 keV were assigned Nilsson quantum numbers of $5/2-[532]$ and $3/2+[411]$, respectively. The levels at 79, 169 and 307 keV then fitted in as rotational states (94) built upon the respective intrinsic Nilsson levels. The present results and those of Widemann and Sebille (88) lend experimental support to this picture which had previously been based extensively on the theoretical arguments. The more precise measurements show that the 104-, 141- and 246-keV transitions definitely possess E1, E1 and M1 multipolarities. The rotational transitions of 61.55 and 78.65 keV have mostly M1 character with reasonably strong E2 admixtures, as expected. The weaker inter-

connecting transitions all were found to have the correct multipolarities if we permit the 167-keV transition a pure E2 character as required by the spin assignments. Thus, the spin and parities of the low-lying nuclear states in Eu^{155} all have now been measured experimentally.

The gamma-ray intensity rules of Alaga (95) can test the characteristics of the rotational bands. These rules predict theoretical intensity ratios for transitions of the same multipolarity which proceed from a single initial level to different members of the rotational band in question. The 26- and 104-keV transitions were both found to have predominately E1 character. In addition, each connects the 5/2 - [532] state to a level in the ground state rotational band. The gamma-ray intensity ratio was measured to be $I_{26\gamma}/I_{104\gamma} = 0.0068 \pm 0.0010$ while the theoretical ratio is 0.0063. This good agreement is consistent with the assignment of E1 multipolarities to both transitions and the conjecture that the ground state rotational band is unmixed. However, the rotational moment of inertia and the transition intensities from the 307-keV level (16,88) indicate that the ground state rotational band is coriolis coupled to a higher-lying band.

B. Nd^{151}

A decay scheme for 12-minute Nd^{151} was first proposed by Schmid and Burson (96) on the basis of studies with a magnetic spectrograph and scintillation spectrometers. It has been revised and extended by the gamma-ray work of Fossan et al. (97), Dzhelepov et al. (98) and finally Zganjar and Helmer (62) to include over a hundred transitions among a large number of nuclear levels in the Pm^{151} daughter. Figure 23 pictures the portion of the Nd^{151} decay scheme which is relevant to the work reported here. A number of the transitions need to be considered here only because of the effect on the beta-ray branching correction. Table 10 lists three sets of experimental relative intensities for the gamma rays of interest in the present work. The extensive gamma-ray analysis contributed by Zganjar and Helmer still remains incomplete. Many of the results used here were generously provided by Dr. Edward Zganjar previous to publication.

1. Photon intensities and standard conversion coefficient

The intensities of the low-energy gamma rays and the K x-rays were measured with the silicon photon spectrometer. The purpose of this experiment was basically twofold. First, to search for the 32-keV gamma ray corresponding to a transi-

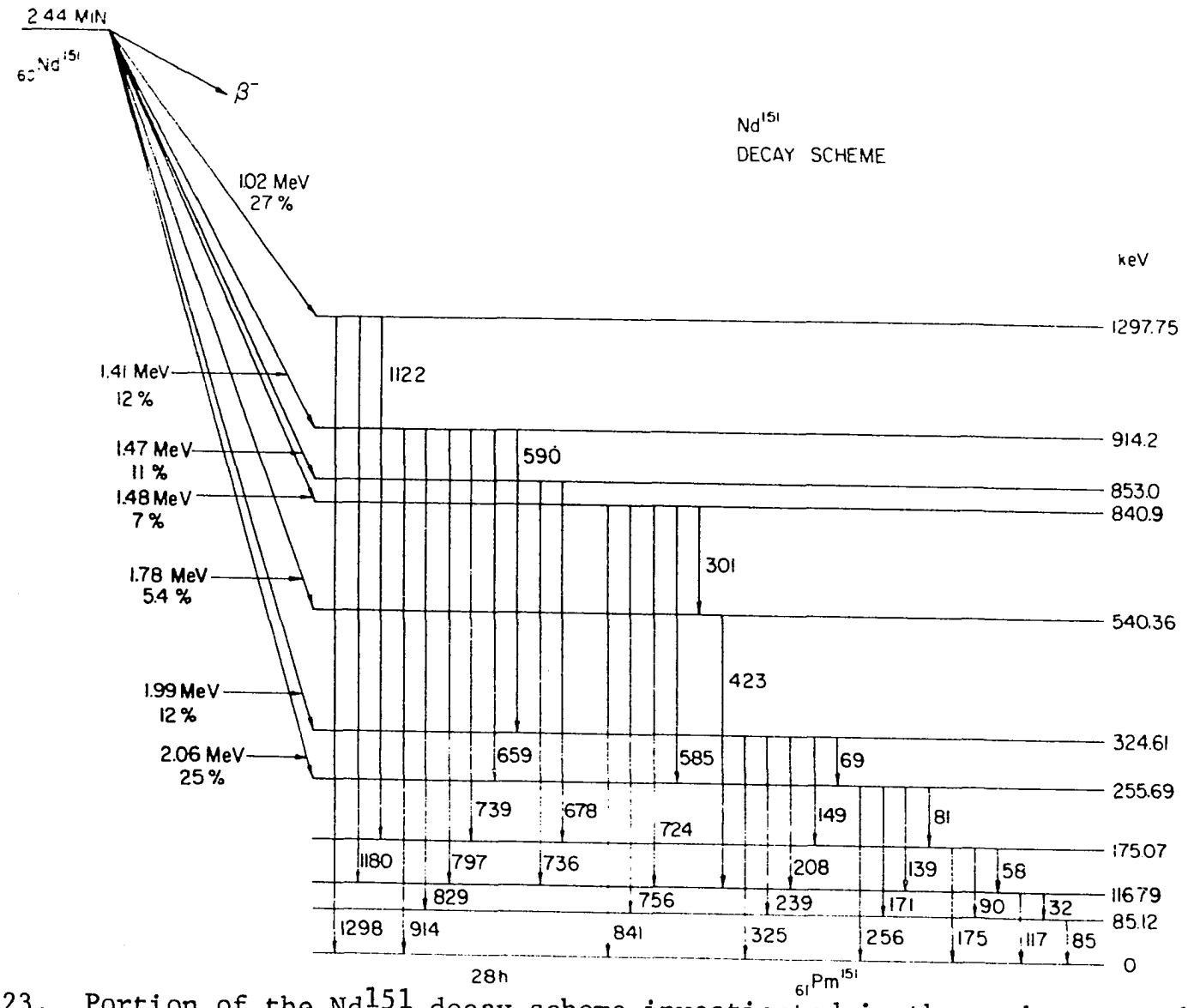

Fig. 23. Portion of the Nd^{151} decay scheme investigated in the work reported here

Table 10. Relative intensities of gamma rays from Nd^{151}

Gamma-ray energies (keV)	Measured gamma-ray relative intensities		
	Fossan (97)	Dzhelepov (98)	Zganjar (62)
58.32			2.4
68.99			8.7
81.85			3.3
85.12	55		14
89.96			11
102.9			3.3
116.79	450		222
138.88	73		43
149.5			2.2
170.75	120		23
175.07			42
183.1			2.5
197.2	5		1.8
199.7			2.0
208.1			2.1
238.7			5.7
239.5			
255.69	130		76
300.6	14		11
324.61	5		3.3
402.3	14		9.6
423.57	55		36
585.2			7.4
589.6			2.0
658.6			4.5
678.0	9		15
724.2			19
736.2	55	50±8	40
739.2			12
755.6			7.4
797.5	36	30±6	32
829.1			1.5
841.1	2		6.5
914.2		6±2	8.2
1122.6	27	33±5	30
1180.9	100	100	100
1297.8			1.3

tion between the first and second excited states in Pm^{151}. No previous study looked at such low energies. Second, to determine the K x-ray to gamma-ray ratio for the strong 117-keV gamma ray. This ratio provides a poor value for the K-shell internal conversion coefficient of the 117-keV transition because the internal conversion of numerous other transitions contribute strongly to the intensity of the K x-rays. However, the K x-ray to gamma-ray ratio can serve to check the overall balance between measured photon and conversion electron intensities. Figure 24 shows the Gaussian fits to several of the photon peaks from the decay of Nd^{151}, and Table 11 lists the relative intensities found with the silicon detector.

Table 11. Relative intensities found with silicon detector

Transition energy (keV)	Photon relative intensities Present results
28	0.4 ± 0.2
32	1.2 ± 0.2
K_α x-ray	94 ± 5
K_β x-ray	23 ± 2
58	3 ± 1
69	8 ± 2
85	13 ± 4
90	12 ± 4
117	200 ± 9
139	41 ± 8

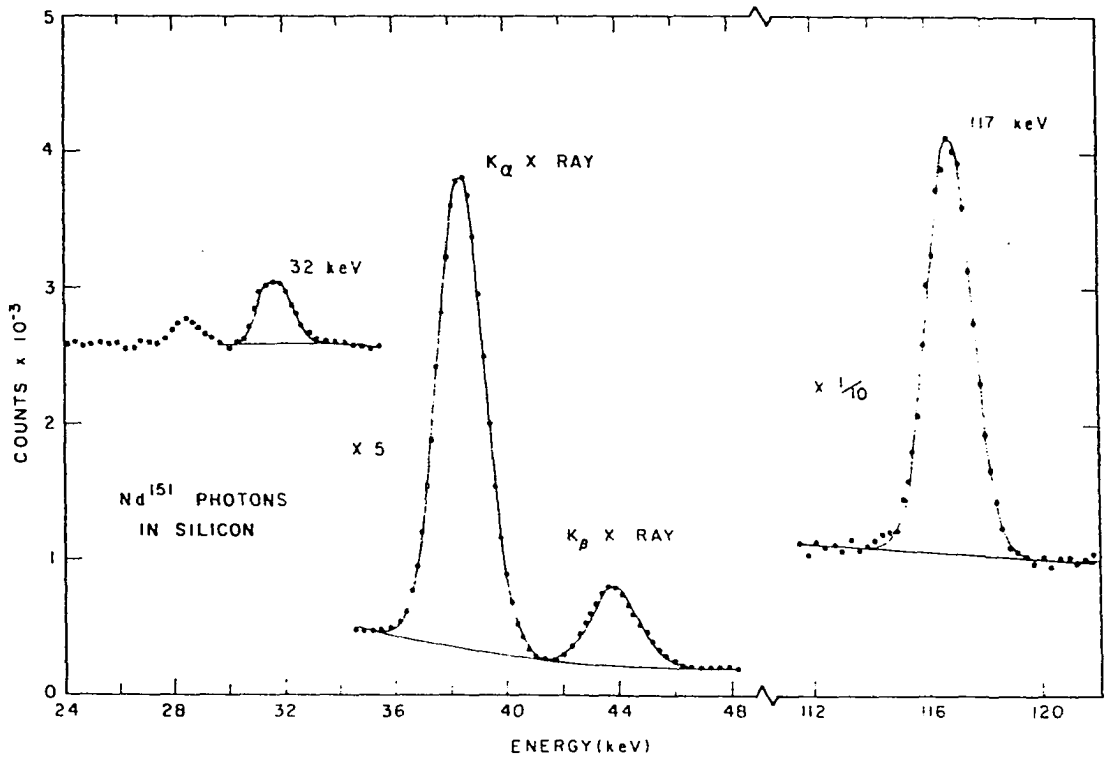

Fig. 24. Portion of silicon spectrum showing some photon peaks from Nd^{151} fit with Gaussian shapes plus quadratic backgrounds

The 32-keV gamma ray definitely exists. The possibility that the peak at this energy could be due to the x-ray via some escape mechanism was investigated by comparing corresponding regions of Nd^{151} and Nd^{149} photon spectra. The gamma-ray branching ratio for de-excitation of the 117-keV level in Pm^{151} is $I_{32\gamma}/I_{117\gamma} = 0.0060 \pm 0.0011$ while the branching ratio for the corresponding 104-keV level in Eu^{155} is $I_{26\gamma}/I_{104\gamma} = 0.0068 \pm 0.0010$. The fact that these ratios are even similar makes the measured intensity of the 32-keV gamma ray appear to be quite reasonable. The spectrum shown in Figure 24 contains the strongest evidence found for the existence of a gamma ray with energy 28.5 ± 1 keV. Such a transition does not fit into the preliminary decay scheme in Figure 23, and it may not even belong to the Nd^{151} decay since the line was too weak for its half-life to be measured accurately. Still, the present work provides some reason to think a weak 28-keV transition may be associated with the decay of Nd^{151} to Pm^{151}.

From the results in Table 11, the total K x-ray to gamma-ray ratio for the 117-keV transition is

$$\frac{I_{K_x}^T}{I_\gamma} = \frac{117 \pm 7}{200 \pm 9} = 0.585 \pm 0.044.$$

The K-shell internal conversion coefficient for the 117-keV transition is formally then

$$\alpha_K = \frac{R_K I_{K_x}^T}{\omega_K I_\gamma} = (0.64 \pm 0.05) R_K$$

where $\omega_K = 0.91$ is the K-shell fluorescent yield for Pm and R_K is the fraction of all K-shell internal conversion electrons that accompany the 117-keV transition. Because of the complexity of the Nd^{151} decay scheme, R_K is not close to unity, and its value can not be measured very accurately. Nonetheless, the K x-ray to gamma-ray ratio method provides an independent check on the normalization of conversion electron to photon intensities.

The primary normalization of electron to gamma-ray relative intensities was obtained by measuring the K-shell internal conversion coefficient of the 117-keV transition directly with the two simultaneous singles spectrometers. The silicon-NaI spectra gave a value $\alpha_K = 0.164 \pm 0.017$ while the silicon-germanium arrangement yielded $\alpha_K = 0.170 \pm 0.016$. The uncertainty in the NaI experiment is a bit larger because of the difficulty in separating the 117-keV gamma ray from weaker neighboring gamma rays. The weighted average value, $\alpha_K = 0.167 \pm 0.015$ is slightly above the theoretical E1 internal

conversion coefficient of 0.149 calculated by Hager and Seltzer (3). Thus, another similarity between the Nd^{151} and Sm^{155} decays now appears.

2. Internal conversion electron relative intensities

The Nd^{151} conversion electron spectrum is not dominated by a small number of very strong lines. Instead, many peaks of comparable intensity are spread over the lower 150 keV of the electron spectrum. The line density is so great in the low-energy region that, in several cases, different lines occur at almost the same energy. For example, the 85K and K_α x-ray overlap; the 90K and the K_β x-ray are not resolved; the 32L is hidden by the 69K peak; the 90L line is mixed up with the 85M and 85N. When possible, the computer was used to unfold such compound peaks. In other cases, the composite lines had to be fit as a single response function by the computer routine. Semi-theoretical arguments were then employed to divide the response function intensity among the component lines in some reasonable manner. Naturally, such a procedure leads to large uncertainties.

Twenty-three electron peaks were strong enough to be seen clearly above the beta-ray distribution present in the singles spectra. The electron relative intensities based on

an analysis of about thirty singles runs are listed in Table 12. Over eighty irradiations were made in accumulating Nd^{151} coincidence spectra. Figure 25 illustrates the major portion of a coincidence spectrum obtained by summing the data from eight irradiations, while Figure 26 shows how the low-energy region of the same spectrum was unfolded into component response functions. Notice that the Nd^{149} contaminant was included as one of the response functions. The beta-ray conversion electron coincidence arrangement permitted the intensities of more than twenty additional conversion lines to be obtained. Table 13 shows the results found from the unfolding of the coincidence spectra. The χ^2 goodness-of-fit parameter varied from 1.16 to 1.77 for the unfolded spectra. The second column of the table lists the relative electron intensities measured directly from the coincidence spectra while the intensities in the third column include the corrections for beta-ray branching described in Appendix II.

Several comments should be made about the data shown. Notice that the coincidence arrangement reduces the intensities of the conversion electron lines from the low-lying 117-keV transition, for example, more than the intensities of conversion lines from some higher-lying transitions. The

Table 12. Nd^{151} relative electron intensities from singles runs

Conversion line	Measured relative intensity
KLL (32M)	130 ± 10
KLM (81K)	73 ± 7
58L	36 ± 4
69K (32L)	520 ± 40
L	76 ± 4
M	24 ± 4
85K	370 ± 40
L	160 ± 10
M	40 ± 4
90K	43 ± 4
102K (58M)	67 ± 5
117K	520 ± 25
L	76 ± 4
M	18 ± 4
139K	56 ± 4
L	8.5 ± 1.6
171K	85 ± 5
L	15 ± 1.2
175K	28 ± 2
239K	4.5 ± 0.7
255K	100 ± 5
L	16 ± 1
423K	12 ± 0.8

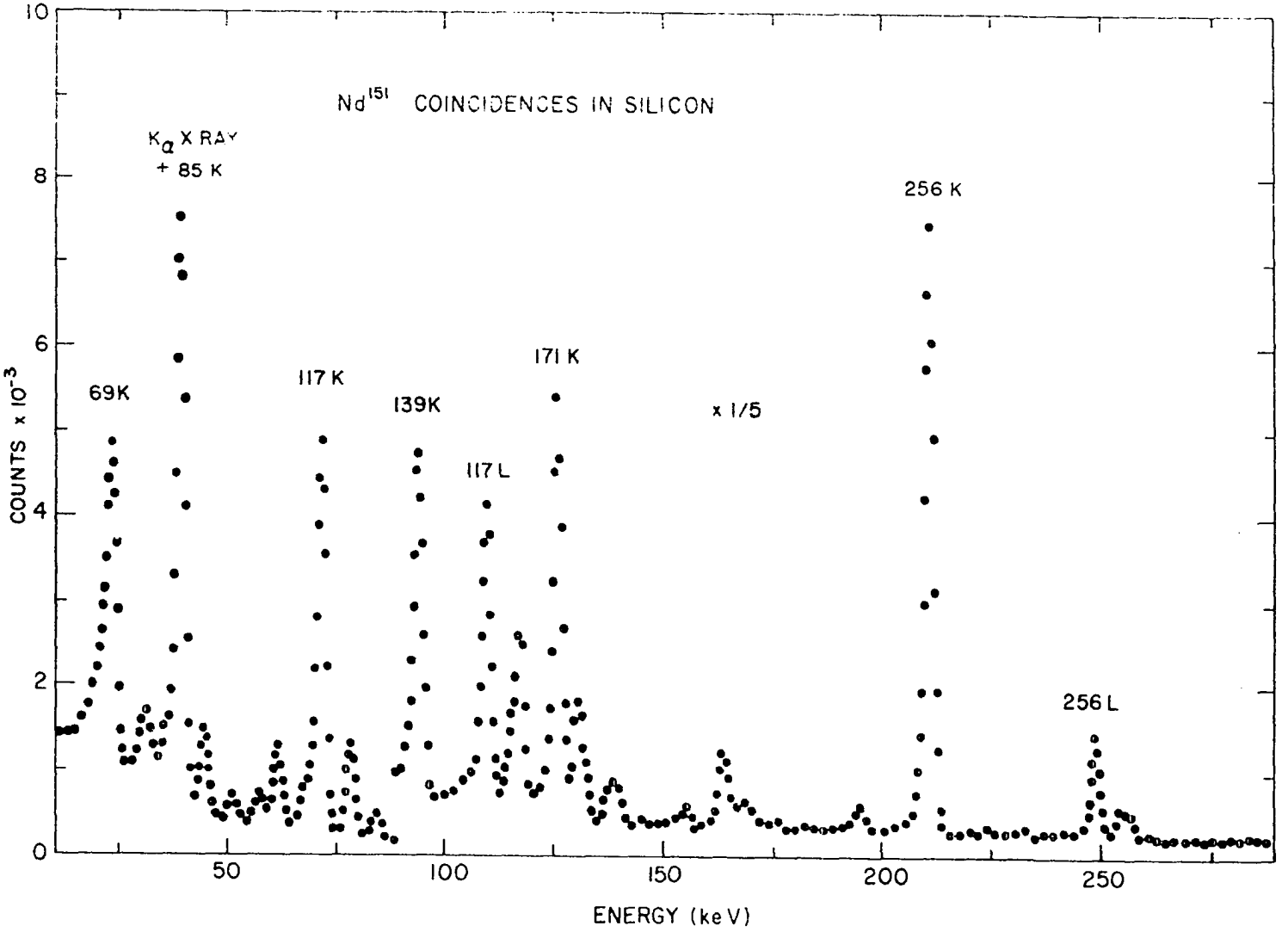

Fig. 25. A major portion of a Nd^{151} coincidence electron spectrum

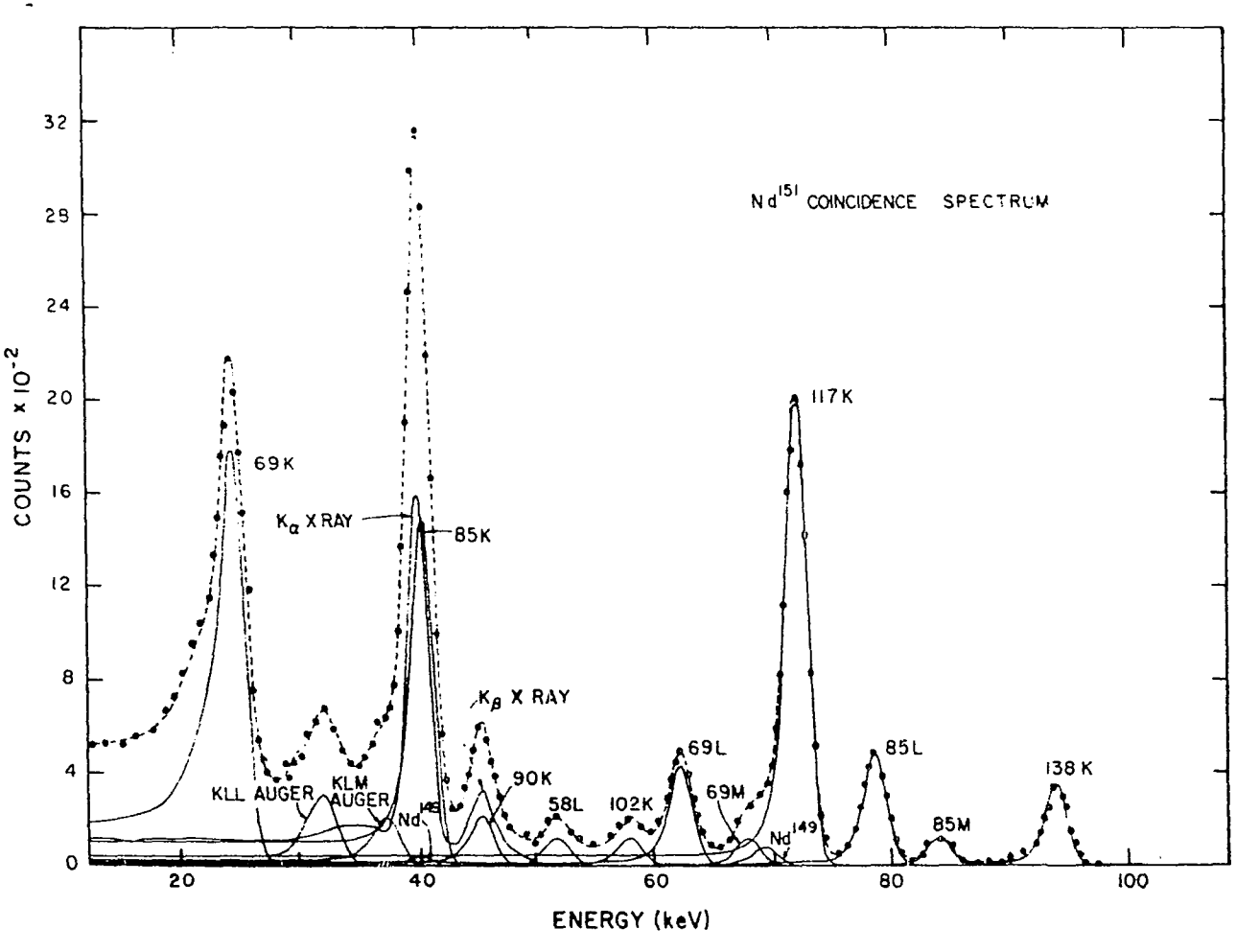

Fig. 26. Results of unfolding the low energy portion of a Nd^{151} spectrum. The individual response functions (solid lines) combine to give the calculated composite spectrum (dashed line) which best fits the data points (dots)

Table 13. Nd^{151} relative electron intensities obtained from coincidence runs

Conversion line	Measured electron relative intensity	
	Direct from coincidence data	After correction for beta-ray branching
KLL (32M)	78 ± 8	124 ± 13
KLM (81K)	51 ± 6	68 ± 10
58L	19 ± 2	38 ± 5
69K (32L)	480 ± 40	530 ± 45
L	71 ± 4	75 ± 5
M	22 ± 3	23 ± 3
85K	190 ± 30	249 ± 45
L	78 ± 5	104 ± 12
M (90L)	20 ± 2	26 ± 3
N	6.5 ± 1	8.5 ± 2
90K	21 ± 3	42 ± 7
102K (58M)	21 ± 2	---[a]
117K	320 ± 15	510 ± 60
$L_{I,II}$	38 ± 3	61 ± 10
L_{III}	10 ± 1.8	16 ± 3
L_{total}	48 ± 3	77 ± 11
M	11 ± 2	17 ± 3
N	4 ± 2	6 ± 3
139K	55 ± 3	55 ± 5
L	8.5 ± 1.3	8.5 ± 1.7
M (183K)	6 ± 1.5	---[a]
149K	2.2 ± 0.8	2.4 ± 0.9

[a]Transition is not placed in the decay scheme and the correction for beta-ray branching can not be made.

Table 13. (Continued)

Conversion line	Measured electron relative intensity: Direct from coincidence data	Measured electron relative intensity: After correction for beta-ray branching
171K	69 ± 4	69 ± 7
L	13 ± 1.2	13 ± 1.5
M	3.7 ± 0.8	3.7 ± 1
175K	14 ± 1	28 ± 3
L	2.8 ± 0.8	5.5 ± 1.7
M (183L)	1.5 ± 0.7	3 ± 1.5
197K	1.4 ± 0.7	---[a]
200K	3.6 ± 0.8	---[a]
239K	3.8 ± 0.7	---[a]
L	1.0 ± 0.3	
255K	100 ± 5	100 ± 7
L	16 ± 1.2	16 ± 1.5
M	3.8 ± 0.8	3.8 ± 1.0
264K	0.9 ± 0.4	---[a]
301K	1.0 ± 0.4	1.9 ± 0.8
325K	1.5 ± 0.6	1.7 ± 0.7
402K	4 ± 0.9	---[a]
L	1.0 ± 0.3	
423K	10 ± 1.3	13 ± 1.8
L	2.5 ± 0.9	3.3 ± 1.3
585K	1.3 ± 0.4	2.5 ± 0.9
736K	1.0 ± 0.3	2.0 ± 0.7
797K	0.4 ± 0.2	0.9 ± 0.5
914K	0.2 ± 0.1	0.4 ± 0.2

phenomenon occurs because the 117-keV level is fed by several strong high-energy transitions which are in coincidence with only low-energy beta rays.

The major discrepancies between the corrected coincidence results and those obtained from the singles spectra involve the intensities of the conversion lines from the 85- and 171-keV transitions. The magnitude of the discrepancies suggests that the 171-keV transition should be placed higher up in the decay scheme. In the present scheme, the 85-keV transition is joined directly to the E_o = 2.06 MeV beta-ray branch by the 171-keV transition. Hence, any change in the position of the 171-keV transition would tend to increase the beta-ray branching corrections for both the 85- and 171-keV transitions. Actually, any major juggling of the decay scheme would require re-examination of all the beta-ray branching corrections.

Because of uncertainties in the decay scheme and in the branching corrections, the data from the singles spectra were used as much as possible. For example, the correction needed to produce agreement between the electron intensities of the 69-keV transition obtained from the uncorrected coincidence spectra and those found from the singles spectra was also

applied to the 149- and 325-keV transitions that de-excite the same level. The coincidence spectra should provide accurate shell and subshell ratios. Table 14 lists the Nd^{151} conversion electron intensities obtained in the present work and compares them with the early results found by Schmid and Burson (96) with a magnetic spectrograph.

The data in Table 14 can be used to find R_K, the fraction of the total K-shell conversion electrons that accompany the 117-keV transition. Thus,

$$R_K = \frac{520 \pm 25}{2000 \pm 250} = 0.26 \pm 0.03$$

where a large part of the uncertainty arises in estimating the intensity of the 58K conversion line. Then, the K x-ray to gamma-ray ratio provides an independent estimate of the K-shell internal conversion coefficient for the 117-keV transition. In this manner, $\alpha_K = (0.64 \pm 0.05)R_K = 0.17 \pm 0.02$, in reasonable agreement with the values determined from the two simultaneous singles spectrometers. Normalization to $\alpha_K = 0.167 \pm 0.015$ for the 117-keV transition produces the measured internal conversion coefficients shown in Table 15. The table also includes the theoretical conversion coefficients of Hager and Seltzer (3) plus the transition multipolarities

Table 14. Relative intensities of electrons from the decay of Nd^{151} to Pm^{151}

Conversion line	Measured electron relative intensities	
	Schmid and Burson (96)	Present results
KLL (32M)		130 ± 10
KLM (81K)		73 ± 7
58L		37 ± 5
69K (32L)		520 ± 40
L		76 ± 4
M		24 ± 4
85K	69	370 ± 40
L	86	160 ± 10
M (90L)	10	40 ± 4
N		13 ± 2
90K		43 ± 5
102K (58M)		67 ± 5
117K	520	520 ± 25
$L_{I,II}$		61 ± 5
L_{III}		16 ± 3
L_{total}	66	77 ± 5
M		19 ± 3
N		6 ± 3
139K	50	56 ± 4
L		8.6 ± 1.4
M (183K)	9	6 ± 1.5
149K		2.4 ± 0.9
171K	90	85 ± 5
L		16 ± 1.3
M		4.6 ± 1

Table 14. (Continued)

Conversion line	Measured electron relative intensities	
	Schmid and Burson (96)	Present results
175K		28 ± 2
L		5.5 ± 1.7
M(183L)		3 ± 1.4
239K		4.5 ± 0.7
L		1.2 ± 0.4
256K	150	100 ± 5
L	35	16 ± 1
M		3.8 ± 0.8
301K		1.9 ± 0.8
325K		1.7 ± 0.7
402K		4.0 ± 0.9[a]
L		1.0 ± 0.3[a]
423K		12 ± 0.8
L		3 ± 1
585K		2.5 ± 0.9
736K		2.0 ± 0.7
797K		0.9 ± 0.5
914K		0.4 ± 0.2

[a]No provision made for unknown coincidence correction.

Table 15. Internal conversion coefficients and multipolarities for transitions in the decay of Nd^{151}

Transition energy (keV)	Conversion line	Internal conversion coefficients			Transition multipolarity
		Experimental	Theoretical		
			E1		
32	L	2.7 ± 2.2	0.86		E1
	M	0.18[a]	0.18		
			M1	E2	M1 +
58	L	1.10 ± 0.18	0.886	10.1	(2.5±2)% E2
	M	0.2[a]	0.188	2.3	
			M1	E2	
69	K	3.84[a]	3.87	3.07	M1 +
	L	0.62 ± 0.07	0.545	4.59	(4±2)% E2
	M	0.19 ± 0.04	0.116	1.05	
			E1		
81	K	0.4 ± 0.2	0.39		E1
			M1	E2	
85	K	1.9 ± 0.3	2.12	1.87	
	L	0.82 ± 0.10	0.30	1.74	M1 +
	M	0.20 ± 0.03	0.063	0.40	(40±10)% E2
	N	0.04 ± 0.02			

[a]Theoretical value used as basis for dividing up multiplet.

Table 15. (Continued)

Transition energy (keV)	Conversion line	Internal conversion coefficients			Transition multipolarity
		Experimental	Theoretical		
			E1		
90	K	0.28 ± 0.04	0.302		E1
	L	0.044[a]	0.044		
			M1	E2	
102	K	1.3 ± 0.2	1.23	1.12	M1, E2
			E1	M2	
117	K	0.167 ± 0.015	0.149	6.75	
	$L_{I,II}$	0.0196 ± 0.0023	0.0181	1.32	E1 +
	L_{III}	0.0051 ± 0.0011	0.00324	0.19	(0.3±0.2)% M2
	L_{total}	0.0247 ± 0.0027	0.0213	1.51	
	M	0.0061 ± 0.0010	0.00447	0.34	
	N	0.0019 ± 0.0009			
			E1		
139	K	0.093 ± 0.010	0.0932		
	L	0.0143 ± 0.0027	0.0131		E1
	M	0.0028[a]	0.0028		
			E1		
149	K	0.08 ± 0.03	0.076		E1
			M1	E2	M1
171	K	0.264 ± 0.032	0.295	0.243	M1 +
	L	0.049 ± 0.006	0.0412	0.0817	(35±20)% E2
	M	0.014 ± 0.003	0.0087	0.0184	

Table 15. (Continued)

Transition energy (keV)	Conversion line	Internal conversion coefficients			Transition multipolarity
		Experimental	Theoretical		
			E1		
175	K	0.048 ± 0.006	0.0498		E1
	L	0.0094 ± 0.0031	0.0069		
	M	0.00145[a]	0.00145		
			M1	E2	
183	K	0.13 ± 0.04	0.275	0.225	M1, E2
	L	0.06 ± 0.04	0.038	0.074	
			E1	E2	
239	K	0.056 (±0.010)	0.022	0.085	--[b]
	L	0.015 (±0.006)	0.003	0.021	
			M1	E2	
256	K	0.094 ± 0.010	0.0983	0.0694	
	L	0.015 ± 0.002	0.0135	0.0166	M1
	M	0.0035 ± 0.0008	0.0029	0.0036	
			E1		
301	K	0.014 ± 0.006	0.012		E1
			M1	E2	
325	K	0.037 ± 0.015	0.052	0.034	M1, E2

[b]Transition not placed in decay scheme. Experimental conversion coefficient subject to large uncertainty.

Table 15. (Continued)

Transition energy (keV)	Conversion line	Internal conversion coefficients				Transition multipolarity
		Experimental	Theoretical			
			M1	E2		
402	K	0.030(±0.009)	0.030	0.018		--[b]
	L	0.008(±0.003)	0.004	0.003		
			M1	E2		
423	K	0.024 ± 0.003	0.0262	0.0159		M1
	L	0.006 ± 0.002	0.0036	0.0029		
585	K	0.024 ± 0.009	E1: 0.0025 M1: 0.012 E2: 0.0068 M2: 0.034			
			E1	E2	M1	
736	K	0.0036 ± 0.0013	0.0015	0.0039	0.0066	E2
			E1	E2	M1	
797	K	0.002 ± 0.001	0.0014	0.0034	0.0057	E1
			M1	E2		
914	K	0.0035 ± 0.0018	0.004	0.0024		M1, E2

deduced from the present results. In cases where two conversion electron lines overlapped, theoretical conversion coefficients were used in assigning portions of the electron peak intensity to different members of the multiplet. For example, α_L for the 58-keV transition determined the multipolarity of the transition to be M1 + (2.5±2)% E2. The corresponding theoretical α_M = 0.2 then fixed the 58M conversion electron intensity so the remainder of the 102K-58M electron doublet could be assigned to the 102K component. A more complicated chain related the 69K line to the 32L, 32M, KLL Auger, KLM Auger and finally the 81K lines. It is not surprising that large errors enter conversion coefficients measured in this way.

3. Discussion

The angular momentum of the Pm^{151} ground state was measured to be 5/2 by an atomic beam experiment (99), while the magnetic and quadrupole moments (100) are μ = 1.8 nm and Q = 1.9 barns. The large quadrupole moment suggests that Pm^{151} is deformed with a deformation parameter δ of 0.2-0.3. This is an interesting speculation in itself since Pm^{149} is not deformed and Fossan et al. (97) treat Pm^{151} as a spherical nucleus having only eight neutrons outside the closed shell at N = 82. The Nilsson scheme allows either

the 5/2 + [413] or the 5/2 - [532] states but favors the 5/2 + [413] assignment on the basis of the measured magnetic moment of the ground state. The analysis of the Pm^{151} decay to Sm^{155} by Chery (101) indicates that the Pm^{151} parent has positive parity. Thus, the Pm^{151} ground state is a 5/2+ level which may be interpreted as the 5/2 + [413] Nilsson state if the nucleus proves to have a rotational character.

The predominant E1 multipolarities of the 117- and 139-keV transitions indicate negative parity for the 117-keV level and positive parity for the 256-keV level. The long half-life (97) of the 256-keV level argues that it cannot be a rotational state even though it de-excites by an M1 transition to the ground state. However, the M1 plus E2 character of the 85-, 58- and 69-keV transitions is strong evidence that the 85-, 175- and 325-keV levels are rotational states built upon the ground state plus the single particle excitations at 117 and 256 keV, respectively. The Nilsson scheme provides the possibility of 3/2 + [411], 3/2 - [541] and 5/2 - [532] orbitals at low energies. The 3/2 + [411] state is assigned to the positive parity level at 256 keV while the 5/2 - [532] state is preferred for the level at 117 keV because of the E1 character of the 32-keV transition to the 7/2+ member of the

ground state rotational band. Thus, the low-lying states in Pm^{151} are remarkably similar to the Eu^{155} states discussed earlier. Figure 27 shows the magnitude of the similarity. Only minor differences can be noted. The level and transition energies differ to a small extent, and the Eu^{155} scheme contains no counterpart to the 90-keV transition in Pm^{151}. This omission is due to the fact that the 7/2- member of the 5/2 - [532] band is fed only very weakly in the Sm^{155} decay.

Notice that the 81-keV transition in Pm^{151} can not de-excite the 256-keV level because it was found to have E1 multipolarity. This transition must belong another place in the Nd^{151} decay scheme. Similarly , the Sm^{155} decay scheme has no transition joining the 3/2 + [411] level to the 7/2- member of the 5/2 - [532] band. There is also some question about the placement of the 171-keV transition in Pm^{151}. It was previously noted that the present placement of this transition obscured an understanding of effects of beta-ray branching. The scheme in Figure 27 requires that the 171-keV transition have pure E2 character. While the internal conversion coefficient results do not prohibit its having a pure E2 multipolarity, they do favor something like a fifty-fifty mixture of M1 and E2 characters for the 171-keV transition.

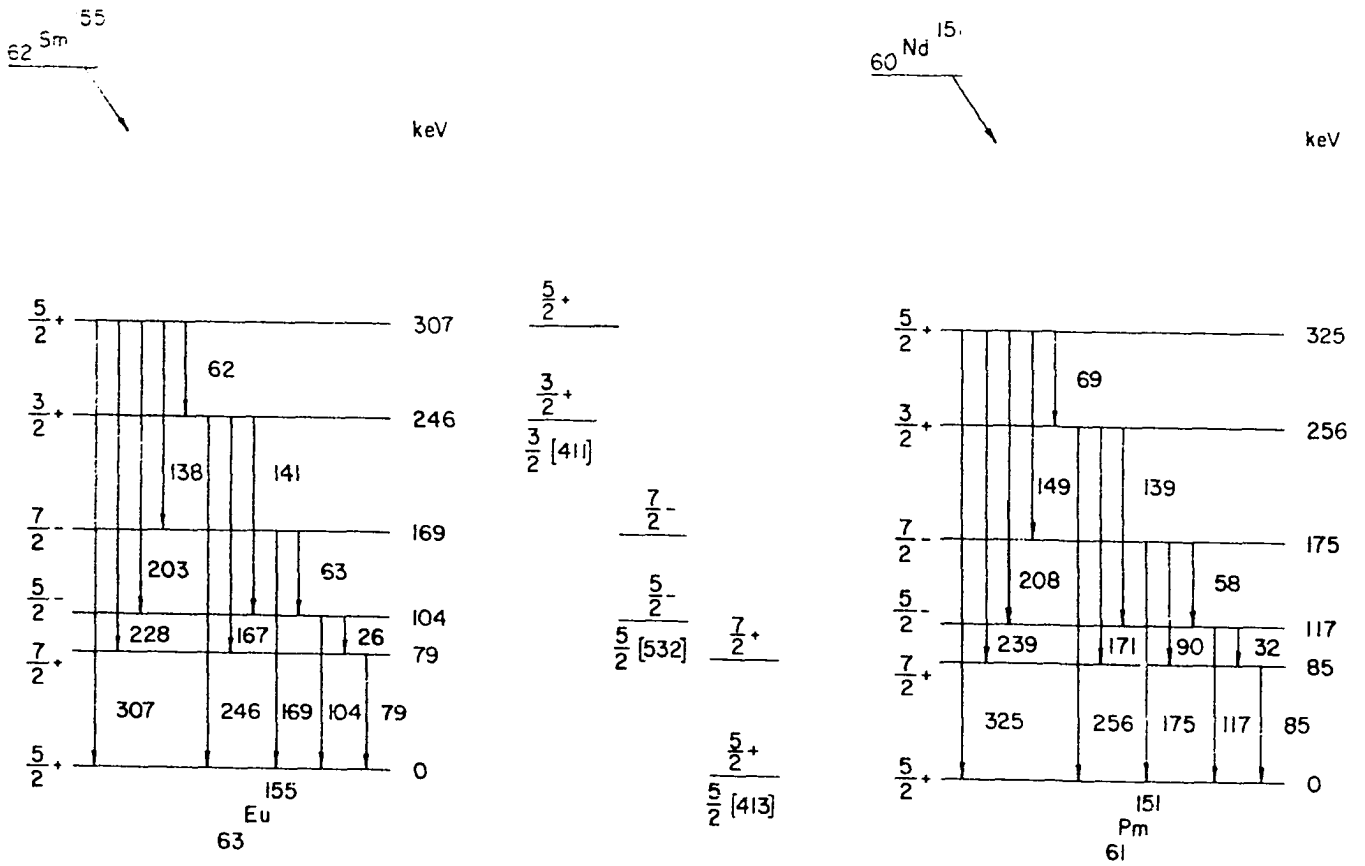

Fig. 27. Comparison of low-lying nuclear levels in Eu^{155} and Pm^{151}

In addition, the 171-keV transition in Pm^{151} is about thirty times stronger on a relative scale than the corresponding 167-keV transition in Eu^{155}. Thus, either the 171-keV transition glaringly disrupts the similarity of the low-lying levels in Eu^{155} and Pm^{151} or the transition fits in elsewhere in the Nd^{151} decay scheme. It is, of course, conceivable that this transition is a doublet whose weaker component connects the 3/2 + [411] state to the 7/2+ member of the Pm^{151} ground state band.

Table 16 compares the mixing ratios of the intraband rotational transitions for the low-lying bands in Pm^{151} and Eu^{155}. The similarity between these two nuclei is retained in that the E2 admixture is large in the 3/2 + [411] band and small in the 5/2 + [413] band for both. The rotational moments of inertia for these two bands are smaller for Pm^{151} than for Eu^{155}, whereas the opposite is true for the 5/2 - [532] band. Whether the mixing ratios for the lowest rotational transition in this band behave anomalously is not known because of the lack of information on the 5/2 - [532] band in Eu^{155}. Table 16 includes the results of Suter *et al.* (102) for the Eu^{153} nucleus where the 5/2 + [413], 5/2 - [532] and 3/2 + [411] bands also occur at low energies.

Table 16. E2 admixtures to M1 rotational transitions in Pm^{151}, Eu^{153} and Eu^{155}

Band	Pm^{151}		Eu^{153}		Eu^{155}	
	Transition energy (keV)	Mixing ratio δ^2	Transition energy (keV)	Mixing ratio $\delta^2(102)$	Transition energy (keV)	Mixing ratio $\delta^2(88)$
5/2+[413]	85	0.67±0.33	83	0.56±0.20	79	0.41±0.02
5/2-[532]	58	0.03±0.02	54		63	
3/2+[411]	69	0.04±0.02	70	0.016±0.002	62	0.10±0.03

Eu^{153} is composed of the same nucleons as Pm^{151} with the addition of two protons while Eu^{155} contains two more neutrons than Eu^{153}. The known properties of the three low-lying bands in Pm^{151} and Eu^{153} are nearly identical.

The gamma-ray intensity rules of Alaga (95) can be applied to the 5/2 + [413] ground state rotational band in Pm^{151}. Table 17 lists the intensity ratios for the E1 transitions to the 7/2+ and 5/2+ members of this band from both the 7/2- and 5/2- members of the 5/2 - [532] band.

Table 17. Measured and theoretical gamma-ray intensity ratios for transitions to 5/2 + [413] band in Pm^{151}

Energy of parent level (keV)	Gamma-ray intensities involved	Intensity ratio	
		Experimental	Theoretical (95)
117	$I_{32\gamma}/I_{117\gamma}$	0.0060±0.0011	0.0080
175	$I_{90\gamma}/I_{175\gamma}$	0.26	0.25

The near agreement of the measured gamma-ray intensity ratios with those predicted by the simple theory tends to suggest that the ground state rotational band is relatively unmixed. However, a similar conclusion based on gamma-ray intensities in the Sm^{155} decay is disputed by other evidence.

The discussion thus far has highlighted the similarities between the Sm^{155} and Nd^{151} decays. The truth is that the decay of the Nd^{151} is much the more complicated. The difference in the characters of the Nd^{151} and Sm^{155} parents causes more levels in the Pm^{151} daughter to be fed. The Sm^{155} ground state is represented by the 3/2 - [521] Nilsson orbital (103) while Nealy and Sheline (104) claim the 5/2 - [523] orbital for the Nd^{151} ground state on the basis of their deuteron-proton scattering data. This 5/2- spin assignment conflicts with the portion of the Pm^{151} level scheme developed in the present work. The Nd^{151} beta decay proceeds to the 5/2+ and 3/2+ members of the 3/2 + [411] band and not to the 5/2 - [532] state as it would by allowed decay if the Nd^{151} ground state had spin 5/2-. The Nd^{150} (d,p) Nd^{151} reaction employed by Nealy and Sheline strongly favors excitation of negative parity levels in Nd^{151}. Thus, their results may be interpreted as showing only that the 5/2 - [523] state is the lowest-lying negative parity level in Nd^{151}. It is possible that the Nd^{151} ground state is a lower-lying positive parity level. This possibility is consistent with the fact that the Q value to the 5/2 - [523] level is less than the predicted ground state Q value (105).

On the basis of the present work, the most likely Nd^{151} ground state is the Nilsson 3/2 + [651] level - the same orbital that describes the Sm^{153} ground state (61).

Little can be stated definitely about the properties of the more excited Pm^{151} levels until the level scheme is better established through completion of gamma-ray studies. The level at 1298 keV is fed by a strong beta-ray branch with log ft less than five. This beta-ray transition is surely allowed so the 1298-keV level apparently has positive parity. The conversion coefficients of the 797- and 914-keV transitions seem to indicate that the level at 914 keV likewise has positive parity. Similarly, the conversion coefficients for the 423- and 301-keV transitions point toward a negative parity level at 540 keV and a positive parity level at 841 keV. The multipolarity data on the 736-keV transition is not convincing enough to support more than a guess at even the parity of the level at 853 keV.

A number of moderate-intensity transitions such as those of 102, 183, 238.7 and 402 keV have not been placed in the tentative Pm^{151} level scheme discussed here. In addition, the original placements of the 81- and 171-keV transitions have been questioned. The present investigation has con-

firmed many of the conjectures made by Dzhelepov et al. (98) concerning the properties of the low-lying Pm^{151} levels. However, there are at present too many uncertainties in the gross outline of the Nd^{151} decay scheme to permit a detailed analysis of all levels. Hopefully, the internal conversion electron results reported here will be more useful when the gamma-ray investigations of Zganjar and Helmer (62) are completed.

C. Summary Remarks

This work has described the use of a lithium-drifted silicon detector to measure the relative intensities of conversion electrons from the decays of Sm^{155} and Nd^{151}. The method employed here includes two unique features. The coincidence arrangement reduced the competitive effects of the continuous beta-ray distribution, and the development of monoenergetic response functions made it possible to unfold entire conversion electron spectra. Reasonable L subshell ratios were obtained for the very strongest transitions even though the L-shell peak showed no clear structure. Several ways to improve the present method come readily to mind. Improved detector resolution could help to separate further the individual conversion electron peaks from each

other and from the beta-ray background. The face-to-face arrangement of the silicon and plastic crystal tended to maximize both the angular correlation effects and the scattering of electrons between the detectors. Both effects could be reduced by fixing the angle between the two crystals at about 126^{o} where the P_2 directional correlation term vanishes. The principal advantage of the experimental apparatus described here remains its simplicity. The present results appear comparable to many obtained with complex magnetic beta-ray spectrometers.

IV. BIBLIOGRAPHY

1. Rose, M. E. Internal Conversion Coefficients. New York, N.Y., Interscience Publishers, Inc. 1958.

2. Sliv, L. A. and I. M. Band. Tables of internal conversion coefficients. In Siegbahn, K., ed. Alpha-, Beta- and Gamma-Ray Spectroscopy. Pp. 1639-1672. Amsterdam, Netherlands, North-Holland Publishing Co. 1965.

3. Hager, R. S. and E. C. Seltzer. Nuclear Data A4: 1. 1968.

4. Blatt, J. M. and V. F. Weisskopf. Theoretical Nuclear Physics. New York, N.Y., John Wiley and Sons. 1952.

5. Rose, M. E., G. H. Goertzel, B. I. Spinrad, J. Haar and P. Strong. Phys. Rev. 83: 79. 1951.

6. Rose, M. E. Tables of internal conversion coefficients. In Siegbahn, K., ed. Beta- and Gamma-Ray Spectroscopy. P. 905. Amsterdam, Netherlands, North-Holland Publishing Co. 1955.

7. Rose, M. E. Theory of internal conversion. In Siegbahn, K., ed. Alpha-, Beta- and Gamma-Ray Spectroscopy. P. 887. Amsterdam, Netherlands, North- olland Publishing Co. 1965.

8. Kohn, W. and L. J. Sham. Phys. Rev. 140A: 1133. 1965.

9. Slater, J. C. Phys. Rev. 81: 385. 1951.

10. Church, E. L. and J. Weneser. Phys. Rev. 104: 1382. 1956.

11. Emery, G. T. and M. Perlman. Phys. Rev. 151: 984. 1966.

12. Pettersson, B. G., L. Holmberg, and T. R. Gerholm. Nuclear Physics 65: 454. 1965.

13. van Nooijen, B. Experimental methods for the determination of internal conversion coefficients. In Hamilton, J. H., ed. Internal Conversion Processes. P. 35.

New York, N.Y., Academic Press. 1966.

14. Subba Rao, B. N. Nuclear Instr. and Methods 45: 22. 1966.

15. Parsignault, D. The beta spectrum of Au^{198}, and the conversion coefficients of the 412-keV line in Hg^{198}. In Hamilton, J. H., ed. Internal Conversion Processes. P. 173. New York, N.Y., Academic Press. 1966.

16. Hagedoorn, H. L. and A. H. Wapstra. Nuclear Physics 15: 146. 1960.

17. Fink, R. W., R. C. Jopson, H. Mark and C. D. Swift. Rev. Mod. Phys. 38: 513. 1966.

18. Nelson, G. C. and E. N. Hatch. Measurements of some gamma-ray relative intensities and internal conversion coefficients using a bent-crystal monochromator. U.S. Atomic Energy Commission Report IS-1730 (Iowa State Univ., Ames). 1967.

19. Nelson, G. C. and E. N. Hatch. Measurements of α_K for the 84.3-keV transition in ^{170}Yb and the 80.6-keV transition in ^{166}Er. U.S. Atomic Energy Commission Report IS-1913 (Iowa State Univ., Ames). 1968.

20. Boneau, D. and E. N. Hatch. Nuclear Physics A118: 238. 1968.

21. Hultberg, S. and R. Stockendal. Arkiv Fysik 14: 565. 1959.

22. Hultberg, S. Arkiv Fysik 15: 307. 1959.

23. Hultberg, S. Recent developments in the internal-external conversion (IEC) method. In Hamilton, J. H., ed. Internal Conversion Processes. P. 125. New York, N.Y., Academic Press. 1966.

24. Newbolt, W. B. and J. H. Hamilton. Nuclear Physics 53: 353. 1964.

25. Erman, P. and S. Hultberg. Arkiv Fysik 30: 101. 1965.

26. Erman, P., B. I. Deutch and C. J. Herrlander. Nuclear Physics A92: 241. 1967.

27. Duke, C. L. and W. L. Talbert, Jr. Phys. Rev. 173: 1125. 1968.

28. Schupp, G. and E. N. Hatch. Precise measurement of the K-shell interval conversion coefficient of the 344-keV, E2 transition in Gd^{152}. U.S. Atomic Energy Commission Report IS-590 (Iowa State Univ., Ames). 1962.

29. Lewin, W. H. G., J. Lettinga, B. van Nooijen and A. H. Wapstra. Nuclear Physics 65: 337. 1965.

30. Croft, W. L., B. G. Pettersson and J. H. Hamilton. Nuclear Physics 48: 267. 1963.

31. Pettersson, B. G., J. E. Thun and T. R. Gerholm. Nuclear Physics 24: 243. 1961.

32. Gerholm, T. R. Arkiv Fysik 11: 55. 1956.

33. Helmer, R. G. and L. D. McIsaac. Phys. Rev. 143: 923. 1966.

34. Gopinathan, K. P. and R. M. Singru. Phys. Rev. 150: 485. 1966.

35. Hatch, E. N., G. W. Eakins, G. C. Nelson, and R. E. McAdams. Method for measuring internal conversion coefficients using a bent-crystal gamma-ray monochromator and a magnetic electron spectrometer. In Hamilton, J. H., ed. Internal Conversion Processes. P. 183. New York, N.Y., Academic Press. 1966.

36. Slätis, H. Arkiv Fysik 6: 415. 1953.

37. Slätis, H. Arkiv Fysik 8: 441. 1954.

38. Slätis, H. Nuclear Instr. and Methods 2: 332. 1958.

39. Slätis, H. Arkiv Fysik 22: 517. 1962.

40. Silberstein, L. and A. P. H. Trivelli. Phil. Mag. 44: 956. 1922.

41. Silberstein, L. Phil. Mag. 45: 1062. 1923.

42. Siegbahn, K., C. Nordling, S. -E. Karlsson, S. Hagström and I. Andersson. Nuclear Instr. and Methods 27: 173. 1964.

43. Berkvist, K. -E. Nuclear Instr. and Methods 43: 170. 1966.

44. Siegbahn, K. Beta-ray spectrometer theory and design. Magnetic alpha-ray spectroscopy. High resolution spectroscopy. In Siegbahn, K., ed. Alpha-, Beta- and Gamma-Ray Spectroscopy. P. 79. Amsterdam, Netherlands, North-Holland Publishing Co. 1965.

45. Graetzer, R., G. B. Hagemann, K. A. Hagemann and B. Elbek. Nuclear Physics 76: 1. 1966.

46. Suarez, A. A., T. von Egidy, W. Kaiser, H. F. Manlein and A. Jones. Nuclear Physics A107: 417. 1968.

47. Taylor, J. M. Semi-Conductor Particle Detectors. Washington, D.C., Butterworth Inc. 1963.

48. Dearnaley, G. and D. C. Northrop. Semi-Conductor Counters for Nuclear Radiations. New York, N.Y., John Wiley, Inc. 1963.

49. Dearnaley, G. and D. C. Northrop. Semi-Conductor Counters for Nuclear Radiations. 2nd ed. New York, N.Y., John Wiley, Inc. 1966.

50. Goulding, F. S. Nucl. Instr. and Methods 43: 1. 1966.

51. Hollander, J. M. Nucl. Instr. and Methods 43: 65. 1966.

52. Haverfield, A. J. The measurement of internal conversion coefficients utilizing semiconductor detectors. U.S. Atomic Energy Commission Report UCRL-16969 (Univ. of California, Berkeley). 1966.

53. Bosch, H. E., F. Krmpotic and A. Plastino. Nuclear Physics 56: 689. 1964.

54. Brown, J. E. and E. N. Hatch. Nuclear Instr. and Methods 47: 185. 1967.

55. Shera, E. B., M. P. Bedesen and K. J. Casper. Rev. Sci. Instr. 38: 1110. 1967.

56. Andersen, V. and C. J. Christensen. Nuclear Instr. and Methods 61: 77. 1968.

57. Burson, S. B. Am. Phys. Soc. Bull. Series II, 13: 673. 1968.

58. Bosch, H. E., F. Krmpotic and A. Plastino. Nucl. Phys. 48: 292. 1963.

59. Bosch, H. E., A. J. Haverfield, E. Szichman and S. M. Abecasis. Nucl. Phys. A108: 209. 1968.

60. Englert, T. J. Nuclear spectroscopic studies with a semiconductor detector coincidence system. Unpublished M.S. thesis. Ames, Iowa, Library, Iowa State University of Science and Technology. 1966.

61. Funke, L., H. Graber, K. -H. Kaun, H. Sodan and J. Frana. Nucl. Phys. 88: 641. 1966.

62. Zganjar, E. F. and R. G. Helmer. Am. Phys. Soc. Bull. Series I, 11: 825. 1966.

63. Edwards, W. F. and F. Boehm. Phys. Rev. 121: 1499. 1961.

64. Scharf-Goldhaber, G. and M. McKeown. Phys. Rev. 158: 1105. 1967.

65. Koicki, S. D., A. H. Kukoc, M. P. Radojevic and J. M. Simic. Bull. Inst. Nuclear Science (Belgrade) 12, No. 3: 1. 1962.

66. Bogdanovic, M., M. Mladjenovic and R. Septic. Nucl. Phys. A106: 209. 1967.

67. Nelson, G. C. and E. N. Hatch. Z. Physik 202: 293. 1967.

68. Chu, Y. Y., O. C. Kistner, A. C. Li, S. Monaro and M. L. Perlman. Phys. Rev. 133: B1361. 1964.

69. Chu, Y. Y. and M. L. Perlman. Phys. Rev. 135: B319. 1964.

70. Suter, T., P. Reyes-Suter and W. Scheuer. Nucl. Phys. 47: 251. 1963.

71. Newbolt, W. B. and J. H. Hamilton. Nucl. Phys. 53: 353. 1964.

72. Moragues. J. A., P. Reyes-Suter and T. Suter. Nucl. Phys. A99: 652. 1967.

73. Alexander, P. and F. Boehm. Nucl. Phys. 46: 108. 1963.

74. Brown, J. E. and E. N. Hatch. A computer method for determining by least squares gamma ray relative intensities using a bent-crystal monochromator. U.S. Atomic Energy Commission Report IS-993 (Iowa State Univ., Ames). 1964.

75. Leutz, H., K. Schneckenberger and H. Wenninger. Nucl. Phys. 63: 263. 1965.

76. Donnelly, D. P. and M. L. Wiedenbeck. Nuclear Instr. and Methods 64: 26. 1968.

77. Shliagan, K. N. and P. S. Samoilov. Soviet Physics JETP (U.S.S.R.) 34: 20. 1958.

78. Taff, L. M. and P. M. Champion. A computer program for automatic analysis of semi-conductor detector spectra. U.S. Atomic Energy Commission Report IS-1986 (Iowa State Univ., Ames). 1968.

79. Davisson, C. M. Gamma-ray attenuation coefficients. In Siegbahn, K., ed. Alpha-, Beta- and Gamma-Ray Spectroscopy. P. 827. Amsterdam, Netherlands, North-Holland Publishing Co. 1965.

80. Lazar, N. H., R. C. Davis and P. R. Bell. Nucleonics 14, No. 4: 52. 1956.

81. Vegors, S. H., Jr., L. L. Marsden and R. L. Heath. Calculated efficiencies of cylindrical radiation detectors. U.S. Atomic Energy Commission Report IDO-16370 (Idaho Nuclear, Idaho Falls). 1958.

82. Axel, P. Rev. Sci. Instr. 25: 391. 1954.

83. Merritt, J. S. and J. G. V. Taylor. Anal. Chem. 37: 351. 1965.

84. Taff, L. M. The nuclear decays of Zr^{97} and Nb^{97}. Unpublished Ph.D. thesis. Ames, Iowa, Library, Iowa State University of Science and Technology. 1969.

85. Schmid, L. C. and S. B. Burson. Phys. Rev. 115: 447. 1959.

86. Agin, G. P., C. E. Mandeville and V. R. Potnis. Nucl. Phys. A105: 698. 1967.

87. Boneau, D. and E. N. Hatch. Am. Phys. Soc. Bull. Series II, 13: 670. 1968.

88. Widemann, F. and C. Sebille. Nucl. Phys. A117: 129. 1968.

89. Sund, R. E. and M. L. Wiedenbeck. Phys. Rev: 120, 1792. 1960.

90. Kracik, B., Z. Miligui, V. Brabec, M. Vejs, A. Mastalka and T. Kucarova. Czech. J. Phys. 13: 79. 1963.

91. Baker, J. M. and F. I. B. Williams. Proc. Roy. Soc. 267A: 283. 1962.

92. Sund, R. E., R. G. Arns and M. L. Wiedenbeck. Phys. Rev. 118: 776. 1960.

93. Nilsson, S. G. Kgl. Danske Videnskab. Selskab, Mat.-Fys. Medd. 29, No. 16: 1. 1955.

94. Bohr, A. and B. R. Mottelson. Kgl. Danske Videnskab. Selskab, Mat.-Fys. Medd. 27, No. 16: 1. 1953.

95. Alaga, G., K. Alder, A. Bohr and B. R. Mottelson. Kgl. Danske Videnskab. Selskab, Mat.-Fys. Medd. 29, No. 9: 1. 1955.

96. Schmid, L. C. and S. B. Burson. Phys. Rev. 115: 178. 1959.

97. Fossan, D. B., L. F. Chase, Jr., and K. L. Coop. Phys. Rev. 140: B1. 1965.

98. Dzhelepov, B. S., Yu. V. Kalinchev and A. G. Sergeev. Acad. Sci. Bull., Physical Series (U.S.S.R.) 31: 666. 1967.

99. Cabezas, A. Y., I. Lindgren and R. Marrus. Phys. Rev. 122: 1796. 1961.

100. Burdick, B. and R. Marrus. Phys. Rev. 132: 723. 1963.

101. Chery, R. J. Phys. Radium 22: 665. 1961.

102. Suter, T., P. Reyes-Suter, S. Gustafson and I. Marklund. Nucl. Phys. 29: 33. 1962.

103. Eastwood, H. K. and R. G. Summers-Gill. Can. J. Phys. 46: 230. 1968.

104. Nealy, C. L. and R. K. Sheline. Phys. Rev. 164: 1503. 1967.

105. Mattauch, J. H. E., W. Thiele and A. H. Wapstra. Nucl. Phys. 67: 32. 1965.

106. Planskoy, B. Nucl. Instr. and Methods 61: 285. 1968.

107. Andersen, V. and C. J. Christensen. Nucl. Instr. and Methods 61: 77. 1968.

108. Frauenfelder, H. and R. M. Steffen. Angular Correlations. In Siegbahn, K., ed. Alpha-, Beta- and Gamma-Ray Spectroscopy. Pp. 99701197. Amsterdam, Holland, North-Holland Publishing Co. 1965.

109. Jackson, J. D. Classical Electrodynamics. New York, N.Y., John Wiley and Sons. 1962.

110. Verheul, H., J. Blok, H. G. Boddendijk and B. G. Vonck. Physica 31: 565. 1965.

111. Vos, J. W. E., C. W. E. Van Eijk, W. H. G. Lewin and F. Schutte. Nucl. Instr. and Methods 60: 285. 1968.

112. Vergnes, M. and J. Jastrzebski. J. Phys. Radium 22: 669. 1961.

113. Malmskog, S. G. Nucl. Phys. 68: 517. 1965.

114. Begzhanov, R. B., D. N. Gladyshev, K. M. Sadykov and K. Teshabaev. JETP Lett. 4: 48. 1966.

115. Burde, J., M. Rakavy and G. Rakavy. Phys. Rev. 129: 2147. 1963.

116. Fossan, D. B. and B. Herskind. Nucl. Phys. 40: 24. 1963 1963.

117. Debrunner, P. and W. Kundig. Helv. Phys. Acta 33: 397. 1960.

118. Sunier, J. W. Helv. Phys. Acta 36: 429. 1963.

119. Zganjar, E. F. The E2 internal-conversion process in ^{152}Gd and ^{154}Gd and the beta-gamma directional correlation in the decay of ^{154}Eu. U.S. Atomic Energy Commission Report TID-22393 (Vanderbilt Univ., Nashville). 1966.

120. Hager, R. S. and E. C. Seltzer. Nuclear Data A4: 397. 1968.

121. Kotani, T. Phys. Rev. 114: 795. 1959.

122. Kotani, T. and M. Ross. Phys. Rev. Letters 1: 140. 1958.

123. Kotani, T. and M. Ross. Prog. Theo. Phys. 20: 643. 1958.

124. Kotani, T. and M. Ross. Phys. Rev. 113: 622. 1959.

125. Biedenharn, L. C. and M. E. Rose. Rev. Mod. Phys. 25: 729. 1953.

V. ACKNOWLEDGEMENTS

I thank Dr. E. N. Hatch for his continual guidance and counsel over the past seven years. I thank K. Malaby and the staff of the Ames Laboratory Research Reactor for their assistance with the irradiation and preparation of the many radioactive sources required. I thank Michael Yester for his help in modifying and executing the computer routines. And finally I thank Charles Turner, George Eakins and the other members of Nuclear Physics Group IV for many discussions on all phases of my work.

VI. APPENDICES

A. Appendix I. Electron Scattering Effects in Silicon Detectors

Planskoy (106) has recently published a fairly detailed study of electron scattering from semiconductor detectors. He divided those electrons that lose less than their original full-energy in the silicon detector into three groups: 1) those backscattered from the silicon itself; 2) those which have lost some energy in scattering off parts of the apparatus into the detector; and 3) those which scatter out the sides of the sensitive area of the detector (edge effect). This division assumes that the thickness of the semiconductor does not allow any incident electrons to escape out the back side of the detector. Figure 28 provides an enlarged view of the source-detector arrangement used in the conversion electron work reported here. The purpose of the aperture was to shield the outer perimeter of the detector in order to reduce any edge effect. It was hoped that the collimator would cut down somewhat on the electrons scattered into the detector from neighboring material. The collimator could not be completely effective because nothing blocks the path of radiation scattered 180^{o} from the region immediately behind the source. The aperture and collimator were designed with the chamfer angles shown in order to minimize any scattering

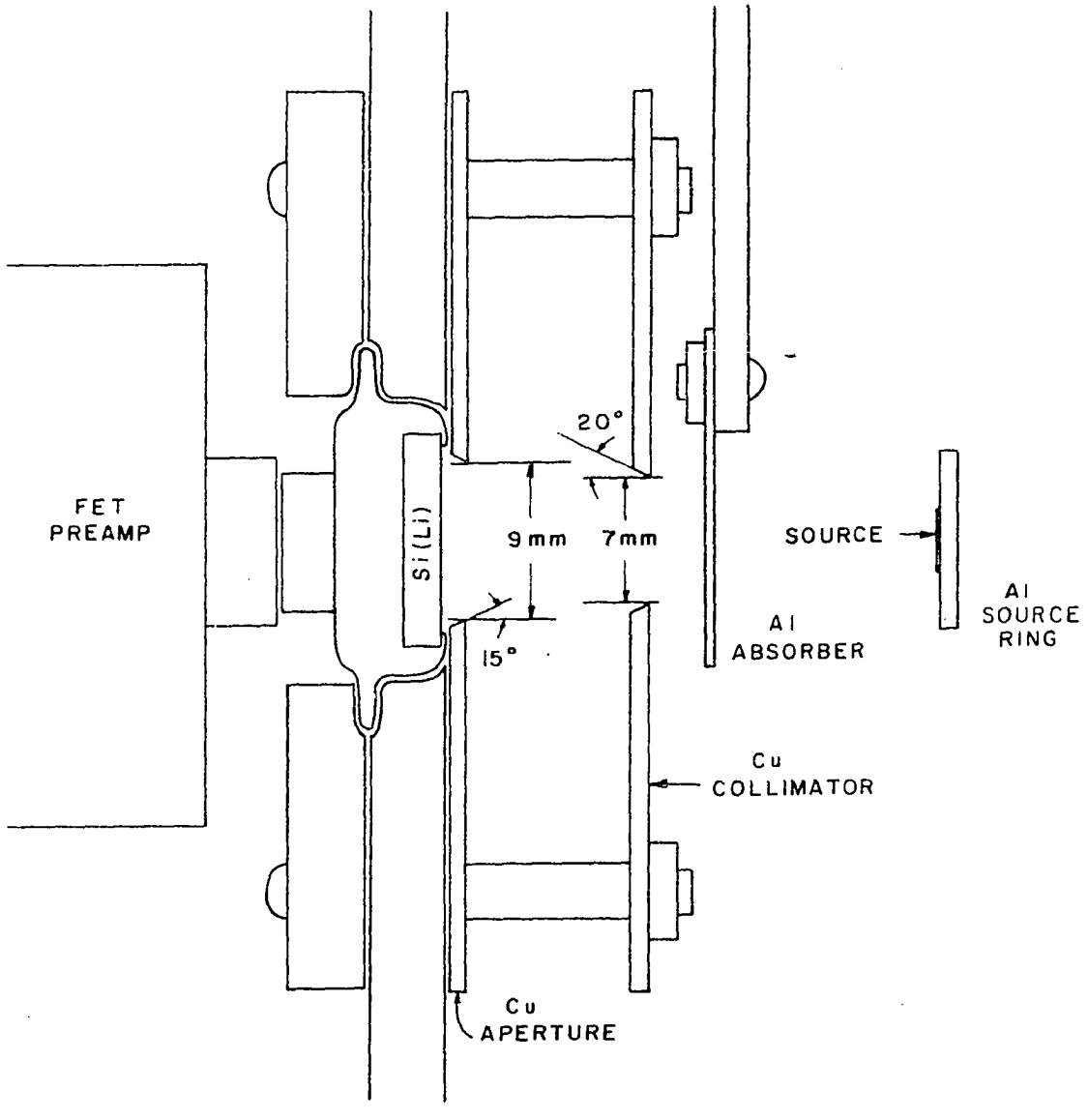

Fig. 28. Cross-sectional view of the source-detector geometry in the silicon spectrometer

from the edges of these pieces.

The worth of the aperture and collimator was tested by observing the shapes of monoenergetic conversion lines from Cd^{109} and Cs^{137} sources with and without these elements in place. Monoenergetic response functions for 62 keV (Cd^{109}) and 625 keV (Cs^{137}) were obtained by retaining only the events in time coincidence with the respective K x-rays. By the nature of the Cd^{109} and Cs^{137} decays, the only radiation (above 10 keV) in coincidence with the K x-rays are the K-shell conversion electrons from the 88- and 662-keV transitions. The K x-rays were detected in the NaI crystal so that the experimental arrangement was similar to that used in determining the intensity of the 62 L line in the Sm^{155} decay. Table 18 lists the total backscatter coefficients found with both aperture and collimator in place, with the collimator removed and with aperture and collimator removed. The total backscatter coefficient is defined as the fraction of the incident electrons that lose less than their full energy in the detector.

The aperture and collimator each help to reduce the backscatter coefficient to an extent. Thus, all the Sm^{155} and Nd^{151} electron data were accumulated with the detector

Table 18. Backscatter coefficient for different experimental arrangements at 200 Volts bias

Experimental arrangement	Backscatter coefficient	
	Cd^{109}	Cs^{137}
Aperture and collimator in place	0.31	0.33
Only aperture in place	0.36	0.36
Neither in place	0.38	0.40

shielded by both aperture and collimator. However, the backscatter coefficients found here are far above the values of 0.15-0.20 reported by Planskoy for similar geometry. Perhaps the mass of material situated directly behind the source holder in the present experiment caused enough scattering to inflate the values in Table 18. A further difficulty in comparing the present work with that of Planskoy is that he does not clearly define where the tail ends and the peak begins. In the work reported here, the peak area includes the Gaussian plus its low-energy hump as discussed in Chapter II while the rest of the response function is allotted to the tail. It is encouraging to note that the results in the first row of Table 18 agree very closely with the peak efficiency data obtained from Hf^{180m} and Ag^{110m} spectra and discussed in Chapter II.

In another recent approach to the study of electron

scattering from silicon detectors, Anderson and Christensen (107) eliminated the effects of backscattering by summing the pulses from two detectors situated at either end of a superconducting solenoid. The response function for 1 MeV electrons still had a tail containing about ten percent of the total counts under conditions similar to ours. Anderson and Christensen attributed this tail to some effect inherent in the detectors. They found that the size of the tail decreases sharply as the applied detector voltage is increased. Table 19 shows the effects of varying detector bias on the backscatter coefficient for the present experimental arrangement.

Table 19. Variation of backscatter coefficient with applied detector voltage

Bias voltage	Backscatter coefficient Cd^{109}	Cs^{137}
150	0.32	0.33
200	0.31	0.33
250	0.30	0.33
265	0.30	0.33

We found very little change with increasing voltage - nothing like the factor of two reduction seen by Anderson and Christensen. While the relative areas of the peak and tail remained about constant, the peak width did decrease markedly

with increasing bias. It is possible that the effects of raising the detector voltage were obscured somewhat by the predominant backscattering in the experiment reported here.

B. Appendix II. Beta-ray Branching Effects

In the coincidence method for suppressing the continuous beta-ray distribution, the only electrons seen by the silicon detector that are recorded are those that occur in coincidence with a beta ray which loses more than some cutoff energy E_c in the plastic scintillator. For a beta-ray branch with endpoint E_o, the fraction of the beta rays with energies greater than E_c is an increasing function of E_o. Thus, conversion electrons in coincidence with high-energy beta-ray branches are enhanced over those in coincidence with low-energy branches. In order to formulate the problem, consider the general decay scheme in Figure 29. Here I_{jk} represents the fraction of the decays of the parent that proceeds from level k to level j via either gamma-ray emission or internal conversion, and B_ℓ is the fraction of the decays of the parent that proceeds directly to level ℓ by beta decay. The intensity of electrons converted in the i th shell by transition jk which is seen by the silicon detector operating in the coincidence mode is

$$M^i_{jk} = \frac{\alpha_i}{1+\alpha_{total}} N_o \epsilon \sum_{\ell=k}^{n} f_\ell < jk,\ell > C_i(jk,\ell) \qquad (1)$$

where n is the total number of energy levels (here n = 5), N_o is the total number of decays, $\epsilon = \epsilon_s \epsilon_p \epsilon_c$ includes the abso-

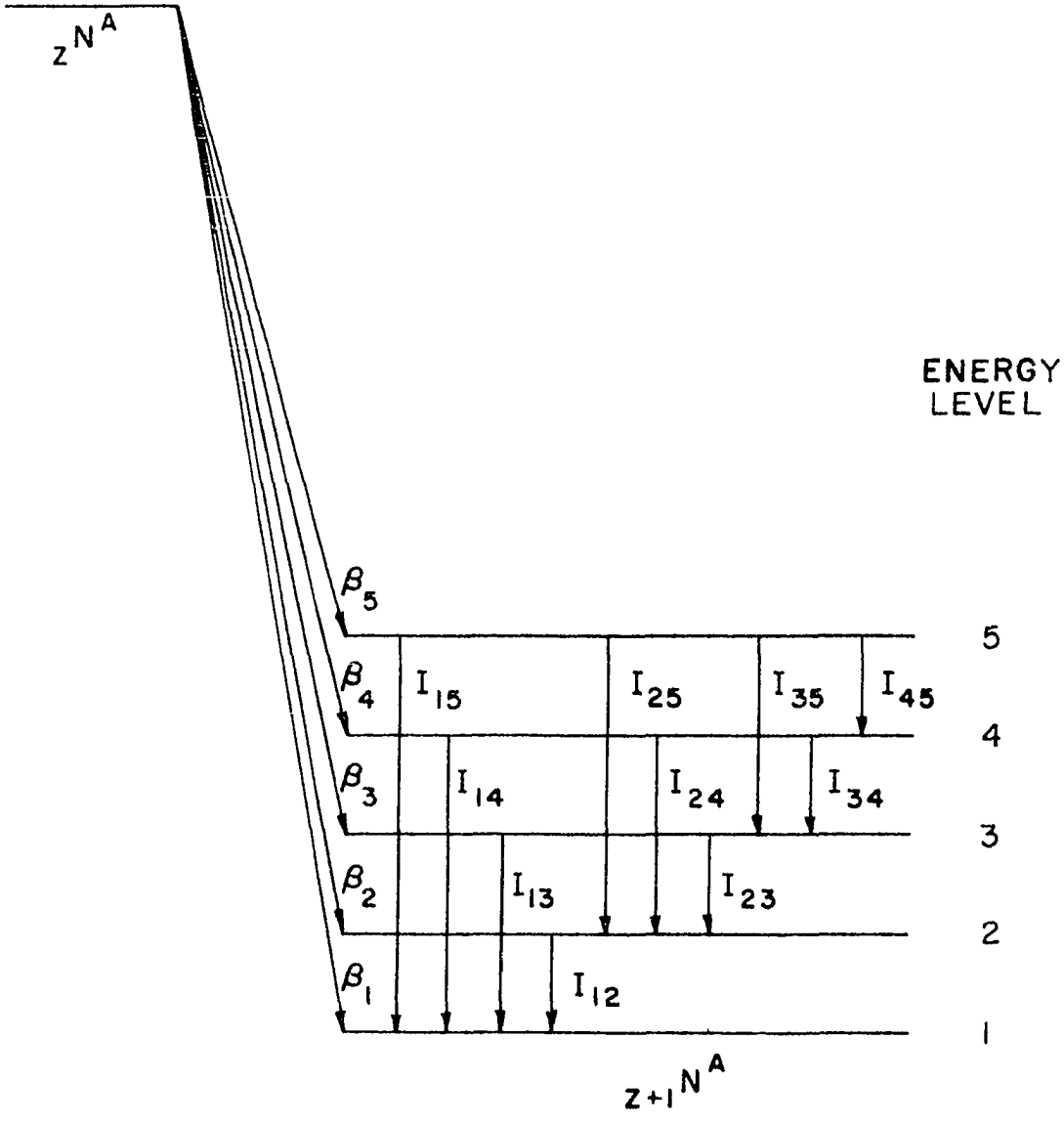

Fig. 29. An idealized level scheme for a daughter nucleus fed by beta decay

lute efficiences of both the silicon and plastic detectors plus the coincidence circuit, f_ℓ is the fraction of beta rays feeding level ℓ that loses energy greater than E_c in the plastic scintillator, $< jk,\ell >$ is the coincidence intensity between the beta-ray branch to level ℓ and the transition jk and $C_i(jk,\ell)$ is the angular correlation factor discussed in Appendix III. The timing of the coincidence circuit was adjusted so that $\epsilon_C = 1.0$. The coincidence intensity can be written as

$$<jk,\ell> = R_{jk} \left\{ \sum_{m=1}^{N} \prod_{k \leq p < r \leq \ell} R_{pr} \right\} \beta_\ell$$

where $R_{pr} = \dfrac{I_{pr}}{\sum_{s=1}^{r-1} I_{sr}}$ is a branching ratio and the summation extends over the $N = 2^{\ell-k-1}$ possible products of R_{pr} such that $k \leq p < r \leq \ell$. If $k = \ell$, the expression enclosed in brackets is unity. As an example, $<13,5> = R_{13}[R_{34}R_{45} + R_{35}]\beta_5$ where $R_{13} = I_{13}/I_{13}+I_{23}$ and so forth. Notice that the decay scheme must be known in detail in order to compute exact values for the coincidence intensities.

The fraction f_ℓ depends on both the nature of the beta-ray branch to level ℓ and the resolution properties of the

scintillation detector. For a simple beta transition the electrons emitted per second with energy in an interval dW is

$$N(W)dW = KS_nF_o(Z,A,W)W\sqrt{W^2-1}\ (W_o-W)^2dW.$$

Here W is the total electron energy (including rest mass) in units of m_ec^2, $W_o = 1+E_o$ is the maximum value of W, F_o is the Fermi function which depends on the charge (Z) and the mass (A) of the daughter nucleus in addition to the electron energy, S_n is the shape factor for n th forbidden beta-ray transitions and K is a numerical constant. The probability P(W,W') that an electron emitted with energy W is detected in the plastic scintillator with energy W' was found to approximate a Gaussian with width $\sigma \propto \sqrt{W-1}$ and FWHM of 18% at one MeV. Thus

$$P(W,W') = \frac{1}{\sigma\sqrt{2\pi}}\ e^{-\frac{1}{2}\left(\frac{W-W'}{\sigma}\right)^2}$$

and the rate of electrons detected with energy W' is

$$D(W')dW' = \Omega\, dW' \int_1^{W_o} P(W,W')N(W)dW$$

where Ω is the solid angle subtended by the plastic crystal. Scattering from the crystal is ignored. In the coincidence method, only beta rays detected with total energy greater than $1+E_c$ gate the coincidence circuit. The fraction of all beta rays with this property is

$$f = \int_{1+E_c}^{\infty} D(W')dW' \Big/ \int_{1}^{\infty} D(W')dW'.$$

A computer routine was written to calculate f for any values of E_o and E_c. The calculation assumes the beta-ray transition is allowed; then, n = 0 and $S_o = 1$. Figure 30 illustrates beta-ray spectra with endpoints $E_o = 1000^o$ and $E_o = 1500$ keV. The total areas of the two spectra are equal, but the fractional areas above $E_c = 500$ keV are quite different.

If angular correlations are unimportant, all the corrections for the effects of beta branching are now understood. The ratio of i th shell conversion electrons from transition jk in a coincidence spectrum to those in a singles spectrum is just

$$\frac{M^{i}_{jk}}{I^{e_i}_{jk}} = \frac{[\epsilon_p \sum_{\ell=k}^{n} f_\ell \langle jk, \ell \rangle]}{I_{jk}} \qquad (1)$$

and

$$\frac{I^{e_i}_{jk}}{I^{e_\lambda}_{\rho\nu}} = \frac{M^{i}_{jk}\, I_{jk} \sum_{\pi=\nu}^{n} f_\pi \langle \rho\nu, \pi \rangle}{M^{\lambda}_{\rho\nu}\, I_{\rho\nu} \sum_{\ell=k}^{n} f_\ell \langle jk, \ell \rangle}. \qquad (2)$$

Actually, however, the singles plus coincidence intensities depend upon the electron intensities to be found. Normally gamma-ray intensities coupled with theoretical internal

conversion coefficients provide a reasonable approximation of the total transition intensities. In addition, the electron relative intensities of the stronger lines were obtained from singles spectra. A self-consistent approach was then used to correct the intensities of weak conversion electron lines for the effects of beta branching in the coincidence method.

In detail, then, the correction procedure assumes the gamma-ray relative intensities and the placement of the nuclear levels and transitions within the decay scheme to be known. The normalizing internal conversion coefficient is measured and the relative intensities of the stronger conversion electron lines are determined from the singles spectra. This data is sufficient to fix coefficients and multipolarities for some of the more important transitions and hence to establish the spins and parities of some nuclear levels. The known properties of the decay scheme are then combined with intuition to assign tentative but reasonable multipolarities and total intensities to the transitions whose conversion electron lines show up only in the coincidence electron spectra. Equations 1 and 2 then provide an initial correction to the coincidence electron intensities and the corrected electron intensities lead to a second estimate of the total

Fig. 30. Computer reproductions of continuous beta-ray distributions seen by the plastic scintillator. The fraction (f) of an individual distribution that loses more than the cutoff energy in the detector depends on the endpoint energy of the distribution

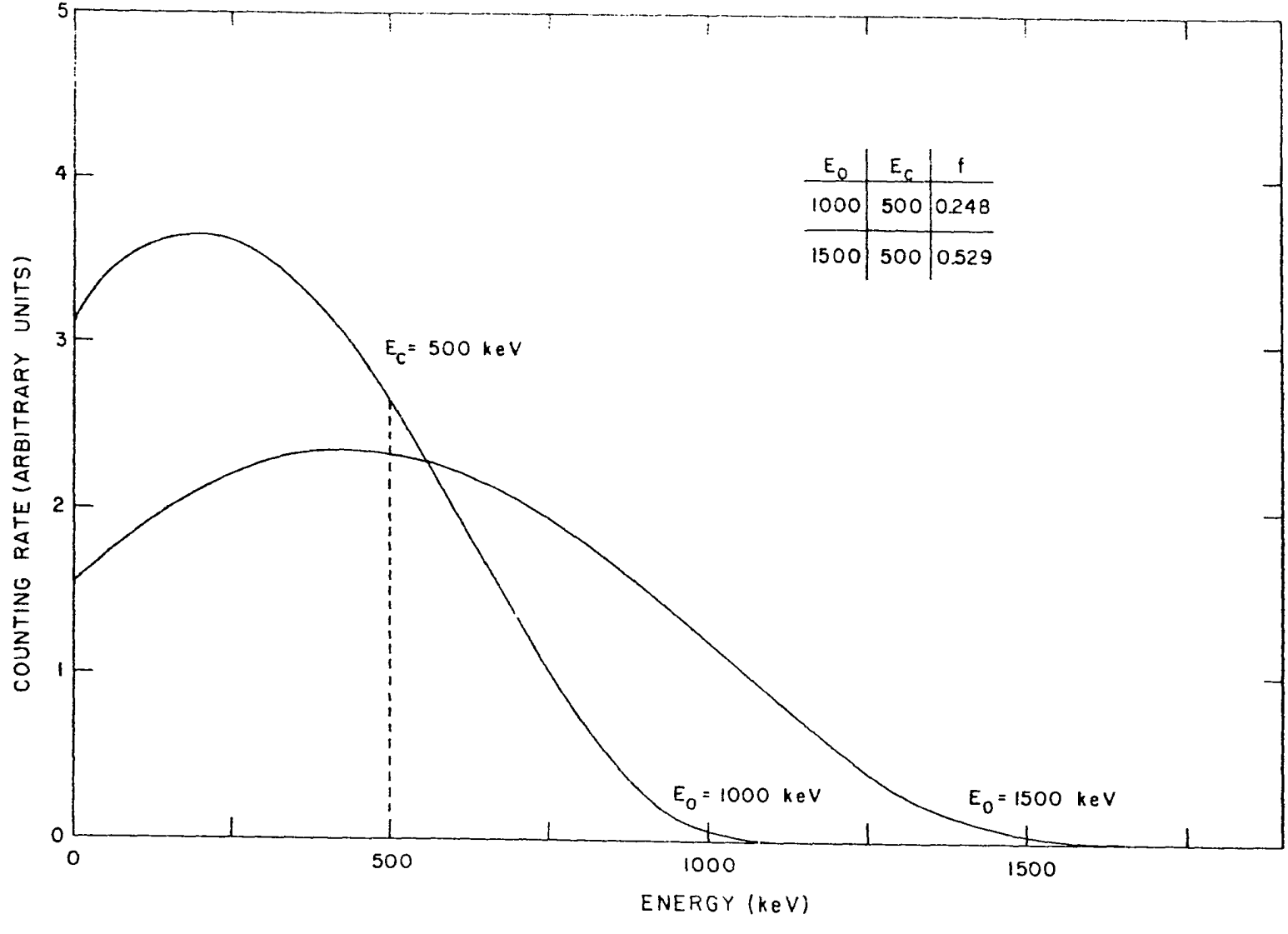
5
4
3
2
1
0
0
500
1000
1500
COUNTING RATE (ARBITRARY UNITS)
ENERGY (keV)
E_c = 500 keV
E_0 = 1000 keV
E_0 = 1500 keV
E_0 | E_c | f
1000 | 500 | 0.248
1500 | 500 | 0.529

reasonable approximation to the total transition intensities. In addition, the electron relative intensities of the stronger lines were obtained from singles spectra. A self-consistent approach was then used to correct the intensities of weak conversion electron lines for the effects of beta branching in the coincidence method.

In detail, then, the correction procedure assumes the gamma-ray relative intensities and the placement of the nuclear levels and transitions within the decay scheme to be known. The normalizing internal conversion coefficient is measured and the relative intensities of the stronger conversion electron lines are determined from the singles spectra. This data is sufficient to fix coefficients and multipolarities for some of the more important transitions and hence to establish the spins and parities of some nuclear levels. The known properties of the decay scheme are then combined with intuition to assign tentative but reasonable multipolarities and total intensities to the transitions whose conversion electron lines show up only in the coincidence electron spectra. Equations 1 and 2 then provide an initial correction to the coincidence electron intensities and the corrected electron intensities lead to a second estimate of the total

intensities for those transitions whose conversion lines appear only in the coincidence spectra. Then a second estimate of the beta-ray branching correction is calculated, and so forth, until a consistent decay scheme is obtained. In practice, two iterations were always sufficient although no proof exists (to my knowledge) that the procedure even converges. The believability of the scheme can be checked to an extent by comparing corrected coincidence intensities for those conversion electron lines which show up in both the singles and the coincidence spectra.

C. Appendix III. Angular Correlation Factors

Whenever coincidence measurements are made between nuclear radiations, angular correlation effects may be present and must be assessed for the individual experiment. This appendix discusses the possibility of correlation effects arising from coincidences between conversion electrons detected in the silicon semiconductor and continuous beta rays seen by the plastic scintillator. The treatment is similar to that of Schupp and Hatch (28).

Figure 31 shows a schematic picture of the geometrical orientation of the source and the two detectors. In order to simplify the calculations and clarify the principles, it is assumed that the only electrons detected are those which leave a point source S within the cones of halfangle θ_2 or $\pi-\theta_1$. We further assume that the detection probability is unity for electrons leaving the source in these angular regions and is zero otherwise. The efficiency of the coincidence circuit is taken to be one.

Consider again the decay scheme in Figure 29. The number of electrons in coincidence with beta-ray branch β_k that are converted in the i th shell by transition jk as seen by the silicon detector is

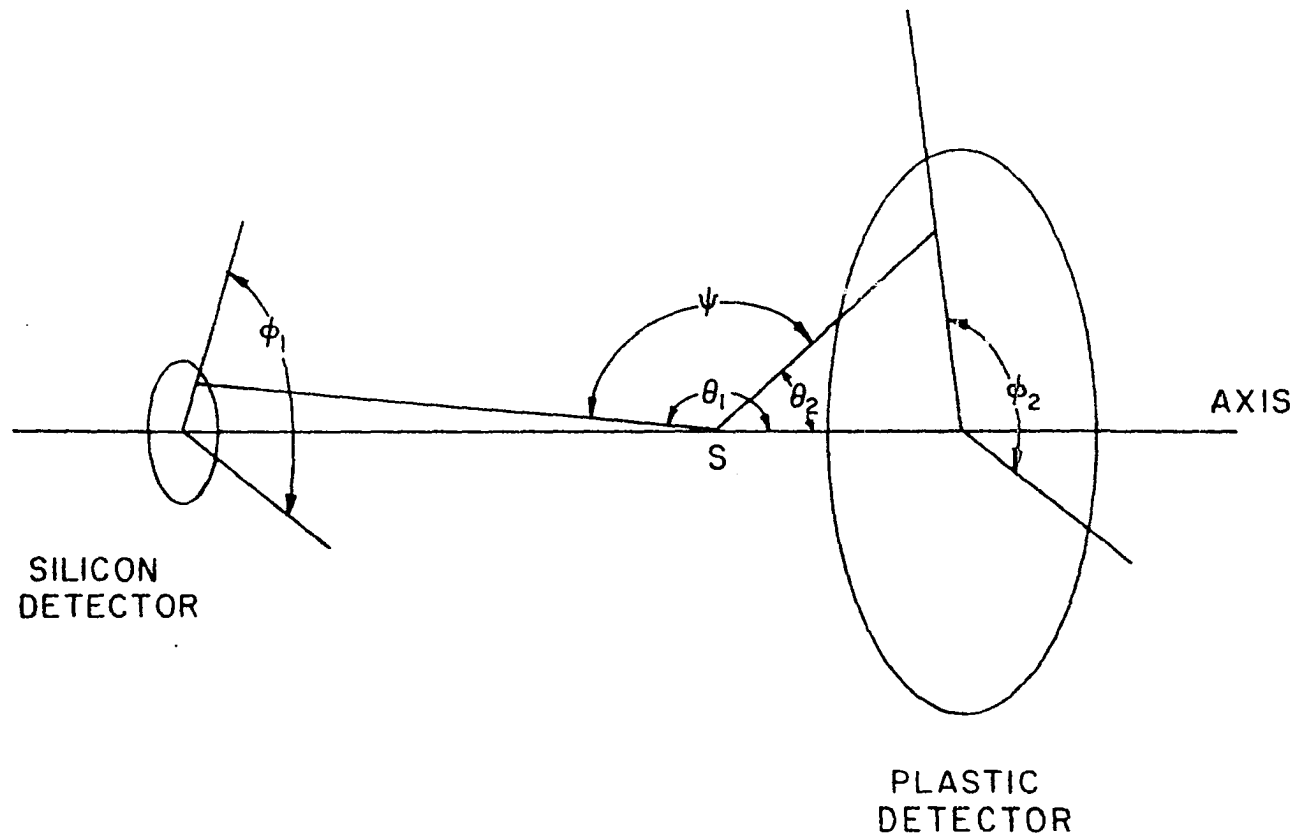

Fig. 31. Schematic drawing of the angles used to describe the coincident radiations detected by the silicon and plastic crystals

$$N^{i}_{jk} = \frac{\alpha_i}{1+\alpha_{total}} N_o f_k R_{jk} \int_1 \int_2 [d\Omega_1/4\pi][d\Omega_2/4\pi] W(\psi)$$

where N_o is the total number of decays, f_k is the fraction of beta rays feeding level k that loses energy greater than E_c in the plastic scintillator and R_{jk} is the branching ratio for de-excitation of level k. The solid angles $[d\Omega_1/4\pi]$ and $[d\Omega_2/4\pi]$ integrated over the angular regions $\pi-\theta_1$ and θ_2 give the silicon and plastic scintillator detection efficiencies ϵ_s and ϵ_p, respectively. $W(\psi)$ is the angular correlation function which expresses the relative probabilities for coincidences between electrons that leave the source at an angle ψ with respect to each other. It has the form (108)

$$W(\psi) = \sum_{\lambda even} b_\lambda(k) b^i_\lambda(j1) A_\lambda(jk,k) P_\lambda(\cos\psi)$$

where $b_\lambda(k)$ and $b^i_\lambda(jk)$ are particle parameters for the electrons detected in the plastic crystal and the silicon semiconductor, respectively; the A_λ are the usual expansion coefficients for gamma-gamma directional correlations; and P_λ are Legendre polynomials. In practice λ_{max} is often restricted to the value two and is never larger than four.

It is convenient to expand $P_\lambda(\cos\psi)$ in terms of the angles θ_1, ϕ_1, and θ_2, ϕ_2 (109). The terms with ϕ_1 and ϕ_2

vanish in doing the azimuthal integration. The final result is then

$$N^{i}_{jk} = \frac{\alpha_i}{1+\alpha_{total}} N_o f_k R_{jk} [\Omega_1/4\pi][\Omega_2/4\pi]$$

$$\cdot \sum_{\lambda_{even}} b_\lambda(k) b^{i}_\lambda(jk) A(jk,k) \overline{P_\lambda(\cos\theta_1)}\ \overline{P_\lambda(\cos\theta_2)}$$

where $\overline{P_\lambda(\cos\theta_1)}$ is the average of $P_\lambda(\cos\theta_1)$ over the angular region $\pi-\theta_1$ and $\overline{P_\lambda(\cos\theta_2)}$ is the similar average over θ_2. A comparison with Equation 1 of Appendix II shows that the angular correlation factor is given by

$$C_i(jk,k) = \sum_{\lambda_{even}} b_\lambda(k) b^{i}_\lambda(jk) A_\lambda(jk,k) \overline{P_\lambda(\cos\theta_1)}\ \overline{P_\lambda(\cos\theta_2)}$$

if we recall that $\epsilon_s = \Omega_1/4\pi$, $\epsilon_p = \Omega_2/4\pi$, $\epsilon_c = 1$, and $R_{jk} = \langle jk,k \rangle$.

The integration described above served to include the effects of the finite size of the two detectors in the directional correlation function. Some authors (110,111) define a correction factor q_λ for the finite size of detector μ by $q_\lambda(\mu)\ P_\lambda(\cos\bar{\theta}_\mu) = \overline{P_\lambda(\cos\theta_\mu)}$. In addition the directional correlation function can be modified by the finite size of the experimental source, by scattering of the emitted electrons in the source and by interactions of the decaying

nucleus with extranuclear fields. Each of the four effects attenuates the experimentally observed correlation below the amount predicted by the characteristics of the transitions and energy levels involves. Each effect tends to smear out any correlation. The corrections are included by writing the present angular correlation function as

$$C_i(jk,k) = \sum_{\lambda\text{even}} q_\lambda(k)q_\lambda(jk)p_\lambda c_\lambda G_\lambda b_\lambda(k)b_\lambda^i(jk)$$

$$\cdot A_\lambda(jk,k)P_\lambda(\cos\bar{\theta}_1)P_\lambda(\cos\bar{\theta}_2).$$

Here q_λ and p_λ correct for the finite size of the detectors and source, c_λ for scattering in the source and G_λ for perturbations due to external fields. The angles $\bar{\theta}_1$ and $\bar{\theta}_2$ are measured to the midpoints of the detector surfaces. Note that all the factors in the expression are defined to be unity for $\lambda = 0$ so the leading term in the expansion is just one.

Explicit expressions to correct for the finite size of cylindrical detectors are easily found (111) to be

$$q_2 = \tfrac{1}{2}\cos\rho(1+\cos\rho)$$

$$q_4 = \tfrac{1}{2}q_2(7\cos^2\rho-3)$$

where $\rho \equiv \theta_{max}$ is the halfangle of the cone subtended by the detector at the source. These angles were measured to be

$\rho_1 = (62 \pm 2)^\circ$ and $\rho_2 = (12 \pm 1)^\circ$ for the coincidence spectrometer. The effect of the finite size of a circular source is treated by Verheul et al. (110). The sources used in the work reported here cause an attenuation of only about 2% for both $\lambda = 2$ and $\lambda = 4$. A nomogram for computation of the scattering correction factor is included in the extensive review article by Frauenfelder and Steffen (108). In the present experiment, the typical value of C_2 is 0.85-0.90 with $C_4 \simeq 2C_{2-1}$. The interactions with extranuclear fields are quite complex and no attempt has been made to include all possible variables in an explicit calculation. Frauenfelder and Steffen do devote a large section to a discussion of specific approaches to the problem. As a rule of thumb, attenuations due to external fields are possible if the lifetime of the intermediate state is longer than 10^{-10} - 10^{-11} seconds. Several transitions in the Sm^{155} and Nd^{151} decays have measured lifetimes of about 10^{-9} seconds (112,113,114). The 123-keV level in Gd^{154} has a lifetime of 1.17 nsec (115,116) and measured G_2 values of 0.56 (117,118,119). Thus, it is possible that some directional correlations in the present work were greatly attenuated due to extranuclear fields. However, no general estimate of the magnitude of the effect can be made.

If the effects of external fields are neglected, the angular correlation function has the form

$$C_i(jk,k) = 1 + (0.29\pm0.03)b_2(k)b_2^i(jk)A_2$$

$$-(0.08\pm0.01)b_4(k)b_4^i(jk)A_4$$

since $P_\lambda(\cos\bar{\theta}_1) = P_\lambda(\cos\bar{\theta}_2) = 1$ for $\bar{\theta}_1 = 180^o$ and $\bar{\theta}_2 = 0^o$.

Tables of the gamma-gamma expansion coefficients A_λ are included in Part II of Hager and Seltzer's work (120) on internal conversion. They have values of the order of unity. Extensive listings of the conversion electron particle parameters have recently been published in the same report by Hager and Seltzer. The particle parameters for beta decay are discussed by Frauenfelder and Steffen (108), Kotani (121), and Kotani and Ross (122,123,124). The parameters $b_2(k)$ and $b_4(k)$ are identically zero for an allowed beta-ray transition and the coincident transition is emitted isotropically. Since allowed transitions tend to dominate in beta decay, this fact greatly reduces the chance of observing any directional correlations in the work reported here. The other likely form of beta decay occurs via non-unique first forbidden transitions where $b_4(k)$ is again zero. The particle parameter $b_2(k)$ is in general non-zero; but its specific form depends on

unknown nuclear matrix elements. If the non-unique first forbidden beta-ray transition can be described by the ξ-approximation (122,124), the maximum possible directional anisotropy is about 10%. The adequacy of the ξ-approximation is normally characterized by small log ft values of 6-7, as are the beta-ray branches observed in the Sm^{155} and Nd^{151} decays. Experimental measurements in the Ce^{144} and Nd^{149} decays (108), where the endpoint energies and log ft values are similar to those seen in the present work, found anisotropies of only 1-3%.

The discussion in this appendix has considered only the case where the internally converted transition is fed directly by beta decay. It is possible for the beta decay to feed an intermediate transition which is in coincidence with the internally converted transition. Again, the beta ray and the conversion electron are detected in coincidence but the intermediate transition escaped unnoticed. Biedenharn and Rose (125) calculate some directional correlation functions for just this case. The unseen intermediate transition generally is more strongly correlated with the beta ray than is the subsequent transition that gives rise to the observed conversion electron. The effect again diminishes the possibility of seeing directional correlations in the experiments reported

here.

We have seen that any complexity due to angular correlation effects was reduced by a host of factors which shrink the correlation function. The $\lambda = 4$ term is zero for all situations of interest here. Geometrical factors attenuate the $\lambda = 2$ term by at least 70% while $b_2(k)b_2^i(jk)A_2$ is very probably less than 0.1. Further attenuations arose because of extranuclear fields and unseen intermediate transitions. Thus, no angular correlation corrections were made to the internal conversion electron relative intensities found from coincidence experiments. However, a three percent uncertainty was included in the coincidence electron intensities to allow for such correlation effects as seem possible.